Modeling of Deep-Convective Transport of Forest Fire Smoke into the Upper Troposphere and Lower Stratosphere

Dissertation
zur Erlangung des Grades
"Doktor der Naturwissenschaften"
am Fachbereich Physik
der Johannes Gutenberg-Universität Mainz

vorgelegt von

Gunnar G. Luderer
geboren in Rottenburg-Wendelsheim

Mainz

Juli 2007

Tag der mündlichen Prüfung: 19. September 2007

Abstract

Deep convection by pyro-cumulonimbus clouds (pyroCb) can transport large amounts of forest fire smoke into the upper troposphere and lower stratosphere. Here, results from numerical simulations of such deep convective smoke transport are presented. The structure, shape and injection height of the pyroCb simulated for a specific case study are in good agreement with observations. The model results confirm that substantial amounts of smoke are injected into the lower stratosphere. Small-scale mixing processes at the cloud top result in a significant enhancement of smoke injection into the stratosphere.

Sensitivity studies show that the release of sensible heat by the fire plays an important role for the dynamics of the pyroCb. Furthermore, the convection is found to be very sensitive to background meteorological conditions. While the abundance of aerosol particles acting as cloud condensation nuclei (CCN) has a strong influence on the microphysical structure of the pyroCb, the CCN effect on the convective dynamics is rather weak. The release of latent heat dominates the overall energy budget of the pyroCb. Since most of the cloud water originates from moisture entrained from the background atmosphere, the fire-released moisture contributes only minor to convection dynamics.

Sufficient fire heating, favorable meteorological conditions, and small-scale mixing processes at the cloud top are identified as the key ingredients for troposphere-to-stratosphere transport by pyroCb convection.

Zusammenfassung

Pyrocumulonimbus Wolken (PyroCb) können große Mengen Rauch aus Waldbränden in die obere Troposphäre und untere Stratosphäre transportieren. In dieser Arbeit werden Ergebnisse von numerischen Simulationen solcher PyroCb-Konvektion vorgestellt. Die Form, Struktur und Injektionshöhe der für eine Fallstudie simulierten Wolke stimmen gut mit Beobachtungen überein. Die Modellergebnisse bestätigen einen erheblichen Eintrag von Rauch in die Stratosphäre und zeigen, dass kleinskalige Vermischungsprozesse zu einer deutlichen Verstärkung des Raucheintrags in die Stratosphäre führen.

Sensitivitätsstudien zeigen, dass die vom Feuer erzeugte Hitze einen wichtigen Einfluss auf die dynamische Struktur der PyroCb hat. Außerdem wirken sich meteorologische Bedingungen sehr stark auf die Konvektionsdynamik aus. Die hohe Anzahl der durch das Feuer emittierten Aerosolpartikel, die als Kondensationskeime wirken, beeinflusst zwar stark die mikrophysikalischen Eigenschaften der Wolke, hat aber nur schwache Auswirkungen auf die Konvektionsdynamik. Die Freisetzung latenter Wärme dominiert das Energiebudget der Wolke. Das meiste Wolkenwasser stammt aus eingemischter Umgebungsluft, daher liefert die durch das Feuer freigesetzte latente Wärme nur einen untergeordneten Beitrag zur Konvektionsdynamik.

Ausreichend starke Hitzeentwicklung durch das Feuer, begünstigende meteorologische Bedingungen und kleinskalige Transportprozesse an der Wolkenobergrenze werden als Hauptvoraussetzungen für den Eintrag von Rauch in die untere Stratosphäre identifiziert.

Contents

Chapter 1

Introduction

1.1 Biomass burning and its atmospheric relevance

It has been well established that biomass burning is a key element in the global budgets of particulate matter, greenhouse gases (most importantly CO_2, CH_4 and N_2O), and other trace gases [*Crutzen and Andreae*, 1990; *Andreae and Merlet*, 2001]. Biomass burning includes both vegetation fires and the use of biomass as a source of energy, e.g., the utilization of fuelwood for heating and cooking. The total mass of biomass burned, however, is dominated by vegetation fires, which account for roughly two thirds [*Andreae*, 1993]. While fires have existed on Earth for hundreds of millions of years, well before humans learned to use fire as an active tool, many modern vegetation fires are caused by human activity.

Most vegetation fires occur in the tropics. Particularly in the dry tropical zones such as savanna-woodlands, these fires are part of the natural biogeochemical cycles. Humans, however, play a significant role in modifying the natural fire regime by changing the frequency and seasons of burning. Deforestation fires occur each year for conversion of forests to cropland or pastures and are the major destructive force in tropical forests worldwide [*Nepstad et al.*, 1999]. Additionally, forest degradation due to selective logging [*Asner et al.*, 2005] disturbs ecosystems and results in increased vulnerability to fire, thus giving rise to further, indirectly anthropogenic, biomass burning. Major directly or indirectly anthropogenic fires have occurred in the Brazilian Amazon and Indonesia during the 1990s and continue to be a serious threat to native forests [*Antle et al.*, 2001; *Goldammer and Price*, 1998].

In contrast to most other surface emissions (e.g., combustion of fossil fuel, dust), emissions from wildland fires are typically co-located with atmospheric con-

vection: so-called pyro-convection, induced by the emission of sensible heat from the fire. The intensity of pyro-convection and therefore the vertical lifting of the fire emissions depends on the size and type of the wildland fire and the convective potential of the atmosphere. Especially in boreal regions, large, intense crown fires combined with conditionally unstable atmospheric conditions can lead to extreme convection with the potential to transport fire emissions into the upper troposphere (UT) and even into the lower stratosphere (LS).

To understand the processes associated with intense pyro-convection, detailed information on the fire emissions and the atmospheric conditions is required. Some observational studies of pyro-convection events from prescribed fires are available. These studies often focused on processes associated with the fires themselves (e.g., the Bor fire, *FIRESCAN Science Team*, 1996). Other studies provide insights into pyro-convection, but only little information about the fire behavior is available (e.g., the Battersby and the Hardiman fires, *Radke et al.*, 1988, 1991; *Banta et al.*, 1992). More comprehensive datasets are available for the Quinault fire on the U.S. West Coast [*Hobbs et al.*, 1996; *Gassó and Hegg*, 1998], the Timbavati fire in South Africa [*Hobbs et al.*, 2003], and from the International Crown Fire Modeling Experiment (ICFME) in Canada's Northwestern Territories [*Stocks et al.*, 2004]. None of these prescribed fires, however, resulted in cloud formation and deep convection.

1.2 Biomass smoke in the stratosphere

For a long time, it has been generally accepted that stratospheric aerosol originates from mainly two sources, namely direct injection of particulate matter by volcanic eruptions, and transport of COS transported from the troposphere, which is subject to photo-oxidation and subsequent transformation into sulphuric acid droplets [*Brasseur and Solomon*, 1984]. The abundance and composition of aerosol in the stratosphere are of major importance for both atmospheric chemistry and radiative balance. Aerosol particles influence the atmospheric radiation budget by intercepting incoming solar radiation and absorbing it or reflecting it back to space, giving rise to cooling at the earth surface and local heating of the respective atmospheric layer. In the stratosphere, aerosol particles have a particularly long lifetime. While particulate matter in the troposphere is subject to wet removal and dry deposition with lifetimes on the order of several days, particles in the stratosphere are located well above tropospheric scavenging mechanisms such as clouds and precipitation. For small particles, gravitational settling is slow, therefore the exchange of air masses with the troposphere is likely the most relevant

sink mechanism.

Recent research has discovered that very large forest fires also have the potential to inject aerosol and trace gases directly into the lower stratosphere through deep convection [*Fromm et al.*, 2004]. More and more observational studies document biomass burning tracers in the upper troposphere and lower stratosphere (UT/LS) region from both remote sensing (satellite and ground based) and in situ instrumentation. *Waibel et al.* [1999] measured enhanced concentrations of carbon monoxide (CO) from boreal fires in Canada in the UT/LS over Europe in the summer of 1994. In the summer of 2002, *Jost et al.* [2004] found particulate and gaseous emissions from a Canadian fire in the stratosphere close to Florida, USA. Also above Florida, enhanced concentrations of methyl cyanide (CH_3CN) from fires in Idaho were detected by the Microwave Limb Sounder (MLS) in the lower stratosphere in 1992 [*Livesey et al.*, 2004]. *Siebert et al.* [2000] report lidar measurements of a stratospheric aerosol layer over Sweden, likely originating from a Canadian wildfire in 1998. Satellite measurements demonstrated that this smoke layer extended over large areas [*Fromm et al.*, 2000, 2005]. Enhanced CO concentrations in the UT/LS region originating from Siberian fires in 2003 were found over Asia and over Europe [*Nedelec et al.*, 2005; *Immler et al.*, 2005]. Lidar measurements over Wisconsin, USA, in 2004 showed an upper tropospheric smoke layer resulting from fires in Alaska and the Yukon Territory [*Damoah et al.*, 2006].

A small but increasing number of studies document direct injection of smoke into the UT/LS region by so called pyro-cumulonimbus (pyroCb). All these events led to long-lasting and large-scale pollution. Most notably, the pyroCb convection induced by the Chisholm Fire, which burned in Alberta, Canada, in May 2001, lead to the formation of a deep convective cloud that penetrated the tropopause, and deposited smoke into the boreal stratosphere [*Fromm and Servranckx*, 2003; *Fromm et al.*, 2007a,b; *Rosenfeld et al.*, 2007]. The summer of 1998 was characterized by strong forest fire activity and substantial enhancement of stratospheric aerosol [*Fromm et al.*, 2000]. For this year, satellite imagery also shows that direct injection by Canadian forest fires through pyro-convection was responsible for the increase in stratospheric aerosol optical depth [*Fromm et al.*, 2005]. In another well documented case, extensive fires near Canberra, Australia, in 2003 led to a fire-induced pyro-cumulonimbus (pyroCb) that reached up to an altitude of 14 km, i.e., well into the stratosphere [*Mitchell et al.*, 2006; *Fromm et al.*, 2006].

It is well known that stratospheric aerosol has a strong influence on the climate at the Earth surface. Large volcanic eruptions, such as those of El Chichon (1982) and Pinatubo (1991) resulted in significant enhancement of stratospheric aerosol burden over the entire globe on time scales of more than a year [*Robock*, 2000]. This

resulted in a marked perturbation of the radiative balance, with strong warming in the stratosphere and noticeable cooling at the Earth surface. In earlier times, eruptions such as the Grimsvotn eruption in Iceland (1783) or the 1813 Tambora eruption may have even had a strong impact on societies by producing abnormally cold summers resulting in crop failures [*Robock*, 2000].

The strong surface cooling induced by stratospheric aerosol gave rise to the fear of a "nuclear winter", i.e., strong solar dimming and colder climate due to massive stratospheric aerosol loading as a consequence of nuclear warfare [e.g., *Crutzen and Birks*, 1982; *Turco et al.*, 1983; *Robock et al.*, 2007]. Other studies, by contrast, proposed artificial injection of aerosol into the stratosphere as a way of offsetting global warming caused by rising greenhouse gas concentrations. Most recently, *Crutzen* [2006] suggested assessing this option as a possible last resort to avoid the most dramatic consequences of climate change.

In view of the evidence for stratospheric injection by forest fires established by the recent findings, pyro-convection must be added to the list of potential sources of stratospheric aerosol. Moreover, such pyro-convection also transports large amounts of gaseous trace compounds, with potentially important consequences for stratospheric chemistry.

Climate change exerts pressure on forest ecosystems in addition to other forms of human disturbances. In boreal regions, forest wildfires occur mostly naturally and are part of the natural cycle of growth, decay and combustion. In view of the changing climate, however, frequency and severity of boreal forest fires are projected to increase significantly [*Stocks et al.*, 1998]. In several regions, there has been a marked increase in fire activity since the 1970s [*Kurz and Apps*, 1999; *Westerling et al.*, 2006], in parallel with the observed warming trend. Climate change will continue to result in warmer summer climates and more weather extremes such as extended heat waves and droughts. The boreal regions that are most significant for fire activity, continental Canada and Siberia, are also projected to experience a decrease in precipitation due to climate change [*Houghton et al.*, 2001; *Antle et al.*, 2001]. Based on coupled climate-ecosystem modeling, *Kasischke et al.* [1995] projected a significant net carbon loss from boreal forests, mostly due to enhanced fire activity. Net CO_2 release from boreal forest ecosystems constitutes an important component of the climate-biosphere feedback and thus has strong implications for the climate sensitivity of the Earth system [*Andreae et al.*, 2005].

Increased fire activity in boreal forest would also imply increased frequency of explosive, deep-convective smoke transport. It is therefore likely that pyroCb convection as a source of particulate matter and trace gases in the UT/LS will

become increasingly relevant in the future.

1.3 Pyro-convection, pyro-cumulus, and pyro-cumulonimbus clouds

A pyro-cumulus is a cumulus cloud formed by a rising thermal from a fire [*Glickmann*, 2000]. Analogous to the distinction between cumulus and cumulonimbus, the pyro-cumulonimbus (pyroCb) is a fire-aided or -cause convective cloud with sufficient vertical development to reach the upper troposphere or even lower stratosphere [1]. With respect to size, injection height, and atmospheric impact, pyroCbs are the most extreme manifestation of pyro-cumulus.

Cumulus-capped wildfire plumes have been reported in the scientific literature for a long time, with the earliest accounts dating back to the late nineteenth century [*Ward*, 1897, 1898]. A compilation of a number of observations of pyro-cumulus clouds, some of which with substantial vertical development, is provided by *Carpenter* [1919]. Studies on pyro-convection conducted in more recent decades focused on its role for processing and transporting biomass burning emissions of trace gases and particulate matter [*Pickering et al.*, 1996; *Reid and Hobbs*, 1998; *Andreae et al.*, 2004].

The schematically illustrated photograph in Figure 1.1 can be used to visualize the structure of pyro-cumulus clouds. The fire releases large amounts of particulate matter, water vapor and other trace gases. The air parcels above the fire are subject to strong heating, and become positively buoyant, thus giving rise to a column of rapidly ascending smoke-laden air.

If sufficient amounts of moisture are available from the fire and the ambient atmosphere, and if the fire forcing results in sufficient vertical development, the air parcels can rise high enough to become saturated in water vapor and to form a pyro-cloud. Since the effect of the fire heating dominates over the effect of the fire-released moisture, the pyro-cumulus cloud base is usually higher than the lifting condensation level of ambient convection (a detailed discussion of this issue is provided in Chapter 6).

The condensation of water vapor originating from the ambient atmosphere and fire-released moisture results in the release of latent heat, thus further increasing the buoyancy of the smoky air and enhancing the vertical development of the pyro-cumulus. Pyro-cumulus clouds are very unique in their microphysical structure.

[1] Definition provided by M. D. Fromm, personal communication, cf. also `http://en.wikipedia.org/wiki/Pyro-Cumulonimbus`

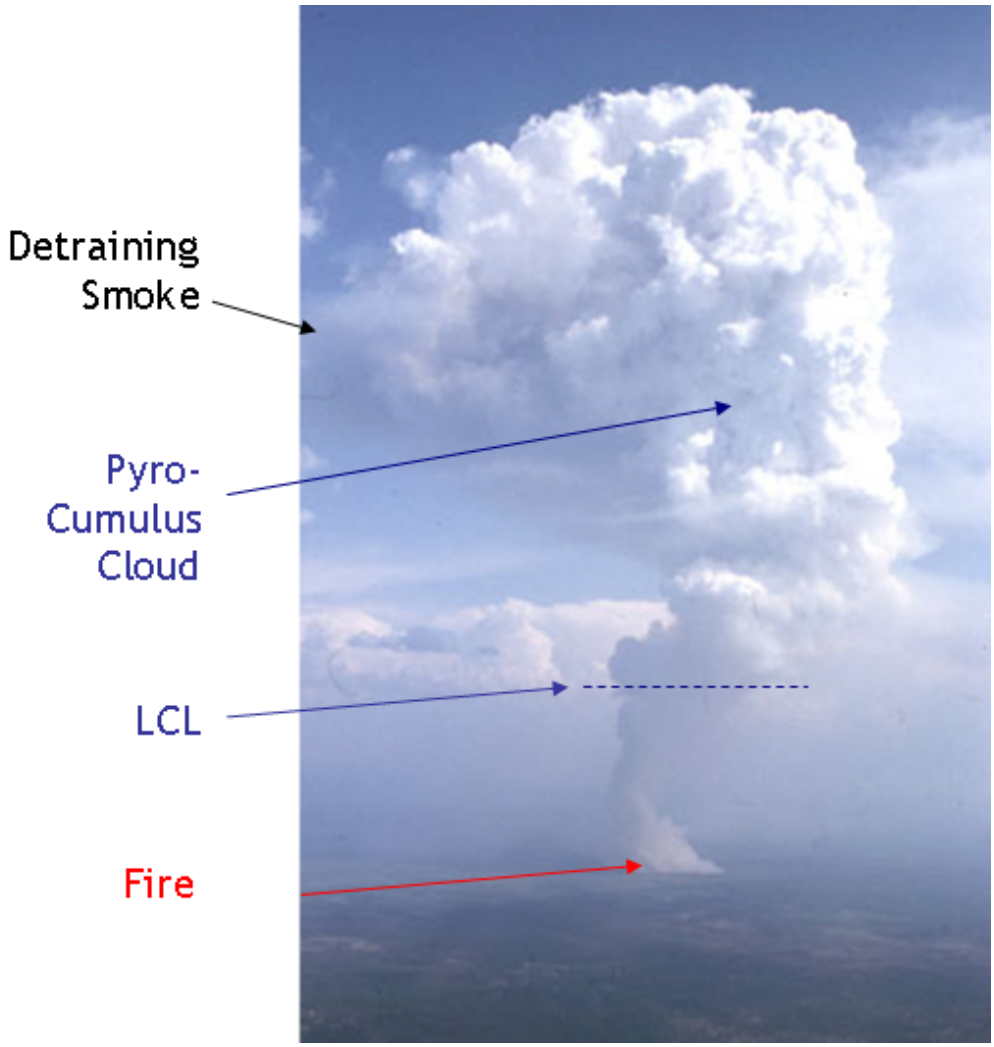

Figure 1.1: Schematic illustration of pyro-cumulus convection based on a photograph of the Bor Fire [*FIRESCAN Science Team*, 1996]

.

This can be attributed to two effects. First of all, the aerosol particles emitted by the fire can act as cloud condensation nuclei (CCN). Since a large number of CCN compete for a given amount of condensable water vapor, pyro-cumulus are characterized by large concentrations of small cloud droplets [e.g., *Andreae et al.*, 2004].

The second effect is related to the more vigorous dynamics induced by the fire. The additional buoyancy generated by the fire heating produces very strong updrafts. This enhances the supersaturation at the cloud base and further increases the number of aerosol particles activated. Moreover, due to the large vertical velocities, individual air parcels entering the pyroCb at the cloud base reach the

detrainment level at the cloud top after substantially shorter time than in regular thunderstorm clouds, hence leaving only little time for microphysical processes within the cloud's updraft.

Below a threshold radius of about 10-15 μm, cloud droplets are very inefficient in growing into precipitation sized hydrometeors through the collision and coalescence mechanism [*Pruppacher and Klett*, 1997]. The small droplet size in combination with the large updraft velocities therefore lead to efficient suppression of rain formation in pyroCbs. Despite strong vertical development, pyroCbs are often observed to result in little or no precipitation other than large hailstones [*Fromm et al.*, 2006; *Rosenfeld et al.*, 2007].

While the absolute concentration of CCN is extremely high in pyroCbs, the fraction of aerosol particles activated into cloud droplets is rather small. Typically, at cloud base, a major fraction (about 90-99 %) of the aerosol particles in pyro-cumulus remains in the interstitial phase, i.e., in between the cloud droplets, without becoming activated (Martin Simmel, personal communication). Much of the aerosol entering the pyro-cumulus at the cloud base is observed to detrain at the cloud top without becoming washed out during the cloud processing [*Reid and Hobbs*, 1998; *Andreae et al.*, 2004]. Hence, these clouds appear to be "smoking".

Forest fires are a very important source of trace gases and particulate matter in the atmosphere [*Crutzen and Andreae*, 1990]. Due to the co-location of efficient vertical transport with the release of large amounts of smoke, fire-caused convection ("pyro-convection") results in direct injection of smoke into the free atmosphere and thus is a very important mechanism for atmospheric chemistry. Large scale transportation patterns as well as chemical and physical transformation mechanisms often depend critically on the injection height [*Lavoué et al.*, 2000].

Jaffe et al. [2004], for instance, documented an event where forest fire smoke was injected into the free troposphere in Siberia and underwent long range transport across the Pacific to North America and resulted in strong enhancements of CO, O_3, and aerosol loading over large parts of the American continent. *Colarco et al.* [2004] report an event of forest fire smoke transport from Quebec eventually mixing with the turbulent planetary boundary and resulting in significant air quality impairments in the Washington D.C. area several days after injection. Similarly, *Hodzic et al.* [2006, 2007] analyzed the spread of smoke originating from wildfires in the Mediterranean basin during the European heatwave in 2003. Based on chemical transport modeling they found that if injection heights are represented realistically, these fires resulted in a substantial enhancement of particulate matter loading over a large part of Europe, a strongly negative radiative forcing at the

surface, and a decrease of photolysis rates responsible for ozone production.

1.4 Modeling of pyro-convection

The major goal of the work undertaken as part of this dissertation was (1) to investigat the physical properties of pyroCbs and (2) to identify the relevant parameters and mechanisms that determine the vertical development and the occurrence of troposphere-to-stratosphere transport. For this purpose, the Chisholm forest fire (see Chapter 2), likely the best-studied and documented pyroCb event ever reported in the scientific literature, was used as a case study.

The simulations presented here are the first ever convection scale modeling study of the newly discovered phenomenon of troposphere-to-stratosphere transport induced by wildfires. Previous modeling studies of convective injection of particulate matter into the lower stratosphere focused on volcanic eruptions [e.g., *Graf et al.*, 1999; *Herzog et al.*, 1998; *Textor et al.*, 2006a,b], or firestorms following nuclear explosions [*Penner et al.*, 1986; *Small and Heikes*, 1988].

Modeling studies such as the one presented here allow us to assess physical quantities that are inaccessible to direct observations. PyroCbs tend to be very vigorous, they occur infrequently and are typically not anticipated. Therefore, there have not yet been any in-situ observations such as aircraft measurement of pyroCbs. The only source of observational information is remote sensing, most importantly observations performed by satellite radiometers (e.g., AVHRR, see Chapter 2) and ground based radar. The Chisholm fire pyroCb occurred fortuitously under good coverage of such remote sensing instruments. From these observations, it was possible to retrieve valuable information on the cloud shape, cloud top temperature structure, anvil altitude, and microphysics [Chapter 2, *Rosenfeld et al.*, 2007]. These observations, however, do not capture quantities such as the fields of temperature, winds, water vapor and aerosol concentration within the cloud. Model simulations, by contrast, allow us to produce a 'virtual' pyroCb and to take a closer and more detailed look at these quantities of interest in order to better understand the physical structure. Furthermore, it is possible to introduce idealized, inert tracers in the model simulations in order to assess flow patterns, vertical exchange of air masses and transport of smoke in detail (Section 3.4.4).

Model simulations also enable us to conduct sensitivity studies by modifying model parameters, initial and boundary conditions or by disabling certain processes. Such sensitivity studies are a valuable tool for assessing the causal connection between various parameters and processes and the physical properties of the system. The sensitivity studies presented in Chapter 5 allow us to identify the

relative importance of various parameters for the pyroCb's development, namely the fire release of sensible heat, the fire release of latent heat, the fire emission of aerosol acting as CCN, and background meteorology. The strong dependence of the atmospheric impact on smoke injection height, as discussed in Section 1.3, underlines the importance of analyzing the vertical development of pyro-convection as a function of the relevant fire and atmospheric parameters by studies on the spatial and temporal scale of convection.

It is important to critically assess the model results in view of its limitations and uncertainties. While there are also uncertainties induced by the model approach itself (cf. Section 3.2), the uncertainty of the simulations presented here is largely dominated by the uncertainty in input parameters such as those related to background meteorology and fire activity. Based on the sensitivity studies, it is possible to analyze how strongly the results depend on certain input parameters (Chapter 5). Furthermore, comparison between model results and observations are used to assess the model performance (Chapters 3 and 4).

This thesis is structured as follows. Chapter 2 reviews the available observational information on the Chisholm fire pyroCb, the background meteorology at the time of the most extreme phase of pyroCb convection, and the pyroCb's atmospheric impact. In the following chapter, Chapter 3, the model setup and results for the reference simulation of the Chisholm pyroCb are described and compared to the observational findings. In Chapter 4 it is shown that small-scale transport processes played an important role in enhancing troposphere-to-stratosphere transport of biomass smoke by the Chisholm pyroCb, and that there is a connection between these small-scale transport processes and the observed cloud top temperature structure. In Chapter 5, a series of sensitivity studies is presented. These simulations demonstrate that the dynamics of the pyroCb is mostly sensitive to the fire release of sensible heat and parameters related to background meteorology, while the fire release of latent heat and aerosol particles acting as cloud condensation nuclei (CCN) is of less significance. Based on more general considerations, Chapter 6 makes the point that, in contrast to a recently published hypothesis, fire-released moisture does not have a strong effect on pyroCb dynamics. A summary, concluding remarks and an outlook are given in Chapter 7.

Much of the work presented here has been published as scientific journal articles or has been submitted for publication. Chapters 4, 5, and 6 of this dissertation are each largely based on individual scientific articles [*Luderer et al.*, 2007b, 2006, 2007a, respectively]. Chapters 2 and 3 are partly based on G.L.'s contributions to *Rosenfeld et al.* [2007] and *Trentmann et al.* [2006], respectively.

Chapter 2

Observations of the Chisholm pyro-cumulonimbus[1]

Abstract. Both in terms of fire intensity and atmospheric impact, the Chisholm fire is one of the most extreme cases of wildfire activity ever recorded in scientific literature. A wealth of observational information on the Chisholm fire is available. In this chapter, the knowledge on the meteorological background conditions and the characteristics of the Chisholm fire, and its atmospheric impacts are reviewed. The observations in conjunction with meteorological analysis show that the severe intensification of the fire activity and pyroCb convection coincided with the arrival of a synoptic scale cold front. The maximum cloud height was approximately 13.5 km. Analysis of the microphysical structure reveals that the pyroCb was extremely continental, i.e., characterized by a large number of small cloud droplets. Precipitation formation in the pyroCb's updraft region was efficiently suppressed.

2.1 Introduction

The Chisholm fire is arguably the best-studied case of wildfire-induced pyro-cumulonimbus convection. There is a wealth of observational information available for the Chisholm fire. It was fortuitously captured by various satellite observations and meteorological radar. In addition, detailed information is available on the characteristics of the forest fire, such as the pattern and rate of spread, the amount of fuel consumed and the fire intensity.

[1]This Chapter is partly based on the manuscript "The Chisholm firestorm: observed microstructure, precipitation and lightning activity of a pyro-cumulonimbus" by D. Rosenfeld, M. Fromm, J. Trentmann, G. Luderer, M. O. Andreae, and R. Servranckx, published in Atmospheric Chemistry and Physics [*Rosenfeld et al.*, 2007].

Figure 2.1: Photograph of the Chisholm pyroCb taken from a firefighting aircraft at 0130 UTC (1930 local time), shortly after the major explosive growth of the convection started. Credit: Alberta Government.

In a pioneering study, *Fromm and Servranckx* [2003] were the first to document direct injection of forest fire smoke into the lower stratosphere by pyroCb convection from analysis of satellite observations of the Chisholm Fire and the subsequent stratospheric impact. The Total Ozone Mapping Spectrometer's aerosol index (TOMS-AI) is very sensitive to opaque aerosol layers with high absorptivity in the UV, and the sensitivity increases with increasing altitude [*Fromm et al.*, 2007a]. The TOMS-AI is therefore excellently suited for the detection of forest fire smoke transport into the UT/LS region by pyroCb convection. In the aftermath of the Chisholm pyroCb, the TOMS-AI reached values of up to 32 – the largest ever recorded. Further observational studies on the characteristics of the pyroCb and its subsequent stratospheric impact followed [*Rosenfeld et al.*, 2007] or are under way [*Fromm et al.*, 2005, 2007a,b].

The focus of this chapter is on the observational information relevant for the modeling studies presented in the following chapters.

2.2 Fire observations

The Chisholm Fire (tagged LWF-063), a man-caused forest fire, was ignited on 23 May 2001 at about 55° N, 114° W, approx. 160 km north of Edmonton, Alberta,

Canada. In the afternoon of 28 May, a second fire was started (LWF-073) and later merged with Fire 063. Favorable weather conditions, in particular a strong low-level jet, and dry fuel led to erratic fire behavior and intense convection on 28 May, especially in the late afternoon and early evening.

Fire intensity maximized on this day between about 17:00 and 24:00 MDT (Mountain Daylight Time), i.e., between 23:00 UTC and 06:00 UTC. During this time span, a total area of more than 50 000 ha was impacted by the fire. The average rate of spread was observed to be $5.4\,\mathrm{km\,h^{-1}}$=($1.5\,\mathrm{m\,s^{-1}}$). Figure 2.1 shows a photograph taken during the mature phase of pyroCb convection. The main types of fuel burned (according to the Canadian Forest Fire Behavior Prediction (FBP) System) were boreal spruce and grass, which include substantial amounts of soil and duff. The fuel density in the area that burned during the time of peak fire activity is rather inhomogeneous. In its southern part, it is dominated by dense coniferous vegetation, while there are extended patches of grasslands in the northern part of the area burned. Field sampling conducted after the fire yielded a fuel consumption of $9.4\,\mathrm{kg\,m^{-2}}$ for the spruce forest [*ASRD*, 2001]. Averaged over the entire area burned, the estimated fuel consumption at the time of the peak intensity is $7.6\,\mathrm{kg\,m^{-2}}$. The Fine Fuel Moisture Code (FFMC) and the Duff Moisture Code (DMC) of the Canadian Forest Service, which are measures of the moisture content of the fine fuel and the duff, respectively, were estimated to be 92.8 and 99, respectively. These values correspond to moisture contents of fine fuel and duff of 8% and 49% of the dry fuel mass, respectively [*Van Wagner*, 1987]. Considering the large consumption of duff of up to about 90% [*ASRD*, 2001], an overall fuel moisture content of the burned biomass of 40% of the dry fuel mass was employed for the modeling studies conducted.

The average head fire intensity during the time of maximum fire activity was about $1.9\times10^8\,\mathrm{W\,m^{-1}}$, with a peak value of $2.4\times10^8\,\mathrm{W\,m^{-1}}$ in the southern part of the fire front that is vegetated with spruce forest and was therefore characterized by higher fuel consumption.

The total energy release due to combustion has been calculated from the average fuel burned, the affected area, and the standard heat of combustion ($18\,700\,\mathrm{kJ\,kg^{-1}}$, *ASRD*, 2001). For the 7 hours of maximum intensity this yields an overall energy release of about 71×10^9 MJ. The explosive yield of TNT, which is the standard unit that nuclear yields are expressed in, is 4.2×10^9 MJ per million ton (MT) of TNT. This means that the energy release of the Chisholm fire is about equivalent to 17 large hydrogen bombs with a yield of 1 MT or about 1200 Hiroshima-size bombs.

Even though the heat release from the fire is enormous, the model simulations

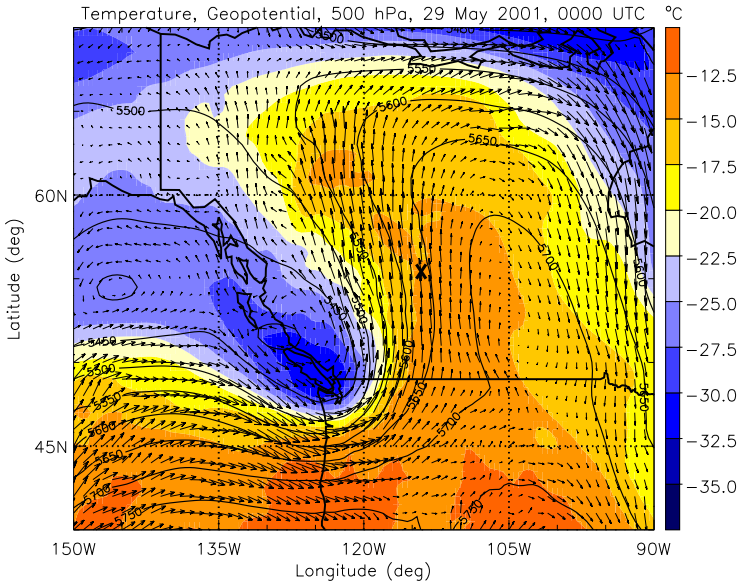

Figure 2.2: Temperature (color scale), geopotential height (m, black contours), and wind field (arrows) at 500 hPa from ECMWF analysis data for 29 May 2001, 00:00 UTC. The location of the Chisholm fire is depicted by the black cross at 55° N, 114° W.

presented in the following chapters show that the energy released from condensation and freezing of ambient and fire-released water vapor exceeds the fire heating by about a factor of three (cf. Chapter 3).

2.3 Meteorological situation and fire development

The meteorological situation on 28 May 2001 over Canada was characterized by a strong 500-mb ridge with its western edge extending from about 45° N to 60° N along about 115° W (Figure 2.2).

Southerly winds were present along the ridge at all levels. The low level winds transported warm and moist airmasses towards the Chisholm area inducing unstable atmospheric conditions (Figure 2.3). West of the Chisholm area a local low pressure area formed with an associated trough and cold front that moved towards the fire area [*ASRD*, 2001].

The temporal evolution of the fire behavior and its connection to meteorological conditions can be reconstructed from the sequence of satellite images recorded by GOES, radar observations recorded at Edmonton (cf. Section 2.4), as well as fire behavior reports in *ASRD* [2001]. A first convective line of isolated cumulonimbus, associated with the upper trough, reached the fire plume at 20:30 UTC

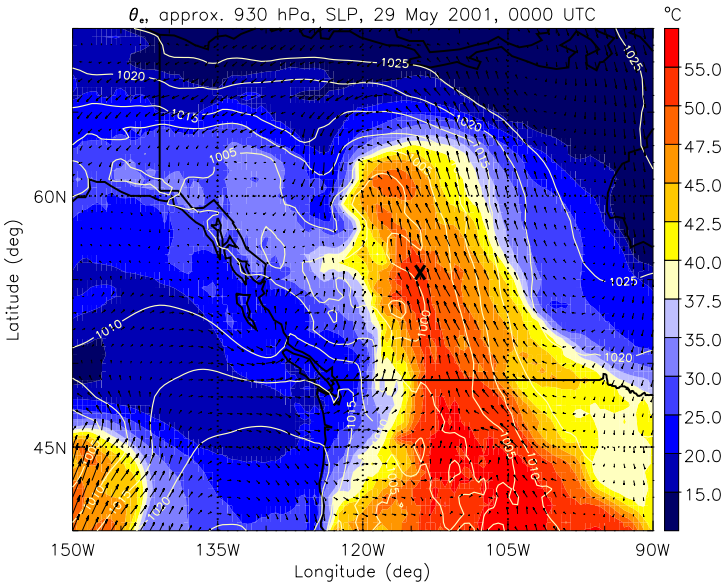

Figure 2.3: Equivalent potential temperature, θ_e, (color scale), normalized surface pressure (hPa, white contours), and wind field (arrows) at the 9th level of the vertical hybrid coordinate system (approx. 930 hPa) from ECMWF analysis data for 29 May 2001, 00:00 UTC. The location of the Chisholm fire is depicted by the black cross at 55° N, 114° W.

(=14:30 MDT). Strong south-easterly surface wind prevailed after the passage of this first convective line. The maximum surface temperature reached 28°C with a minimum relative humidity of 25% indicating high fire risk [*ASRD*, 2001]. As a result of the unstable airmass behind the first line of Cb, a second line of intense convection approached the fire area from southerly directions at about 23:00 UTC (=17:00 MDT). This convective line was more intense with maximum altitudes of radar reflectivity of about 10 km and widespread thunderstorm activity. A peak wind gust, influenced by downdrafts of the passing thunderstorm at the surface, of 92 km h^{-1} was measured at 00:00 UTC [*ASRD*, 2001].

During the passage of the first convective line, the fire-induced convection started to veer, but did not intensify. The fire-induced convection was substantially intensified between 23:30 UTC and 02:30 UTC, when the second convective line approached the fire [*Rosenfeld et al.*, 2007]. Two distinctively intense pyroCbs (blow-ups) were observed in this time frame. The first occurred between 23:30 UTC and 00:30 UTC with maximum echotop heights measured by the radar of about 12 km. The second blow-up occurred between 01:20 UTC and 02:30 UTC with the arrival of the second line of convection at the fire location. Radar observations yield maximum heights for this pyro-convection between 13 km and

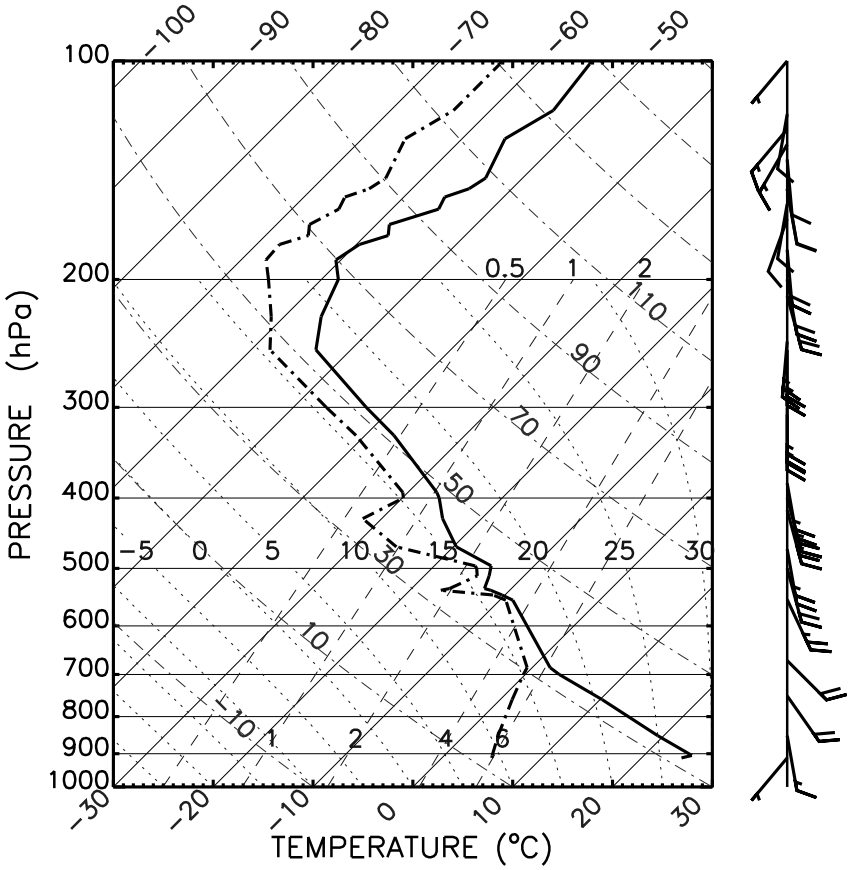

Figure 2.4: Vertical profiles of temperature and dew point temperature used for the initialization of the model simulations.

14 km. Satellite observations at 02:00 UTC on 29 May 2001 show a well developed convective cloud anvil covering an area of about 50 km×100 km [*Rosenfeld et al.*, 2007]. An overshooting region slightly north of the fire on top of the anvil and gravity wave-like structures in the anvil are also visible. Other features of this pyro-convection include an anomalously high number of positive lightning strikes [*Rosenfeld et al.*, 2007]. In the present work, we focus on the second of this pair of intense pyro-convection events.

Figure 2.4 presents measurements taken from a radiosonde launched near Edmonton, Alberta (WMO Station Identifier 71119; 53.55° N, 114.10° W) on 29 May 2001 at 00:00 UTC (available at `http://raob.fsl.noaa.gov/`). These measurements, taken approx. 200 km south of the Chisholm fire, are representative of the conditions before the second line of convection had reached Chisholm. While the atmospheric boundary layer was not particularly moist (absolute humidity q_v=6 g kg^{-1}), the middle troposphere above 700 hPa (corresponding to 3000 m

above sea level (asl)) was almost saturated. Below 700 hPa the temperature approximately followed a dry adiabatic decrease with altitude, above 700 hPa the lapse rate was slightly larger than the moist-adiabatic lapse rate.

With its rather low convective available potential energy (CAPE) of 131 J kg^{-1}, this profile does not indicate the potential for extreme convection, whereas the value for the convective inhibition (CIN) of 26 J kg^{-1} suggests easy initiation of convection. The lifting condensation level (LCL), the level of free convection (LFC), and the level of neutral buoyancy (LNB) of the background profile are located at 3250 m, 3620 m, and 7410 m respectively. The 0 °C-level is at about 3400 m, i.e., close to the LCL. The thermal tropopause based on the WMO-definition is located at 12.3 km, corresponding to a pressure of 180 hPa and a potential temperature of 345 K. Based on ECMWF analysis data, the dynamical tropopause (PV=2 PVU) was located at a potential temperature of θ=332 K, corresponding to an altitude of z=11.2 km and a pressure of p=225 hPa. Here, we chose to use the PV-definition of the tropopause, because it is more meaningful for studies of the troposphere-stratosphere exchange in mid-latitudes [e.g., *Holton et al.*, 1995; *Stohl et al.*, 2003].

2.4 Properties of the Chisholm pyroCb

The Chisholm pyroCb was captured by several satellite instruments. Observations of the Chisholm pyroCb are available from the Advanced Very High Resolution Radiometer (AVHRR), the Defense Meteorological Satellite Program (DMSP) and the Geostationary Operational Environment Satellite (GOES-8). Fortunately, the Chisholm fire also occurred under good coverage of the Edmonton weather radar, stationed about 200 km south of the fire location. These observations provide unique insights into the dynamics and structure of the pyroCb development.

2.4.1 Temporal development and vertical structure

These satellite observations consistently show that the convective "blowup" of the fire convection into a massive pyroCb coincided with the arrival of a synoptic cold front. This finding is also supported by the radar time series.

Figure 2.5 depicts AVHRR images taken during an overpass at 0220 UTC, nicely capturing the mature phase of the pyroCb convection. Several fires burned in the Chisholm region on 28 May 2001. The false-color composite image shown in Figure 2.5(a) was created with red, green and blue used for radiances in the 3.7 μm, 0.9 μm and 0.64 μm channels, respectively. Due to the thermal radiation

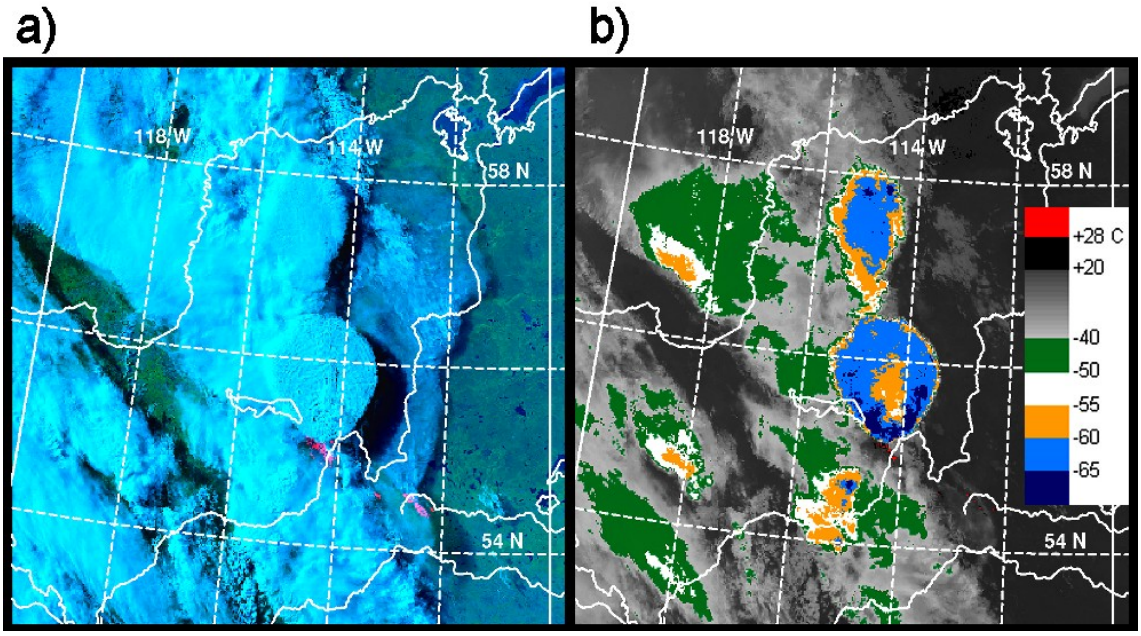

Figure 2.5: AVHRR observations of the mature phase of the Chisholm pyroCb recorded at 0220 UTC. (a) is a false-color composite image with red, green and blue used for radiances in the 3.7 μm, 0.9 μm and 0.64 μm channels, respectively. (b) shows brightness temperatures recorded at 10.8 μm. This figure is reproduced from [*Fromm and Servranckx*, 2003]

emitted at 3.7 μm, the fire locations therefore show up as distinct red hot spots. A pair of pyroCb cells are clearly visible in the center of the picture as massive thunderstorm clouds. While the northern cell has been already advected away from the fire, the even more intensive southern convection cell is still attached to the fire. The strong solar illumination from the low-standing sun results in shadowing and nicely highlights the cloud's structure. The flattening of the anvils due to the tropopause inversion is clearly visible. The lengths of the shadows indicate that the central pyroCb reaches much higher than the clouds in the ambient convection. The pyroCb's are embedded in a cloud band stretching from south to north. Analysis of the meteorological situation and GOES satellite images (not shown) confirms that the sudden intensification of the pyro-convection into a massive pyroCb coincided with the arrival of a synoptic scale cold front. The cloud top brightness temperature observed in the 10.8 μm channel of the AVHRR (Figure 2.5b) reveals that the coldest cloud top brightness temperatures at the southern edge are substantially lower than the tropopause cold point recorded by the Edmonton radiosonde (Chapter 2.3). At the same time, the maximum cloud top brightness temperatures measured in the center of the pyroCb are much warmer than the temperatures anywhere at the tropopause level. This indicates that the pyroCb

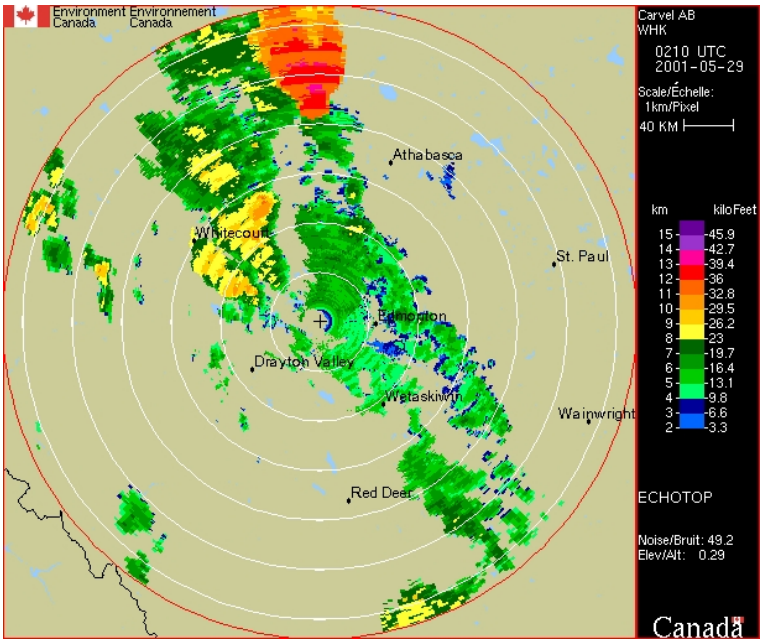

Figure 2.6: radar echotop height image capturing the mature phase of pyro-Cb convection. The maximum pyroCb activity is reached at the time of arrival of a cold front. The pyroCb (red) is clearly discernible from the rainband (green) associated with the approaching cold front. Credit: Environment Canada.

reaches well into the lower stratosphere. A detailed analysis of the pyroCb's cloud top temperature based on the model results is provided in Chapter 4.

The cloud top altitude of the Chisholm pyroCb can be independently estimated using several methods: analysis of cloud top temperature at the anvil level and comparison with the background temperature profile, analysis of echotop heights as measured by radar (cf. Chapter 2.4.2), and calculation based on shadow length and the geometry of solar illumination. *Rosenfeld et al.* [2007] conclude that the various methods consistently show that the cloud top reached to about 13.5 km, more than 2 km above the dynamical tropopause.

2.4.2 Microphysical structure

Rosenfeld et al. [2007] analyzed radar observations, radiometric satellite imagery and rain gauge measurements of the Chisholm pyroCb. They used this observational information to characterize the pyroCb's microphysical properties and to analyze its vertical development.

Figure 2.6 shows a radar image depicting echo top heights, i.e., the maximum altitudes at which the RADAR recorded reflection signals, during the phase of mature pyroCb convection. These echotop heights give a good indication of the

cloud top heights and clearly show that the pyroCb (red) reached substantially higher than ambient convective clouds without fire forcing.

Despite the very strong vertical development of the pyroCb, the radar reflectivities within the region where the pyroCb reaches the maximum height are rather weak. Since radar reflectivity scales with the sixth power of the droplet radius [e.g., *Rogers and Yau*, 1989], this is a clear indication of the small hydrometeor sizes and the inefficient precipitation formation within the pyroCb's updraft region [*Rosenfeld et al.*, 2007]. *Rosenfeld et al.* [2007] also used the AVHRR to retrieve the size of the cloud ice particles in the pyroCb's anvil. According to this analysis, the hydrometeor effective radius in the pyroCb is about 5-10 μm, while ambient clouds that are not affected by the fire are characterized by much larger effective radii and hence are much more efficient in forming precipitation.

The small size of cloud droplets in the updraft region has important implications for the cloud glaciation. Immersion freezing, the dominant mode of heterogeneous freezing, relies on suitable ice nuclei (IN) to initiate freezing. The probability of the presences of an IN within an individual droplet scales with the droplet volume – small droplets are therefore much less likely to undergo heterogeneous freezing. In extreme cases of microphysically continental clouds with small droplet sizes, a major fraction of the cloud water content is therefore observed to remain liquid until the level of homogeneous freezing at about $-39°$C [*Rosenfeld and Woodley*, 2000]. The freezing level derived from the radar observations of the Chisholm pyroCb is at 8.5 km, in good agreement with the homogeneous freezing level according to the RAOB sounding. This finding indicates that heterogeneous freezing was efficiently suppressed, and has important implications for the effect of the fire CCN on the pyroCb dynamics as discussed in Chapter 5.4.4.

Rosenfeld et al. [2007] also discuss another peculiar feature concerning the electrical activity of pyroCbs: while the lightning produced in ordinary thunderstorms is typically dominated by negative lightning flashes, most of the flashes observed in pyro-clouds are positive [*Jungwirth et al.*, 2005]. Similarly, for the time from 28 May 2300 UTC until 29 May 0300 UTC, the time of maximum pyro-convection, the record of the Canadian Lightning Detection Network (CLDN) recorded a strong dominance of positive flashes in the area of the Chisholm fire, whereas ambient clouds that were not ingesting smoke from the fire produced mostly negative flashes. The reason for this anomaly is not entirely understood. Possible explanations of this behavior are the chemical composition of the smoke [*Jungwirth et al.*, 2005] or the microphysical anomaly of pyroCbs, with exceptionally high amounts of supercooled water at greater heights and lower temperatures [*Rosenfeld and Woodley*, 2000].

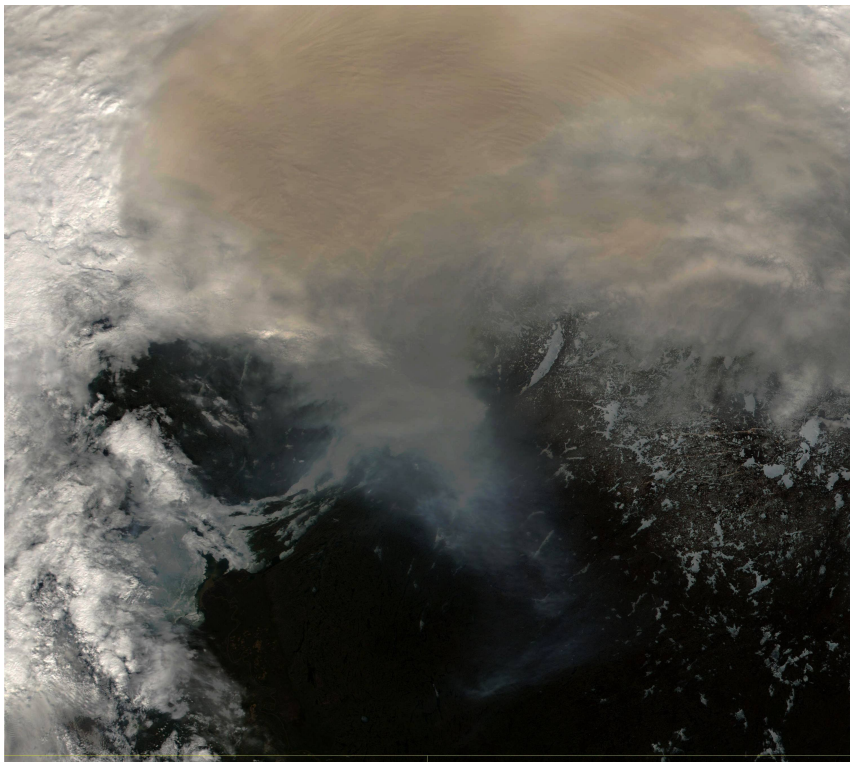

Figure 2.7: True color image of the smoke plume generated by the Chisholm pyroCb as observed by the Moderate Resolution Imaging Spectroradiometer (MODIS) onboard the Terra satellite over the Canadian Northwest Territories on 29 May 2001, 1840 UTC, the day after the pyroCb event. The smoke appears as yellowish-brownish fog. An analysis of the MISR instrument onboard the same satellite reveals that the smoke plume was located at about 12 km. The size of the image is roughly 1000 km ×1000 km.

2.4.3 Large scale impact

With the help of GOES-8 satellite observations, the transport of the fire smoke within the upper troposphere/lower stratosphere region was traced [*Fromm and Servranckx*, 2003]. The plume was transported by the upper level wind fields towards the north and, at about 15:00 UTC on 29 May 2001, turned eastward, north of 60° N. On 29 May 2001, 18:40 UTC, the Moderate Resolution Imaging Spectroradiometer (MODIS) and the Multi-angle Imaging SpectroRadiometer (MISR), both aboard the TERRA satellite, observed the smoke plume about 1200 km north of Chisholm (Figure 2.7). Using the information from MISR's different viewing angles, the maximum height of the smoke layer was determined to be about 12 km, i.e, well within the stratosphere (`http://eosweb.larc.nasa.gov/HPDOCS/misr/misr_html/chisholm_forest_fire.html`, Fromm et al. 2007b). On 01 June, the POAM satellite instrument encountered the Chisholm plume over Quebec and ob-

served a strong enhancement of extinction in the lower stratosphere, peaking at an altitude of 12 km, which corresponds to a potential temperature of 355 K. Over the course of the following months, the Chisholm plume was spread and advected within a latitude band ranging from 20°N to about 80°N and was observed by numerous satellite occultation and ground-based lidar measurements. These measurements show that the potential temperature levels of the smoke plume increased over time, with maximum values as high as 458 K observed in July of 2001. The continuous increase in potential temperature indicates the presence of diabatic processes such as solar heating due to the large concentration of absorbing aerosol within the plume. The zonal average aerosol optical depth in the lower stratosphere exceeded the background level by a factor of two [*Fromm et al.*, 2007a]. Since there were no volcanic eruptions in the relevant time frame and Chisholm remained the only pyroCb event with stratospheric impact, the observed enhancement in stratospheric aerosol can be attributed exclusively to the three hours of Chisholm pyroCb convection.

2.5 Summary and Conclusions

The wealth of observational data and reports on the Chisholm fire provide valuable insights into the structure and dynamics of the Chisholm fire and the associated development of pyroCb convection. Key findings from the observations include:

- The Chisholm forest fire was extremely vigorous with maximum values of the fire intensity of about $2.4\times10^8\,\mathrm{W\,m^{-1}}$
- The Chisholm fire as well as the pyroCb convection reached its maximum intensity shortly before the arrival of a synoptic scale cold front.
- Several methods of estimating the maximum cloud height consistently show that the cloud top altitude was about 13.5 km above sea level.
- The cloud top brightness temperature structure observed from satellite reveals a warm region in the center of the anvil surrounded by a u-shaped cold region.
- Due to the large abundance of fire aerosols acting as cloud condensation nuclei, the Chisholm pyroCb was characterized by an extremely continental microphysical structure. In conjunction with the very high vertical velocities in the updraft leaving little time for droplet growth, this lead to an efficient suppression of precipitation formation within the updraft region.

- The Chisholm pyroCb resulted in a lower stratospheric aerosol plume that persisted at potential temperature levels of up to 458 K for at least three months, traveled around the world several times and led to a two-fold increase in zonal average stratospheric aerosol burden.

The modeling study presented in the following chapters is aimed at verifying the observed features of the Chisholm pyroCb, analyzing its structure and enhancing the understanding of the physical mechanisms. Chapter 4 provides an explanation for the observed cloud top temperature structure and discusses implications for troposphere-to-stratosphere transport. Chapters 5 and 6 analyze the relative importance of fire release of sensible heat, latent heating from fire moisture and water vapor entrained from the environment, interactions between cloud-microphysics and dynamics as well as the role of the meteorological conditions due to the passage of the cold front.

Further investigations on the long term and large scale impacts of the Chisholm pyroCb are underway [*Fromm et al.*, 2007a,b]. Together with other observational studies of pyroCb convection [*Fromm et al.*, 2005, 2006] and measurements of biomass-burning related trace gases and particulate matter in the lower stratosphere, these findings confirm that deep convective transport of forest-fire smoke into the stratosphere occurs regularly at mid- and high latitudes and has a profound impact on stratospheric chemistry.

Chapter 3

Reference simulation[1]

Abstract. This chapter presents results from the reference simulation for a case study of the pyro-cumulonimbus cloud (pyroCb) that developed over Chisholm, Alberta, Canada on 28 May 2001. For this study, the three dimensional cloud resolving model ATHAM (Active Tracer High Resolution Atmospheric Model) was used. The initialization of the background meteorology was based on radiosonde observations. Information on the fire forcing was obtained from ground-based observations of the mass and moisture of the burned fuel.

The simulated structure is in good agreement with observations of the pyroCb. The model simulation shows intensive convection with an overshoot above the tropopause, which was located at 11.2 km and a potential temperature level of 332 K. According to the model simulations, the pyro-convection reached an altitude of 12.5 km, which is slightly lower than the maximum altitude obtained from observations (13.5 km). While the main outflow from the pyro-convection occurs at about 10.6 km, a significant fraction (about 8% after 40 min and 11% after 50 min simulation time) of the emitted mass of smoke aerosol is transported beyond the tropopause isentrope and reaches the lower stratosphere. According to the simulations, the pyroCb is characterized by extremely continental microphysical conditions. Volume mean radii within the updraft region are as low as 3 μm. In the updraft region, precipitation formation is efficiently suppressed. These findings are consistent with the observations.

In contrast to regular convection, the region of maximum updraft velocity in the pyro-convection is located close to the surface above the fire. This results in

[1]This Chapter is partly based on G.L.'s contribution to the manuscript "Modeling of biomass smoke injection into the lower stratosphere by a large forest fire (Part I): Reference study" by J. Trentmann, G. Luderer, T. Winterrath, M. Fromm, R. Servranckx, C. Textor, M. Herzog, H.-F. Graf, and M. O. Andreae, published in Atmospheric Chemistry and Physics [*Trentmann et al.*, 2006].

high updraft velocities $>10\,\mathrm{m\,s^{-1}}$ at the cloud base. The temperature anomaly in the plume decreases rapidly with height from values above 50 K at the fire to about 5 K at about 3000 m above the fire. An analysis with idealized inert tracers exhibits significant entrainment of environmental air into the pyroCb at low and mid-tropospheric levels.

While the sensible heat released from the fire is responsible for the initiation of convection in the model, the release of latent heat from condensation and freezing dominates the overall energy budget. Emissions of water vapor from the fire do not significantly contribute to the energy budget of the convection.

3.1 Introduction

Whereas there is some observational information on pyro-convection, very limited research has been conducted using numerical models. Most of the previous approaches to simulate convection induced by a fire or other surface heat sources have been performed with simplified models. Based on observations, *Lavoué et al.* [2000] derive a linear correlation between the injection height and the fire intensity. Buoyant plume and parcel models are used to estimate the height of the pyro-convection [e.g., *Morton et al.*, 1956; *Manis*, 1985; *Jenkins*, 2004]. Two-dimensional axis-symmetric models including simple cloud parameterizations were used for a more detailed description of the transport and entrainment [e.g., *Small and Heikes*, 1988; *Gostintesev et al.*, 1991]. The first three-dimensional model simulations of fire plumes were presented by *Penner et al.* [1986] for rather idealized scenarios and for the pyro-convection induced by the Hardiman Fire [*Penner et al.*, 1991]. Results from the latter simulation were combined with a parcel model to investigate the scavenging of smoke aerosol and cloud formation [*Chuang et al.*, 1992]. Recently, *Cunningham et al.* [2005] presented results from detailed simulations of the small scale dynamical interaction between the fire-induced buoyancy and the atmospheric wind.

In parallel to these models, which focus on the pyro-convection, numerical models that include the interaction between the atmosphere and fire have been developed and applied [e.g., *Clark et al.*, 1996, 2004; *Linn et al.*, 2005]. These kinds of models, however, do not resolve the full dynamical evolution of deep pyro-convection involving cloud formation, and are not easily applicable to atmospheric studies.

The first detailed comparison of model results with field observations from a young biomass burning plume was presented by *Trentmann* [2001]; *Trentmann et al.* [2002]. They used observed atmospheric profiles of temperature, moisture

and wind combined with information on the fire emissions to simulate the pyro-convection induced by the prescribed Quinault fire [*Hobbs et al.*, 1996]. Chemical processes leading to the formation of tropospheric ozone were also investigated [*Trentmann et al.*, 2003a]. In the case of the Quinault fire, the convection was not particularly intense, no cloud was formed, and the smoke aerosol remained in the boundary layer.

Here, we will present model simulations for the pyro-convection induced by the Chisholm fire [*Fromm and Servranckx*, 2003; *Rosenfeld et al.*, 2007]. This pyro-convection transported the fire emissions into the upper tropospheric region and into the stratosphere. The pyroCb-convection and the resulting stratospheric aerosol plume have been observed by radar and satellite [*Fromm and Servranckx*, 2003; *Rosenfeld et al.*, 2007]. This paper presents relevant information on the model and its initialization. Results from model simulations using the best available data for the meteorological conditions and the fire emissions are shown and evaluated with field observations. Some dynamical features of the simulated pyroCb are discussed. In Chapter 5, results from sensitivity studies exploring the impact of the fire emissions (sensible heat, water vapor, and CCN) and the ambient background profiles on the simulated pyroCb are presented [cf. also *Luderer et al.*, 2006].

3.2 The ATHAM Model

3.2.1 Model description

The non-hydrostatic active tracer high resolution atmospheric model (ATHAM) [*Oberhuber et al.*, 1998; *Herzog*, 1998; *Herzog et al.*, 2003] is used to simulate the pyro-convection induced by the Chisholm fire. ATHAM was originally designed and applied to simulate eruptive volcanic plumes [*Graf et al.*, 1999]. It was used to investigate the particle aggregation in an explosive volcanic eruption [*Textor et al.*, 2006b], the impact of latent heat release and environmental conditions on the volcanic plume rise [*Herzog et al.*, 1998; *Graf et al.*, 1999], and the stratospheric injection of trace gases by explosive volcanic eruptions [*Textor et al.*, 2003]. It was also employed to simulate the transport of fire emissions [*Trentmann et al.*, 2002] and the chemical processes leading to photochemical production of tropospheric ozone [*Trentmann et al.*, 2003a]. Moreover, results obtained from ATHAM simulations were used to investigate three-dimensional radiative effects in a smoke plume [*Trentmann et al.*, 2003b].

ATHAM is formulated with a modular structure that allows the inclusion of

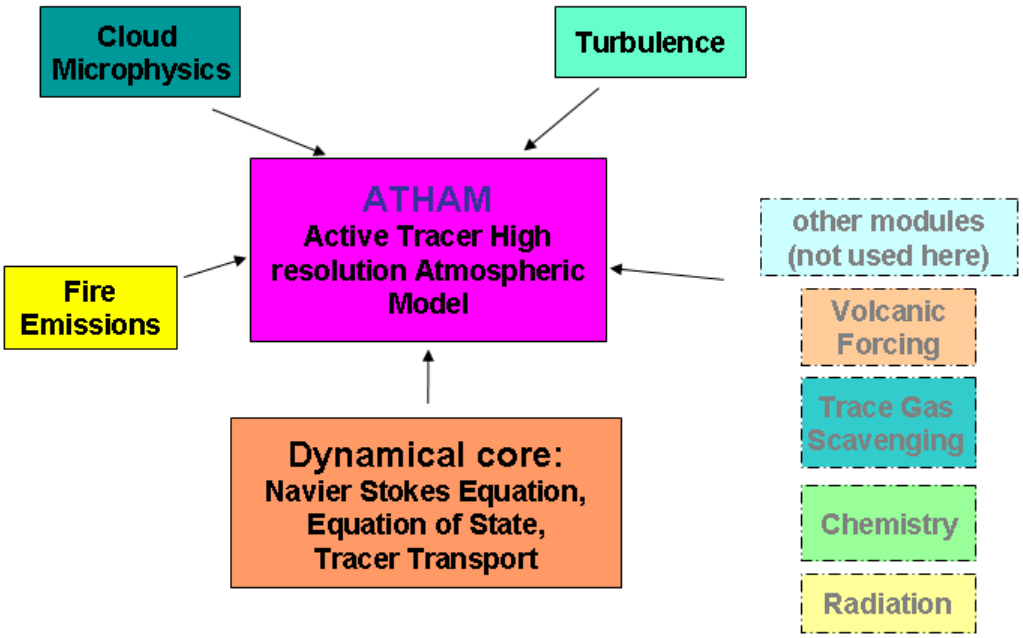

Figure 3.1: Schematic structure of ATHAM. In the version used for this study, the ATHAM core was coupled with a module for the simulation of fire emissions, a two-moment cloud microphysics scheme, and a turbulence module based on an extended TKE approach.

independent modules (Figure 3.1). Existing modules treat the dynamics, turbulence, tracer transport, cloud microphysics, gas scavenging, radiation, emissions, and chemistry. For the study presented here, only the dynamics, transport, turbulence, and cloud microphysics modules of ATHAM were used.

The dynamical core of ATHAM fully accounts for the effect of active tracers, i.e., components that affect the density, heat capacity and compressibility of air parcels. Within the model framework, active tracers can occur in any concentrations. They modify the density and heat capacity of the grid box average quantities, and can have a strong impact on the dynamics of the system. In the present study, the aerosol particles and all hydrometeor classes are treated as active tracers. The model dynamics is based on the simultaneous solution of a coupled equation system comprised of the Navier-Stokes equation, the equations for tracer advection, the temperature equation, and the pressure equation. The spatial discretization of the physical quantities is realized on a staggered Arakawa C grid [*Arakawa and Lamb*, 1977]. In this configuration, the grid points for vectorial quantities such as the wind field are located in between the grid points for scalar

quantities such as pressure, density and temperature. A grid stretching allows for the use of a higher spatial resolution in certain predefined regions at which strongest gradients occur, such as the region close to the fire and the tropopause region.

Centered differences and an implicit time stepping scheme are employed for the numerical solution of the dynamical equations. In order to ensure mass-conservation, the transport equations are formulated in flux form for all tracers.

For the representation of subgrid processes, a modified turbulent kinetic energy (TKE) scheme is used [*Herzog et al.*, 2003]. In this approach, a distinction is made between horizontal and vertical turbulence exchange processes. It is based on a set of three coupled prognostic equations turbulent kinetic energy and the turbulent length scale, from which the horizontal and vertical turbulent exchange coefficients are derived.

Cloud microphysical processes are simulated using a two-moment scheme that predicts the numbers and mass mixing ratios of four classes of hydrometeors (cloud water, cloud ice, rain, graupel) and water vapor [*Textor et al.*, 2003, 2006a]. The size distribution of each mode is represented by a generalized gamma function. In total 13 processes that transfer water between the five classes (four classes of hydrometeors and water vapor) are included in the scheme. These include water vapor transfer processes (i.e., condensation at and evaporation of liquid droplets as well as deposition at and sublimation on ice particles) based on the approach by *Byers* [1965], autoconversion of cloud water/cloud ice into the rain/graupel class, respectively, based on the approach by *Murakami* [1990], accretion due to a differential fall velocity between different hydrometeor classes [*Textor et al.*, 2006a], and freezing of supercooled water following the stochastic approach of *Bigg* [1953]. Within this approach, which is commonly used in microphysical parameterizations in convective cloud models [e.g. *Reisin et al.*, 1996; *Seifert and Beheng*, 2006], the potential of the smoke particles to act as ice nuclei (IN) is not explicitly taken into account. Observations suggest that smoke particles can act as IN [*Hobbs and Locatelli*, 1969], but large uncertainties remain. Therefore the stochastic hypothesis for freezing of droplets seems appropriate for the present study. At temperatures below $-36\,^{\circ}\mathrm{C}$, homogeneous freezing is considered in the model simulations [*Pruppacher and Klett*, 1997].

The activation of aerosol particles cannot be treated explicitly in parameterized microphysical schemes. Sensitivity studies were conducted using a cloud parcel model with explicit treatment of aerosol activation [*Simmel and Wurzler*, 2006]. The influence of the aerosol number concentration, the aerosol size distribution, the vertical velocity, and the soluble fraction of the aerosol on the fraction of activated

aerosol particles has been investigated by M. Simmel (pers. comm., 2003). In these model simulations, the number of activated smoke particles, i.e., the number of aerosol particles that act as cloud condensation nuclei, was most sensitive to the aerosol number concentration. For the high number concentration typically found in pyro-convection ($>100\,000\,\mathrm{cm}^{-3}$), only a very small fraction of the aerosol particles becomes activated. Based on the cloud-parcel model results, we assume in ATHAM that 5% of the smoke aerosol particles act as CCN. The exact value of the activated aerosol fraction used here for the conditions in pyro-convection must be regarded as a rough estimate. However, it was found that the microphysically induced effect of the fire aerosols on dynamics is rather small [*Luderer et al.*, 2006, and Chapter 5]. This justifies the simplified approach used here. However, the simplification limits the use of ATHAM for detailed microphysical studies on the aerosol effect on the evolution and the precipitation efficiency of pyro-convection. Work is in progress to implement a more complex cloud microphysical scheme that includes the activation of aerosol [*Khain et al.*, 2004].

The focus of this study is the detailed description of the impact of fire emissions on the atmosphere in the vicinity of the fire on a horizontal scale of about 100 km. The fluxes from the fire to the atmosphere are prescribed, and therefore not modified by the meteorological conditions, e.g., the wind speed and direction. The reduced requirements for computer resources allow a detailed description of the atmospheric processes related to fire-induced convection. Other numerical models that include the interaction between the atmosphere and fire result in a more realistic fire evolution and small scale features of the atmospheric fields [*Clark et al.*, 2004; *Linn et al.*, 2005]. However, they do not consider all relevant processes (e.g., cloud microphysics) to describe the evolution of deep pyro-convection on the timescale considered here.

3.2.2 Model setup and initialization

For the present study, ATHAM is initialized to realistically represent the conditions of the convective event induced by the Chisholm fire.

The model domain was set to 85 km×65 km×26 km with 110×85×100 grid boxes in the x-, y-, and z-directions, respectively. The minimum horizontal grid box size was set to 500 m and 100 m in the x- and y-directions, respectively. Due to the stretched grid, the size of the grid boxes increases towards the borders of the model domain. The vertical grid spacing at the surface and the tropopause was set to 50 m and 150 m, respectively. Outside these regions, slightly larger vertical grid spacings were used. The lowest vertical model level is located at 766 m above sea level (asl), corresponding to the lowest elevation available in the radiosonde

data used for the model initialization, and close to the elevation of Chisholm of about 600 m [*ASRD*, 2001]. Throughout this study, model elevations are given in m asl. An adaptive dynamical timestep between 1 sec and 3 sec was used, determined online by the Courant-Friedrichs-Lewy (CFL) criterion (CFL$\leq$0.8). The model simulation was conducted for 40 min. Since flat topography is employed in the model simulations, the model spin-up time is substantially shorter than the simulation time.

The model domain was initialized horizontally homogeneously with measurements obtained from the radiosonde presented in Section 2.3, Figure 2.4. Open lateral boundaries were used for the model simulations. The horizontal means of the directional wind speed (u, v) and of the specific humidity (q_v) were nudged towards the initial profile at the lateral boundaries. The initial atmospheric profile has some potential for convection (see Section 2.3), however, without the heat flux from the fire the model would not produce such a deep convective cloud, given a level of neutral buoyancy of 7.4 km in the initial profile.

3.2.3 Representation of the fire emissions

The fire is represented in the model by time-constant fluxes of sensible heat, water vapor, and aerosol mass into the lowest vertical model layer. The fire front was approximately linear and extended from south-south-east to north-north-west at an angle of approximately 165° to North. Note that the x-axis of the model coordinate frame was aligned with the fire front, such that the x-direction of the model domain points to SSE at an angle of 165° to North.

The actual length of the fire front was about 25 km. Due to computational constraints, however, we only accounted for the southern 15 km of the fire front, which passed through densely forested area. The width of the fire front was set to 500 m. The energy release from the fire was calculated based on a fuel loading of 9.0 kg m^{-2} and a value of 18 700 kJ kg^{-1} for the heat of combustion. Based on the relatively high fuel load in the southern part of the fire front, we choose a higher-than-average fuel loading in the simulations. With the observed rate of spread of the fire front of 1.5 m s^{-1}, the frontal intensity [*Byram*, 1959; *Lavoué et al.*, 2000] of the simulated fire is about 239 000 kW m^{-1}. In the model, the fire fluxes are held constant throughout the simulation. Not enough information on the fire behavior is available to include a more realistic spatial and temporal distribution of the fire emissions. As part of this study, test simulations using a moving fire front have been conducted (not shown here), which showed no impact of the moving fire front on the model results.

There is significant uncertainty in the literature on how much of the energy re-

leased by combustion, contributes to local heating of the atmosphere (sensible heat flux) and is available for convection, and how much of the energy is lost due to radiative processes. Commonly found estimates for the radiative energy are between nearly zero percent [*Wooster*, 2002; *Wooster et al.*, 2005] and 50% [*McCarter and Broido*, 1965; *Packham*, 1969]. These estimates are based on laboratory studies or small scale fires and their application to large scale crown fires resulting in pyroCb convection remains highly uncertain. Additional uncertainty exists related to the fate of the radiative energy emitted by the fire. In the thermal infrared, where most of the fire radiation is emitted [*Wooster*, 2002], aerosols are rather inefficient absorbers. It is likely that most of the radiative energy from the fire is absorbed by cloud droplets or gaseous absorption at cloud base or in air masses that are entrained into the convection. In both cases the radiative energy from the fire is trapped in the lower part of the pyro-convection and therefore contributes to the convective energy. Considering these radiative processes in detail is not possible in the present model setup. Here, we assume that all energy released in the combustion process becomes available for convection. This assumption is consistent with the coupled fire-atmosphere model of *Clark et al.* [1996]. The sensitivity of the pyroCb characteristics to assumptions on the release of sensible heat is studied in Chapter 5.4.2.

A small part of the energy released by the combustion of fuel is used to evaporate the fuel moisture. In the present study, a fuel moisture content of 40% was assumed (cf. Chapter 2.2), which takes up about 5% of the total energy released by the combustion. Additional water vapor is released directly from the combustion process itself. Assuming complete combustion, 1 kg of fuel yields about 0.5 kg of combustion water vapor [*Byram*, 1959]. In our simulations, about $8\,\mathrm{kg\,m^{-2}}$ water vapor was released, with the main contribution (about 55%) coming from combustion moisture, leading to a total release of 4.7×10^8 kg H_2O. The particulate emissions from the fire were calculated using the emission factor of $17.6\,\mathrm{g\,kg^{-1}}$ from *Andreae and Merlet* [2001], assuming a volume mean diameter of 300 nm [*Reid et al.*, 2005].

No detailed information on the wind direction at the location of the fire front at the time of the blow-up is available. Due to the complex meteorological situation (i.e., the approaching line of convection) it is likely that the local wind speed and wind direction were irregular and subject to rapid change. These effects cannot be represented with the model approach of this study. Therefore, we adopted the wind profile measured by the Edmonton radiosonde. Its surface wind direction is at an angle of about 30° to the fire front. In the upper atmospheric levels, the ambient wind direction is parallel to the fire front. The angle between the surface

wind field and the fire front has some impact on the vertical dynamics of the pyro-convection since. Small angles between the fire front and the wind direction result in longer exposure of individual air parcels to the fire heating and hence to higher buoyancy and more intense vertical development.

3.3 Model limitations and uncertainties

It is necessary to keep in mind that model simulations have inherent limitations. Since there is no analytical solution to the dynamical equations the model is based on, it is necessary to seek an approximate numerical solution by discretizing the model domain and using finite time steps. The resolution of the model grid is limited by constraints to the computational resources. The minimum grid spacing used for the ATHAM simulation is similar to the size of characteristic structure such as the fire front. As part of this work, sensitivity experiments with different model setups were conducted (not shown). These experiments showed that a further increase in resolution does not have a significant influence on the model results.

Models only include a limited number of processes and are not able to capture the full complexity of the real world. Many processes, such as microphysics and subgrid-scale turbulence in the case of cloud resolving models, cannot be simulated directly. For such processes, models such as ATHAM have to rely on parameterizations as described in Section 3.2.1. The two-moment scheme used here for the simulation of cloud microphysical processes, for instance, performs well in simulating the transformations between water vapor and the various hydrometeor classes. Due to the prescribed width of the size distribution, however, it is limited in its ability to simulate the growth to precipitation sized hydrometeors. This limitation must be taken into account in the analysis of the simulated cloud properties.

The validity of simulations also depends critically on the accuracy of initial and boundary conditions. The uncertainties for the present study are largely dominated by the uncertainty in the input parameters. Since the most active phase of fire convection happened during the passage of a cold front, the meteorological conditions were highly variable at that time and are difficult to constrain in retrospective. Compared to other fire events, the knowledge about the fire characteristics such as the amount of fuel burned and rate of spread are rather good. Nevertheless, large uncertainties remain. The amount of fuel burned was based on the sampling two weeks after the fire. The rate of spread, an important quantity determining the fire intensity, is based on a fire model, which may have underestimated the fire dynamics present in the extreme conditions of the Chisholm

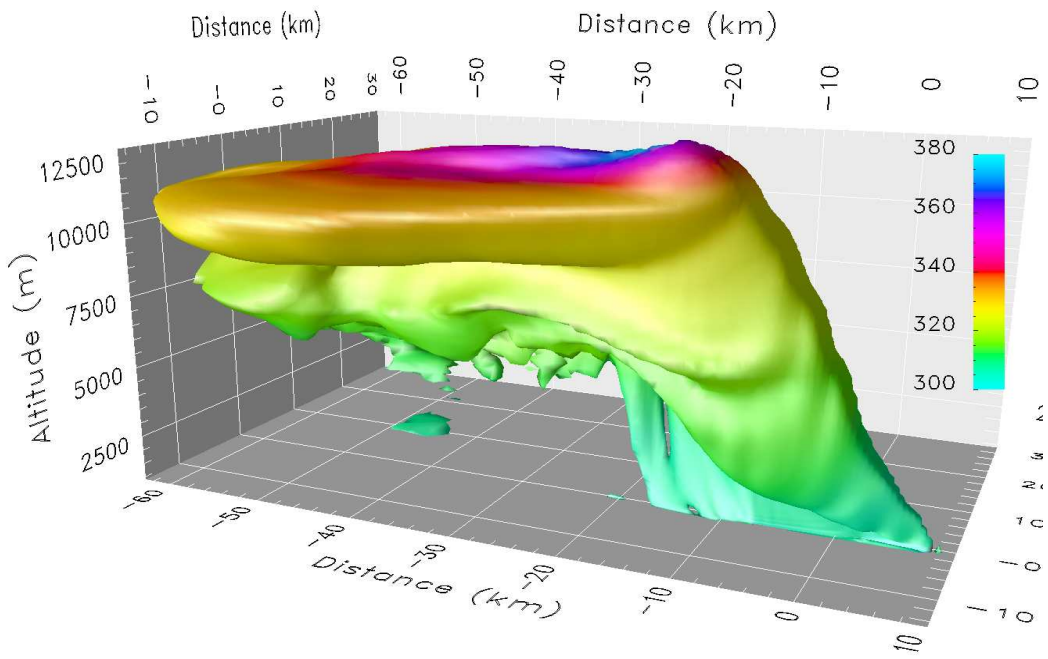

Figure 3.2: Spatial distribution of the $50\,\mu g\,m^{-3}$-isosurface of the simulated aerosol mass distribution after 40 min of simulation time. The color coding represents potential temperature.

fire.

It is important to critically assess the model results in view of the limitations and uncertainties. The sensitivity studies presented in Chapter 5 allow us to analyze how strongly the results depend on certain input parameters. Furthermore, comparisons of the model results with observations as provided in Chapters 3.4 and 4 are used to evaluate the model performance.

3.4 Model results

This section presents results from the model simulations. The overall structure of the simulated pyroCb is described, followed by a more detailed investigation of some dynamical features in Section 3.4.3.

3.4.1 General aspects

A three-dimensional representation of the aerosol plume simulated with ATHAM for an integration time of 40 min is depicted in Figure 3.2. The plume is represented by the $50\,\mu g\,m^{-3}$-isosurface of the aerosol concentration with the potential temperature field overlaid in color coding. The assumed linear shape of the fire

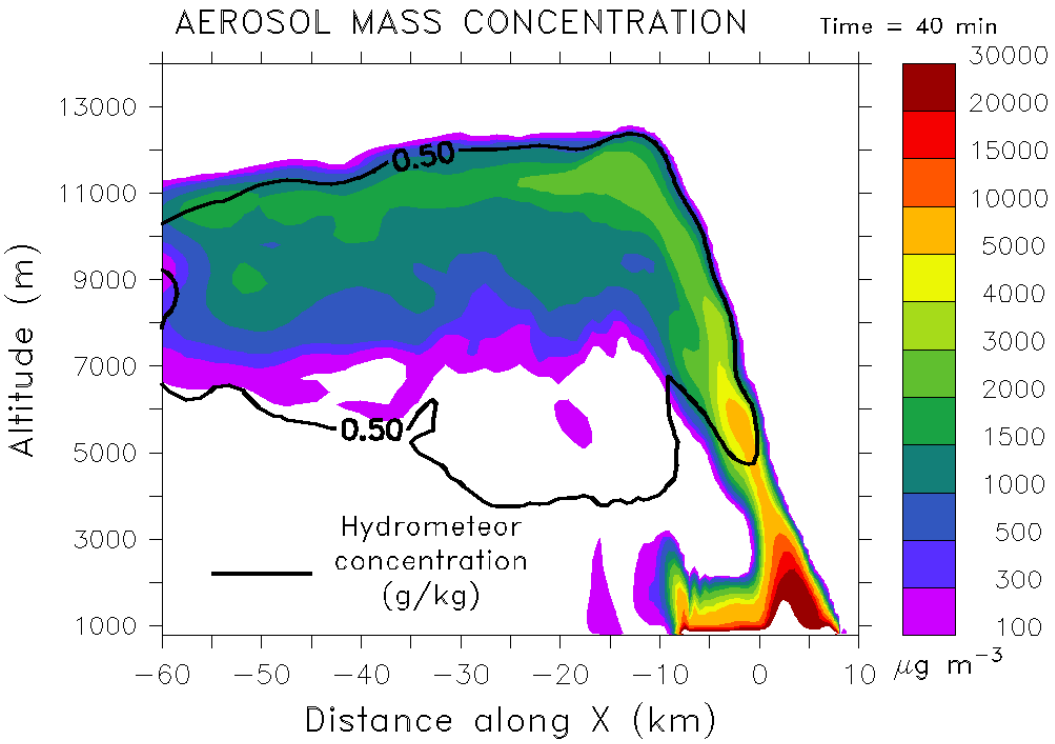

Figure 3.3: Vertical cross section of the aerosol mass distribution at along the x-axis at y=0 km. The black solid line is the 0.5 $g\,kg^{-1}$ isoline of the hydrometeor concentration and indicates the extent of the pyroCb.

front is clearly visible as the origin of the convection and the source of the aerosol particles. Above the updraft region, the an overshooting dome is formed at which the aerosol plume reaches its maximum height of about 12.5 km. The cloud top altitude is roughly 1 km lower than the estimate obtained from the observations (cf. Chapter 2), indicating that either the fire-forcing was underestimated or that the meteorological profile underestimates the convectivity of the background atmosphere. Nonetheless, the overall structure and shape of the simulated pyro-cloud is in good agreement with the observations. Large areas of the cloud top are characterized by potential temperatures in excess of 340 K, indicating that the plume reaches well into the stratosphere. The dynamical tropopause was located at 332 K, corresponding to an altitude of 11.2 km (cf. Chapter 2.3). Downwind of the overshooting region, a relatively warm area develops in the anvil region with potential temperatures above 350 K. This is in good agreement with the warm core of the Chisholm pyroCb observed by satellite [*Fromm and Servranckx*, 2003; *Rosenfeld et al.*, 2007]. A more detailed investigation of the plume top structures including an evaluation of the model results with satellite observations is presented in *Luderer et al.* [2007b] and Chapter 4.

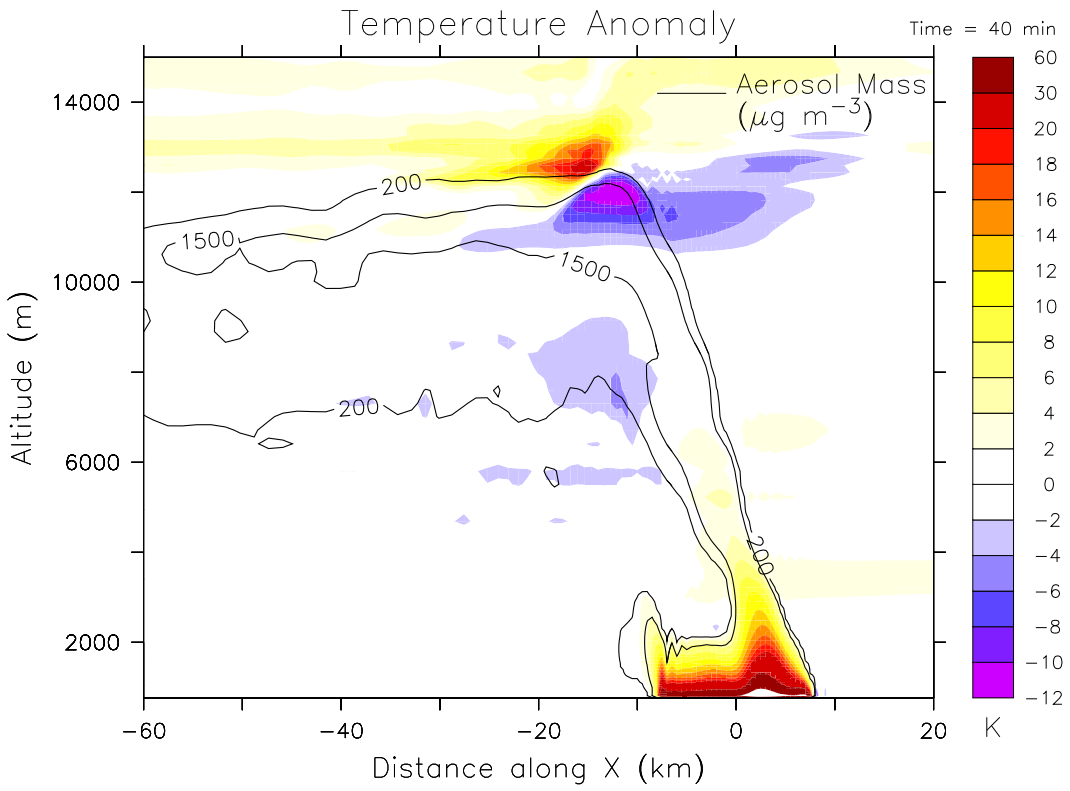

Figure 3.4: Simulated temperature anomaly after 40 min along the cross section at y=0. Shown is the difference between the simulated and the initialized ambient temperature. Negative (positive) temperature anomalies are shown in blue (red).

Figure 3.3 presents a vertical cross section along the fire front of the aerosol mass concentration. The lower part of the smoke column is characterized by very large aerosol concentrations. At the cloud base the aerosol mass concentration is still as high as 5000 $\mu g\,m^{-3}$, corresponding to extreme number concentrations on the order of 10^6 cm^{-3}. Within the pyroCb, the smoke aerosol becomes increasingly diluted but nonetheless remains high with peak concentrations of about 2000 $\mu g\,m^{-3}$ in the upper part of the anvil.

Figure 3.4 shows the simulated temperature anomaly after 40 min along the same cross section used for Figure 3.3. The fire-released heat flux induces a strong temperature anomaly in the lower 2 km of the rising plume with maximum values of some 50 K in the layer above the fire. About 1 km above the fire, the temperature anomaly has decreased to values smaller than 20 K, at about 3 km it is only about 8 K. In the upper part of the plume, a dipole-like structure of the temperature anomaly can be seen. This is associated with gravity wave formation above the overshooting dome. A detailed analysis of this phenomenon is presented in Chapter 4.

For photochemical reactions occurring in the smoke plume, this temperature enhancement can be regarded as small and can be neglected in photochemical models of young biomass burning plumes [*Mason et al.*, 2001; *Trentmann et al.*, 2005]. The temperature effect from the fire is, however, significant for the condensation of water vapor and the cloud base level (see Chapter 3.4.2). The increased temperature leads to a delayed onset of condensation and a higher cloud base, thereby counteracting the effect of the water vapor emissions from the fire on the cloud base (cf. also Chapter 6).

A cross section of the vertical velocity along the y-axis after 40 min is provided in Figure 3.5. The maximum vertical velocity is reached right above the fire, below the 2000 m level. At the tropopause, a region with downward vertical motion of about $6\,\mathrm{m\,s^{-1}}$ is simulated downwind of the fire. One has to note, that the interpretation of individual cross sections is complex, especially due to the asymmetric ambient flow.

In contrast to simulations of mid-latitude convection, the maximum vertical velocity is reached at lower levels in the case of fire-induced convection (between 1 km and 3 km compared to about 9 km in *Wang*, 2003 and *Mullendore et al.*, 2005). This is explained by the significant acceleration by the heat flux from the fire. A second local maximum of the updraft velocity can be found at about 8 km (Figure 3.5), which corresponds to the maximum of the updraft velocity in simulations of regular mid-latitude convection due to the release of latent heat. The different vertical profiles in the updraft velocity, in particular at the cloud base, between regular mid-latitude convection and fire-induced convection potentially lead to differences in the cloud microphysical evolution in addition to the high number of smoke particles acting as CCN.

After the onset of the heat flux from the fire, convection immediately develops in the model simulations due to the positive temperature anomaly of the air in the lowest model layer above the fire. Figure 3.6 presents streamlines of the horizontal wind and the vertical wind velocity at 1000 m asl (i.e., about 200 m above ground level.) after 40 min of simulation. The fire clearly has a strong impact on the ambient wind field. The emission of sensible heat leads to high updraft velocities of up to $20\,\mathrm{m\,s^{-1}}$. The updraft results in the formation of a convergence of the horizontal wind. The simulated updraft velocities at the surface are signifcantly higher than those expected for regular convection. In the case of pyro-convection, the updraft initiates the convergence of the low-level horizontal wind, while regular convection often starts from low level wind convergence.

This wind modification is expected to significantly impact the evolution of the fire itself as has been shown in coupled atmosphere-fire simulations [*Clark et al.*,

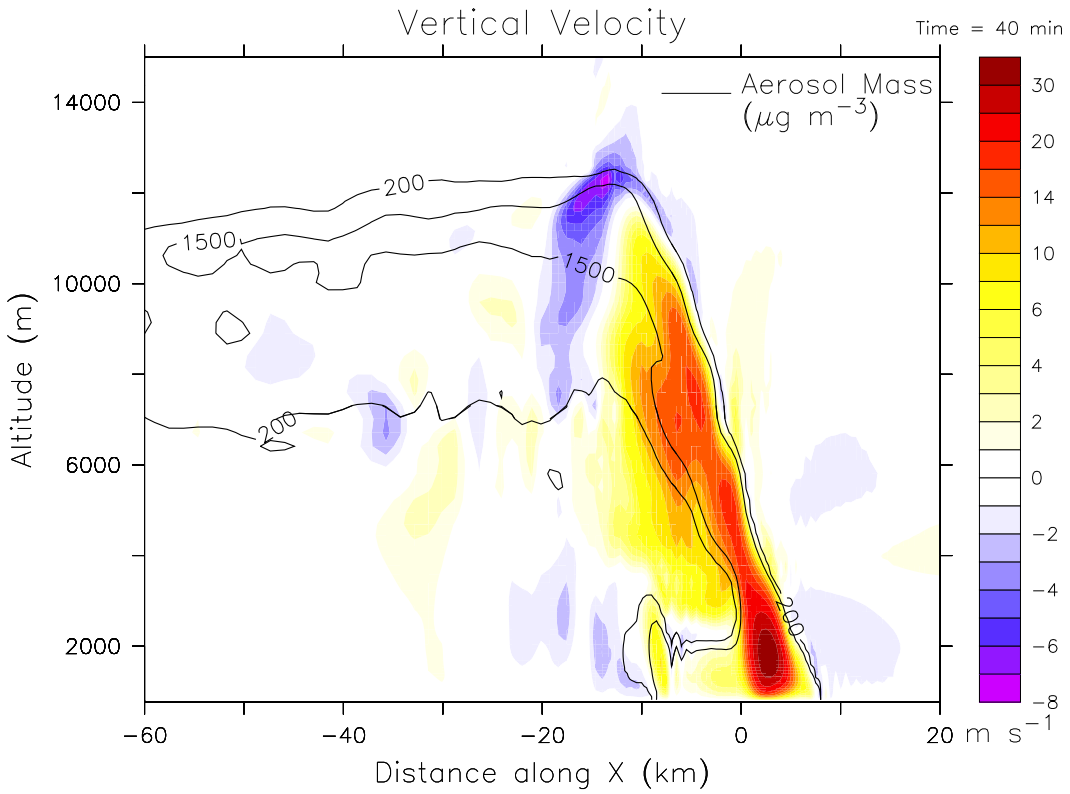

Figure 3.5: Simulated updraft velocity (color coding) and aerosol mass concentration (contour lines) after 40 min along the cross section at y=0.

2004; *Coen*, 2005]. Since the focus of this work is the investigation of the vertical transport of fire emissions, this feedback mechanism is not included here and the shape of the fire and the fire emissions are kept constant throughout the simulation.

For the analysis of vertical transport into the UT/LS region, it is worthwhile to consider the horizontally integrated aerosol mass distribution, both as a function of altitude and as a function of potential temperature (cf. also Chapter 4). Figure 4.10 shows the horizontally integrated aerosol mass as a function of altitude and potential temperature for various integration times. The main outflow height (defined as the height of the maximum of the vertically integrated aerosol distribution) and the maximum penetration height (defined as the height below which 99 % of the aerosol mass is located) are 10.6 km and 12.1 km, respectively (cf. Chapter 5 and *Luderer et al.*, 2006). The outflow height is substantially higher than the level of neutral buoyancy calculated based on the sounding (7410 m, Section 2.3), due to the significant emissions of sensible heat from the fire. A substantial amount of aerosol mass is located at stratospheric potential temperature levels (θ>332 K). After 50 min of simulation time, an aerosol mass of 1050 t is located above the tropopause. This amount corresponds to 11% of the total aerosol mass emitted by

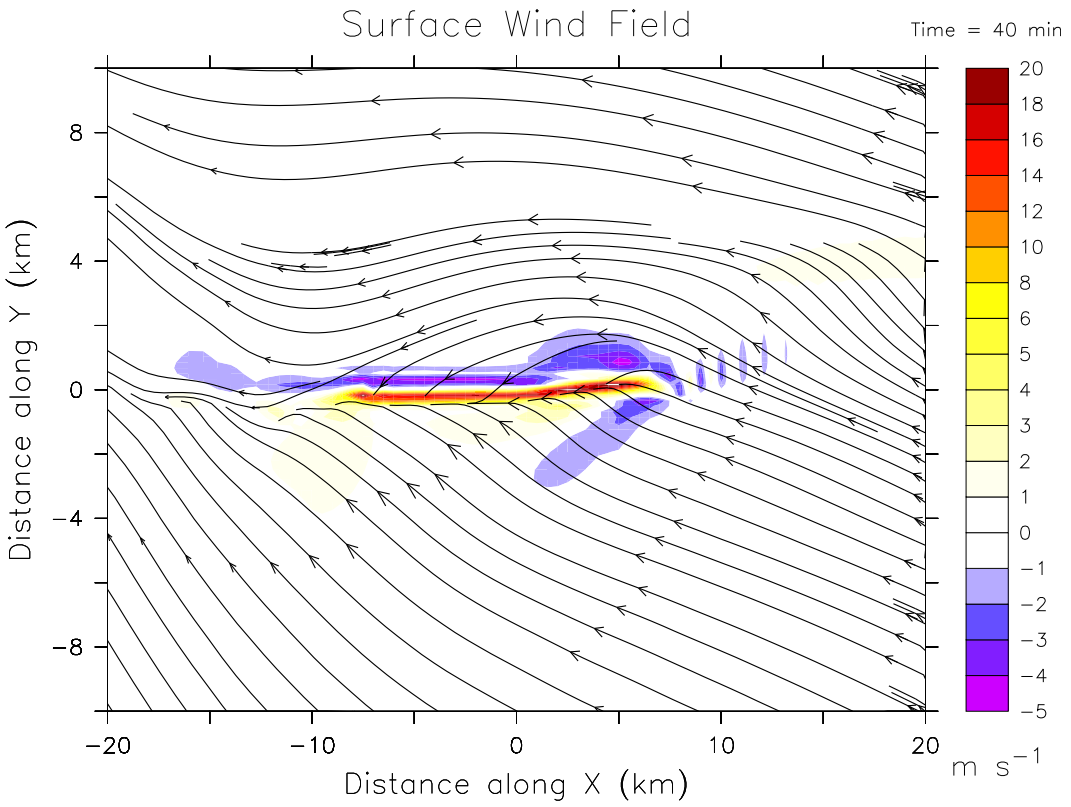

Figure 3.6: Simulated wind field after 40 min of simulation time at 1000 m altitude. Streamlines indicate the horizontal wind, the vertical wind speed is indicated by the color coding. Adopted from *Trentmann et al.* [2006].

the fire during this time span. The real-world Chisholm pyroCb persisted for much longer time, and the area burned during its occurrence was about 5 times larger than what is accounted for in the model. This is consistent with estimates from satellite observations of the aerosol plume in the aftermath of the Chisholm pyroCb, from which a stratospheric injection of roughly 10 000 t of aerosol or 10-20% of the total aerosol emitted were estimated (Mike Fromm, personal communication, 2007). The total stratospheric sulphur injection caused by the volcanic eruption of Mount Pinatubo was about 10 Tg [*Bluth et al.*, 1992], about three orders of magnitude more than the aerosol mass injected by the Chisholm fire.

Whether the smoke aerosol will remain in the stratosphere after the pyro-convection has decreased, can not be evaluated with the present model setup that only allows model simulations for 50 min. The present simulation, however, does show that pyro-convection can be sufficiently intense to transport smoke aerosol across the tropopause and into the stratosphere.

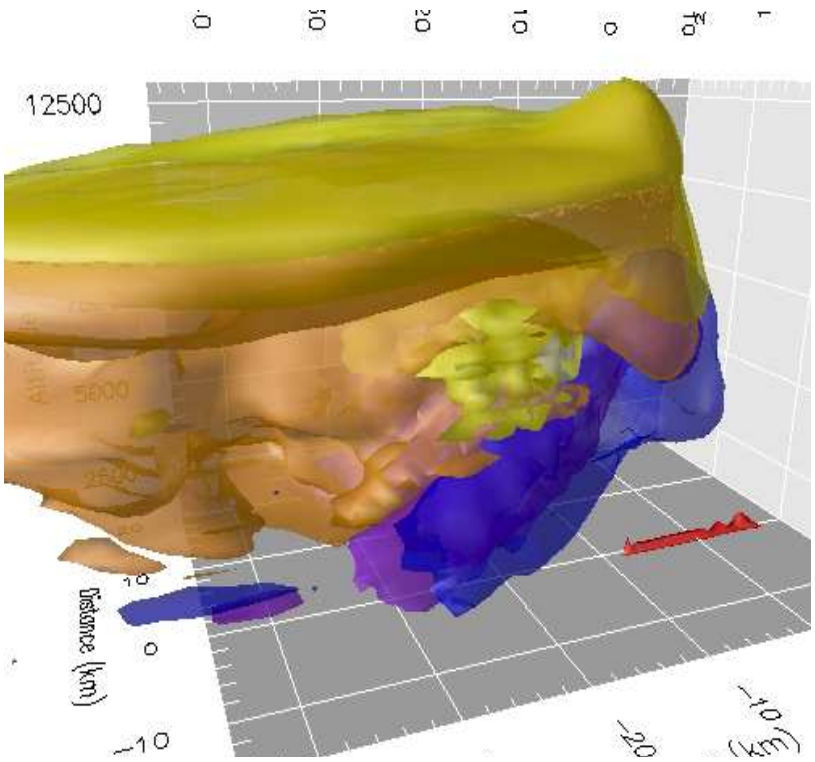

Figure 3.7: Spatial distribution of the $0.4\,\mathrm{g\,kg^{-1}}$-isosurfaces of the simulated (blue) cloud water, (purple) rain water, (yellow) cloud ice, and (orange) graupel after 40 min of simulation time. Also indicated is the fire front (red) by the $45\,000\,\mu\mathrm{g\,m^{-3}}$-isosurface of the simulated aerosol mass distribution. Adopted from *Trentmann et al.* [2006].

3.4.2 Microphysics

An analysis of the microphysical structure of the pyroCb is shown in Figure 3.7, where the spatial distribution of the $0.4\,\mathrm{g\,kg^{-1}}$-isosurfaces of the four hydrometeor classes treated in the model (cloud water, rain, cloud ice, and graupel) after an integration time of 40 min is presented. Graupel is the main contributor to the hydrometeor mass in the simulated pyroCb. It should be noted that the upper part of the cloud is dominated by cloud ice particles. This is due to the sedimentation of the large hydrometeors, leaving behind the small hydrometeors.

The droplet size in the updraft region is of key importance for the microphysical development of convective clouds. Cross sections of volume mean radii of the various hydrometeor classes are depicted in Figure 3.8. The hydrometeors remain very small at volume mean radii of about $3\,\mu$m throughout the updraft region due to the high concentration of smoke aerosol acting as CCN and the large updraft velocities [*Luderer et al.*, 2006, and Chapter 5]. In good agreement with the observations, small liquid cloud droplets are present in the smoke plume's updraft region up to the level of homogeneous freezing of $-39°$C at about 9000 m. Such

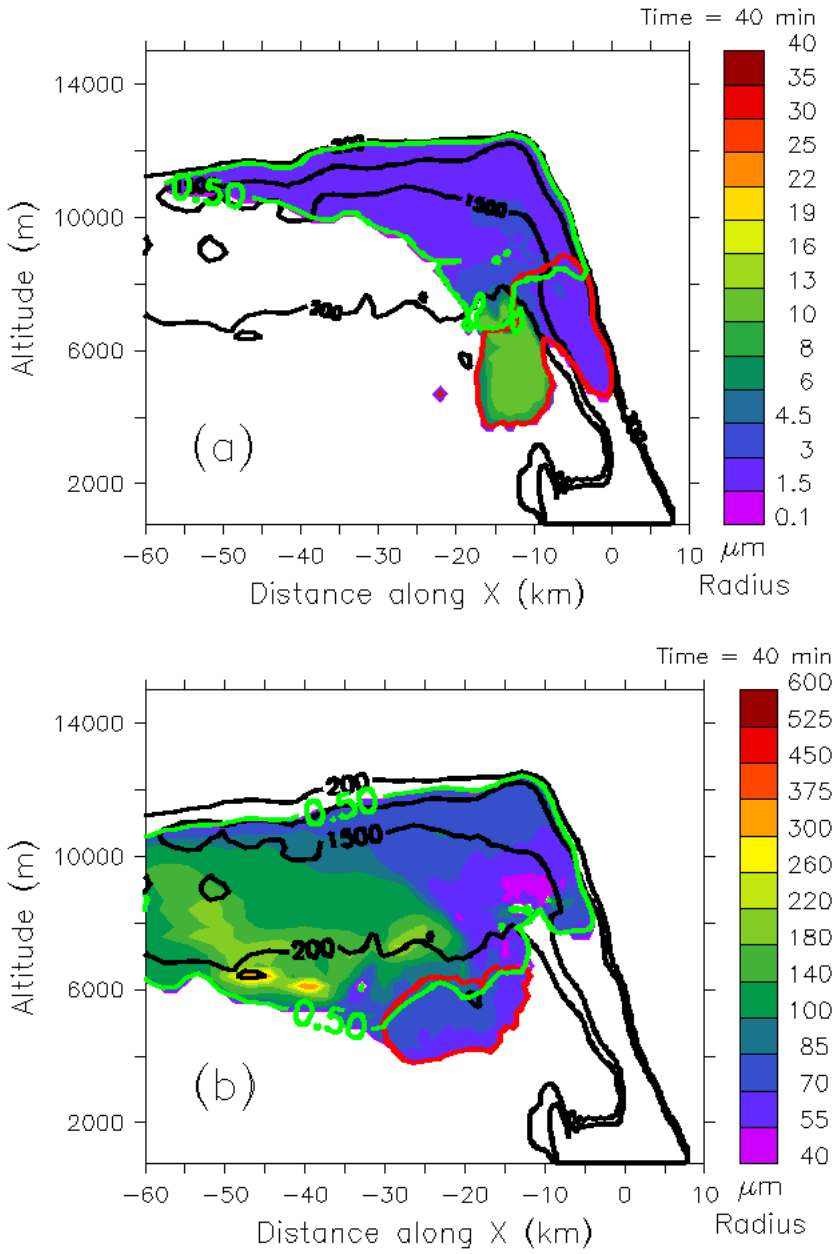

Figure 3.8: (a) Volume mean radii of the small hydrometeor classes (cloud droplets, ice crystals) and (b) the large hydrometeor classes (rain, graupel). The black lines are isolines of the aerosol mass concentration in $\mu g\,m^{-3}$. The abundance of liquid hydrometeors is indicated by the 0.5 $g\,kg^{-1}$-isoline in red, that of frozen hydrometeors by 0.5 $g\,kg^{-1}$-isoline in green.

homogeneous freezing of the small cloud droplets gives rise to large amounts of small ice crystals in the upper part of the anvil.

The pyro-convection also induces the uplift of relatively clean, i.e., smoke free

air, about 10 km downwind of the smoke column, which results in the formation of a secondary cloud. Figure 3.8(a) shows that this secondary cloud is characterized by distinctly different microphysical properties, with cloud droplet radii of about 10 μm. Due to the droplet sizes, freezing sets in, at circa 1500 m lower altitude level.

Within the smoke column, the first cloud water condenses after about 4 min of simulation time at an elevation of about 4.2 km. The fire-induced temperature enhancement temperature results in delayed condensation compared to the LCL of the background profile, which is located at 3.25 km.

No large liquid hydrometeor are formed in the updraft region of the smoky part of the convective cloud. Significant amounts of hydrometeors large enough to sediment are only found downwind of the updraft region. Precipitation is very weak, and only little amounts of rain reach the ground.

After 40 min, the total amount of hydrometeor mass in the model domain is 9.6×10^9 kg. The hydrometeor mass is dominated by graupel, which accounts for 6.2×10^9 kg. Also, ice crystals which accumulate in the upper part of the anvil, contribute significantly with 2.0×10^9 kg to the hydrometeor budget, while the liquid hydrometeor classes only account for a combined 1.4×10^9 kg.

3.4.3 Convection dynamics

The concept of convective available potential energy (CAPE) considers the energy that a pseudo-adiabatically ascending air parcel can draw from its buoyancy relative to the environment between the level of free convection and the level of neutral buoyancy in a conditionally unstable environment [e.g., *Glickmann*, 2000]. Real-world pyro-convection differs from this idealized concept mainly in two aspects: Firstly, due to the input of latent heat and sensible heat from the fire, air parcels already become positively buoyant at ground level and therefore do not need to overcome the convective inhibition typical of regular convection in conditionally unstable environments. The energy input from the fire adds significantly to the convective energy of pyro-convection. Secondly, substantial amounts of ambient air are entrained into the pyro-convection at low- and mid-levels. This effect is in disagreement with the assumption of pseudo-adiabatic process and tends to decrease the air parcels' buoyancy. The convective energy is more realistically described by introducing a new quantity, which hereafter will be referred to as integrated buoyancy IB:

$$IB = \int_{Z_0}^{Z_{\mathrm{LNB}}} \bar{b}(z)\,\mathrm{d}z. \tag{3.1}$$

.

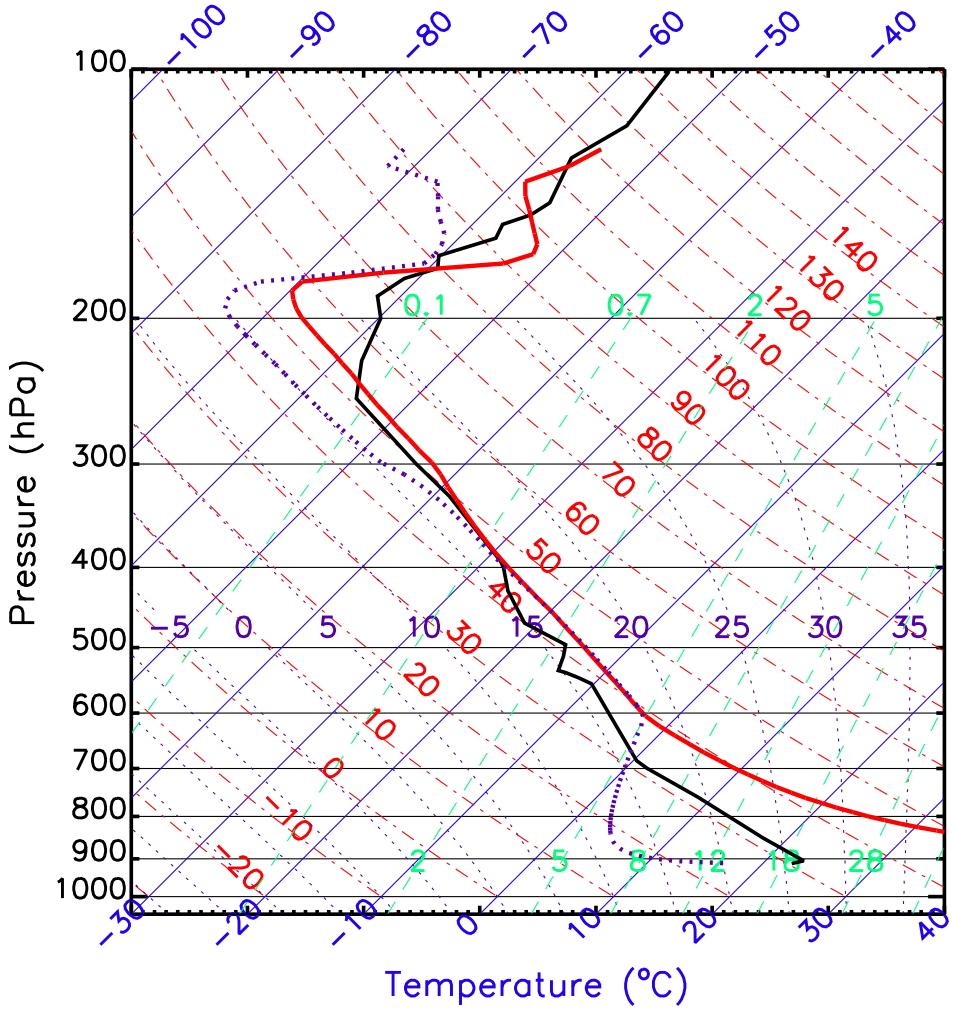

Figure 3.9: Vertical profiles of background temperature (solid black line) as well as mean temperature (red solid line) and dew point temperature (purple dotted line) within the updraft region of the aerosol plume.

IB generalizes the CAPE concept and expresses the amount of energy an air parcel would gain from the acceleration due to its positive buoyancy during its ascent from the ground or the LFC to its LNB.

The dynamics of pyro-convection can be visualized by comparing the ambient temperature profiles with the mean temperature profile within the updraft region of the smoke plume. Figure 3.9 depicts vertical profiles of the environmental temperature, T_0, as well as mean temperature, $\overline{T}$, and dew point temperature, $\overline{T_d}$, within the updraft region. The mean values within the updraft region were calculated based on the framework introduced in Chapter 5.4.1, Equation (5.2). The buoyancy of an ascending air parcel is roughly proportional to the temper-

ature difference to the environment. The heating from the fire results in a large temperature excess of up to 60°C of the smoke column at low levels. Below the lifting condensation level, indicated by the convergence of the $\overline{T}$- and $\overline{T_d}$-profiles, at about 600 hPa, the absolute value of the temperature gradient is significantly larger than that of the dry adiabat. This additional cooling is due to entrainment of environmental air into the smoke column.

While the temperature difference at the cloud base is about 2°C, it becomes close to zero between 400 hPa and 320 hPa. In this altitude range, glaciation has already set in for ambient convection, whereas, due to its extremely continental microphysical structure, the pyroCb is characterized by supercooled liquid cloud water up until the level of homogeneous freezing, which is reached at 320 hPa. The implications of this effect for the interaction between microphysics and convection dynamics are discussed in Chapter 5.4.4.

Above the freezing level, pyroCb air is slightly warmer than the environment. The level of neutral buoyancy is reached at the 240 hPa level, above which the ambient profile is characterized by the transition into the tropopause inversion. In the overshoot region above the LNB, the pyroCb air is up to 10°C colder than the environment.

3.4.4 Entrainment and redistribution of air masses

Entrainment of ambient air into the pyroCb is of major relevance for the cloud's budgets of energy and water vapor. In order to assess mixing at various altitude levels, six tracers were initialized within six separate layers of identical mass, i.e., pressure thickness. The lower boundaries of these layers are the surface, 2.25 km, 4 km, 6.1 km, 8.9 km, and 12.9 km. Cross sections of the redistribution of the tracers after 40 min simulation time are shown in Figure 3.10. Figure 3.11 depicts the relative contribution of the different tracer masses to the air the smoke plume.

The air masses in the main outflow of the plume mainly originate from the two lower levels (Tracer I and Tracer II), each contributing about 30% to the total air mass in the plume. The significant contribution of the mid-level Tracer II indicates significant entrainment of ambient air masses into the plume between 2.25 km and 4 km. Additional contributions to the air in the outflow come from Tracers III, IV, and Tracer V. These findings are consistent with the modeling results from *Mullendore et al.* [2005], who also found significant entrainment of ambient air from the middle troposphere into the updraft and the outflow of convective systems.

The significant contribution of mid-level air masses in the plume point to the potential importance of the background conditions, particularly in terms of temperature and humidity levels in the ambient atmosphere. The sensitivity of the

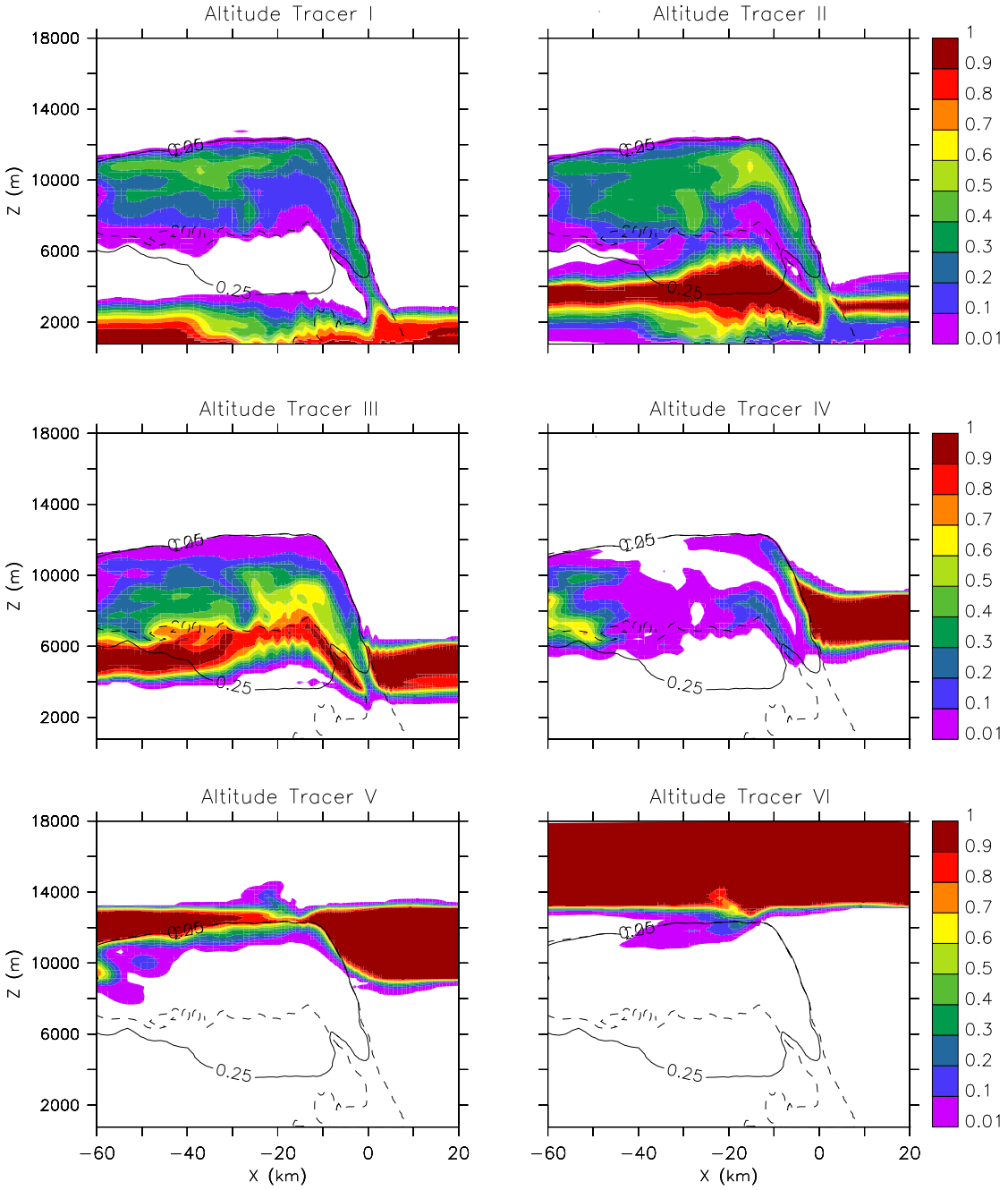

Figure 3.10: Cross-sections of the relative contribution of tracer air masses in the plume from different atmospheric levels. Altitude tracer I was initialized between the surface and 2.25 km, tracer II at 2.25 km–4 km, tracer III at 4 km–6.1 km, tracer IV at 6.1 km–8.9 km, tracer V at 8.9 km–12.9 km, tracer VI above 12.9 km. Each tracer layer corresponds to a pressure increment of about 150 hPa, such that the respective air masses are of equal thickness. The solid and dashed lines indicate isolines of hydrometeor content (0.25 g kg^{-1}) respectively.

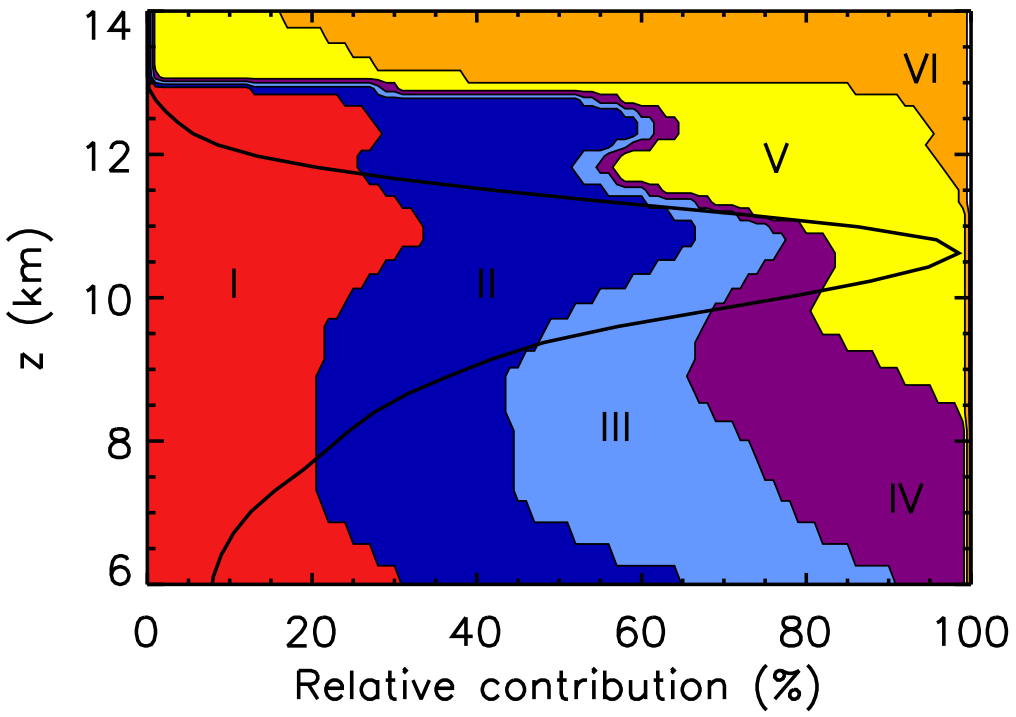

Figure 3.11: Relative contribution of altitude tracers from different atmospheric levels to the air masses to in the smoke plume. Red: Tracer 1, released between the surface and 2.25 km; dark blue: Tracer II, 2.25 km–4 km; light blue: Tracer III, 4 km–6.1 km; purple: Tracer IV, 6.1 km–8.9 km; yellow: Tracer V, 8.9 km–12.9 km; orange: Tracer VI, above 12.9 km. Also indicated is the horizontally integrated aerosol mass (black line).

pyroCb convection to background meteorology is analyzed in a separate set of sensitivity studies presented in Chapter 5.4.5.

The high amounts of entrainment also limit the use of the CAPE concept, which usually neglects entrainment, to characterize pyro-convection events. The non-negligible contributions of tracers V and VI in the smoke plume especially at elevations above 12 km give evidence for the occurrence of mixing processes and downward transport of stratospheric air at the tropopause level.

3.4.5 Budgets of water and energy

A detailed analysis of the contribution of the water vapor emitted by the fire to the total water vapor is given in Chapeter 6. Using passive tracers, the model study allows us to distinguish between water vapor emitted from the fire and moisture entrained from the background atmosphere. Figure 6.3(a) shows the relative contribution of fire-released moisture to the water budget of the pyro-cloud. Right

above the fire, the fire-released water dominates the water vapor concentration in the smoke column. Due to mixing of the plume with environmental air masses, however, the contribution of the water vapor from the fire rapidly decreases at higher altitude. Above about 4000 m, the contribution of water from the fire is less than 10% of the total water available in the plume. The sensitivity study presented in Chapter 5.4.3 and the more detailed analysis provided in Chapter 6 show that the water vapor emitted from the fire does not have a significant impact on the evolution and dynamics of pyro-clouds and atmospheric dynamics.

An estimate of the contribution of latent heat release from condensation and freezing compared to the release of sensible heat by the fire can be obtained by considering the total heat of condensation and freezing based on the total mass of hydrometeors in the model domain. After 40 min of simulation time, the latent heat amounts to be 26.8×10^9 MJ (8.22×10^9 kg frozen hydrometeors, 1.4×10^9 kg liquid hydrometeors). This value should be considered a lower estimate of the total energy release by condensation/freezing, since deposition of hydrometeors is neglected in this simplified estimate. This is much larger than the total amount of sensible heat emitted from the fire during the simulation time, which sums up to 9×10^9 MJ. Thus, only about 25% of the total energy results from direct emission of sensible heat from the fire, while the dominant part of the energy budget can be attributed to the release of latent heat from condensation and freezing. Comparing the total water mass released from the fire (4.7×10^8 kg, see Section 3.2.3) to the total mass of liquid and frozen hydrometeors in the plume (9.62×10^9 kg) yields a contribution of the latent heat release from the fire of less than 5% to the total energy released from condensation and freezing.

A similar estimate can be obtained by considering an individual parcel in the upper part of the plume with an average aerosol mass concentration of 3000 μg m^{-3} and a hydrometeor concentration of about 5 g kg^{-1}. Based on the emission ratios for sensible heat, water vapor, and particles, this parcel gained about 6 K of sensible heat and 0.3 g kg^{-1} H_2O from the fire. The hydrometeor concentration corresponds to a release of latent heat from condensation of about 12 K. This parcel-based estimate yields a slightly larger contribution of the sensible heat flux from the fire to the parcel energy than the previous estimate based on the energy budget for the whole pyroCb. Both estimates highlight the importance of the availability of ambient moisture for the evolution of the pyro-convection.

It must be noted, however, that a positive feedback exists between the sensible heat flux from the fire and the latent heat released in the plume [*Luderer et al.*, 2006, and Chapter 5]. Enhancing the sensible heat flux enhances also the total latent heat release in the plume, probably because of enhanced entrainment of

humid air at low levels and reduced entrainment of dry air at higher levels. Even though the latent heat dominates the overall energy budget of the plume, the sensible heat input is a critical parameter to determine the evolution of the pyro-convection [*Luderer et al.*, 2006, and Chapter 5].

3.5 Summary and conclusions

In this chapter, a three-dimensional model simulation of the pyroCb convection induced by the Chisholm fire in Alberta, May 2001, was presented. During its most intense phase, the Chisholm fire burned 50 000 ha of forested land within a few hours, resulting in the formation of an intense fire-induced cumulonimbus (pyroCb). Using fire emissions based on available estimates for the amount of fuel burned and measurements obtained by a radiosonde at a distance of about 200 km, the model is able to realistically simulate the formation and the evolution of the pyro-convection. The maximum penetration height of the pyro-convection was well above the tropopause and is slightly lower than the maximum altitude determined from radar observations. The injection of smoke aerosol into the stratosphere is simulated in good accordance with satellite observations. The character of the pyro-convection is different from regular mid-latitude convection. Mainly owing to the sensible heat emissions from the fire, the main outflow is significantly higher than the level of neutral buoyancy of the background atmosphere.

More modeling studies of this kind are required to fully understand the nature of pyro-convection. The intensity of pyro-convection determines the injection height of fire emissions, which is important for their atmospheric lifetime and impact. Injection of smoke from fires at high altitude into the atmosphere increases its lifetime compared to injection in the boundary layer and may result in hemispheric and seasonal effects of the smoke from a single pyroCb event on the atmosphere. PyroCb studies of the kind presented here, using different scenarios for the fire emissions and atmospheric conditions, will lead to a more realistic representation of fire emissions in larger scale models. Studies such as the present one also make it possible to take into account the small-scale processes in pyro-clouds that lead to a modification of the primary fire emissions (e.g., photochemistry, scavenging of soluble gases and particles). The investigation of these and other processes (e.g., aerosol-cloud interaction) using a combination of model simulations and field observations will lead to an improved representation of fire emissions in larger scale models and will also advance our understanding of these fundamental processes in regular convective clouds.

Chapter 4

Enhancement of troposphere-to-stratopshere transport by small-scale mixing processes[1]

Abstract. Deep convection induced by large forest fires is an efficient mechanism for transport of aerosol particles and trace gases into the upper troposphere and lower stratosphere (UT/LS). For many pyro-cumulonimbus clouds (pyroCbs) as well as other cases of severe convection without fire forcing, radiometric observations of cloud tops in the thermal infrared (IR) reveal characteristic structures, featuring a region of relatively high brightness temperatures (warm center) surrounded by a U-shaped region of low brightness temperatures.

We performed a numerical simulation of a specific case study of pyroCb using a non-hydrostatic cloud resolving model with a two-moment cloud microphysics parameterization and a prognostic turbulence scheme. The model is able to reproduce the thermal IR structure as observed from satellite radiometry. Our findings establish a close link between the observed temperature pattern and small-scale mixing processes atop and downwind of the overshooting dome of the pyroCb. Such small-scale mixing processes are strongly enhanced by the formation and breaking of a stationary gravity wave induced by the overshoot. They are found to enhance the stratospheric penetration of the smoke by up to 30 K and thus are

[1]This Chapter is based on the manuscript " Small-scale mixing processes enhancing troposphere-to-stratosphere transport by pyro-cumulonimbus storms" by G. Luderer, J. Trentmann, K. Hungershöfer, M. Herzog, M. Fromm, and M. O. Andreae, published in Atmospheric Chemistry and Physics Discussions [*Luderer et al.*, 2007b].

of major significance for irreversible transport of forest fire smoke into the lower stratosphere.

4.1 Introduction

Deep convection induced by large forest fires is a highly efficient mechanism for the vertical transport of gaseous and particulate fire emissions. In its most extreme form, this fire-induced convection is called pyro-Cumulonimbus (pyroCb), a phenomenon shown by both observational and modeling studies to result in direct injection of substantial amounts of smoke as high as into the lower stratosphere [*Fromm and Servranckx*, 2003; *Fromm et al.*, 2005; *Rosenfeld et al.*, 2007; *Trentmann et al.*, 2006; *Luderer et al.*, 2006]. Due to a different chemical environment and the lack of washout processes, the lifetime of many tracers, such as aerosol particles and NO_y, is greater in the lower stratosphere than in the troposphere. The injection of biomass smoke therefore results in a substantial perturbation of the chemical composition and the radiative balance of the upper troposphere and lower stratosphere (UT/LS) region, with potentially far reaching consequences for atmospheric chemistry and even climate.

The Chisholm fire is one of the largest forest fires ever observed; it has been scientifically documented and thoroughly analysed in terms of its fire characteristics [*ASRD*, 2001; *Fromm and Servranckx*, 2003] as well as its atmospheric impact [*Fromm and Servranckx*, 2003; *Trentmann et al.*, 2006; *Luderer et al.*, 2006; *Rosenfeld et al.*, 2007]. Here, it serves as a case study for the assessment of the structure of overshooting cloud tops.

This study links two important aspects of intensive deep convection: The occurrence of characteristic cloud top temperature patterns that are regularly associated with pyroCbs and other intensive thunderstorms (cold U with an enclosed warm center, see below), and the role of small-scale mixing processes at the cloud top in troposphere-to-stratosphere transport (TST).

Understanding and quantification of TST from mid-latitude deep convection is not only important for pyroCbs, but also for intensive regular thunderstorms. Even though mid-latitude deep convection accounts for only a small fraction of the air masses in the lowermost extra-tropical stratosphere [*Holton et al.*, 1995], this process is very important for the budgets of many trace species in the lower stratosphere, most notably water vapor as well as some short-lived species [*Mullendore et al.*, 2005]. This is due to the rapid and direct transport from the planetary boundary layer, where most tracers have their sources. Several studies, e.g., *Fischer et al.* [2003], *Ray et al.* [2004], *Hanisco et al.* [2007] and *Pittman et al.* [2007],

report direct observational evidence for the influence of water vapor and tracers into the lower stratosphere due to deep convection at high- and mid-latitudes. Numerical studies using cloud resolving models have investigated the characteristics of TST induced by deep convection. *Wang* [2003, 2007] identified gravity wave formation and breaking atop convective thunderstorm clouds as an important process for the injection of moisture plumes into the lower stratosphere. *Lane et al.* [2003] and *Lane and Sharman* [2006] found that the breakdown of gravity waves generated by thunderstorms is an important source of turbulence above the cloud and at tropopause level. *Mullendore et al.* [2005] assessed the vertical transport of idealized passive tracers by deep convection and found that, in addition to latent heating, mixing processes contribute significantly to potential temperature increases necessary for irreversible TST.

When observed from space, many pyroCbs, as well as intense regular thunderstorm clouds, feature a distinct cloud top temperature pattern. Due to its structure with a warm center surrounded by a U-shaped cold region, this feature will hereafter be referred to as the "cold U/warm center". Typically, cold U brightness temperatures are lower than the tropopause minimum, while the temperatures in the warm center are higher than the temperatures of ambient air at the cloud top altitude. Observations of such thermal structures have been reported repeatedly in the literature [e.g., *Heymsfield et al.*, 1983; *Heymsfield and Blackmer, Jr*, 1988; *Levizzani and Setvák*, 1996; *Setvák et al.*, 2007; *Rosenfeld et al.*, 2007].

Most of these studies agree that the cold U region is due to air masses that have cooled while ascending adiabatically beyond their level of neutral buoyancy [e.g., *Heymsfield and Blackmer, Jr*, 1988; *Rosenfeld et al.*, 2007]. There is, however, substantial uncertainty about the cause of the warm center. In a recent study based on analysis of brightness temperatures at various wavelengths, *Setvák et al.* [2007] found that, for some storms, moisture plumes above the anvil level reach equilibrium with high stratospheric temperatures and mask the colder temperatures of the underlying cloud tops, thus giving rise to the observed warm center. Other studies suggested effects related to variations in radiative properties of cloud hydrometeors at the cloud top, with optically less opaque hydrometeors in the center allowing IR radiometers to see further down to a lower, hence warmer level of effective emission [*Heymsfield et al.*, 1983]. In this paper, we will demonstrate that both observations and simulations suggest that neither moisture masking nor effects related to the hydrometeors' radiative properties were relevant in our case study. The analysis of *Rosenfeld et al.* [2007] showed that the emissivity in the core is close to unity and does not show any inferred change of particle size in the warm center. Based on these observational results, and the simulation of the

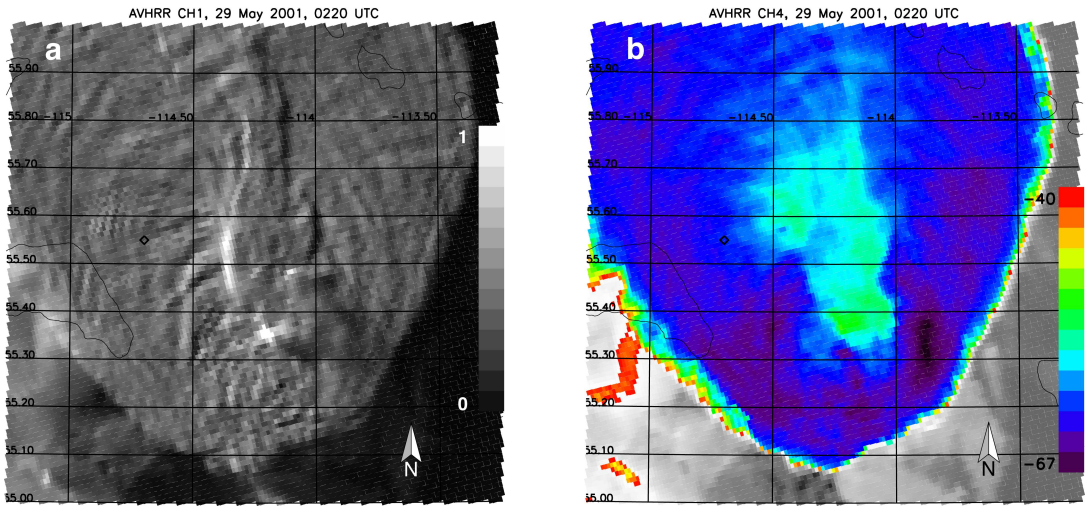

(a) 0.65 μm reflectance

(b) 10.8 μm brightness temperature

Figure 4.1: Images from a NOAA AVHRR overpass during the mature phase of pyroCb convection. Reflectance in the visible 0.65 μm channel is depicted in (a), brightness temperatures measured by the 10.8 μm thermal IR channel are shown in (b). Reproduced from *Rosenfeld et al.* [2007].

Chisholm pyroCb presented here, we infer that the warm center originated from subsidence and mixing of stratospheric air masses induced by gravity wave activity. This explanation is in good agreement with those proposed in earlier studies by *Adler and Mack* [1986] and *Schlesinger* [1984].

This paper is structured as follows: In the next section, observations of the Chisholm pyroCb are presented. In Section 3, the Active Tracer High Resolution Atmospheric Model (ATHAM) and the model setup used for this study are described. Section 4 presents an analysis of the cloud top structure based on the model results. Discussions and conclusions are presented in Section 5.

4.2 Observations

The Chisholm fire serves as a case study for this paper. In terms of its atmospheric impacts, the Chisholm fire is the largest boreal forest fire ever to be scientifically documented. Its fire characteristics were thoroughly documented by the Alberta Sustainable Resource Development agency. According to the post-burn assessment presented in *ASRD* [2001], the Chisholm Fire burned an area of 50,000 ha in the time of its most intensive activity between 1700 and 2400 local time on 28 May 2001 alone. The fire intensity was up to 239,000 kW m^{-1} [*Trentmann et al.*, 2006; *ASRD*, 2001, and Chapter 2]. The severe intensification of the fire-

induced convection was observed to coincide with the passage of a synoptic cold front. As documented by numerous satellite and ground based observations, it injected substantial amounts of smoke into the lower stratosphere, which persisted for several months and resulted in a significant enhancement of the lower stratospheric aerosol loading on a hemispheric scale [*Fromm and Servranckx*, 2003; *Fromm et al.*, 2007a,b] *Rosenfeld et al.* [2007] analyzed the structure, precipitation and lightning activity of the pyroCb based on satellite and radar data and found that the convection reached an altitude of about 13.5 km. In an earlier modeling study, *Trentmann et al.* [2006] and *Luderer et al.* [2006] reproduced the observed structure of the Chisholm pyroCb, and assessed its sensitivity to fire activity and meteorological background conditions (cf. also Chapters 3and 5). It was found that the main driving forces for the vertical development of the convection and subsequent TST of smoke were the release of sensible heat from the fire and the background meteorological conditions, while the release of latent heat in the form of water vapor and the presence of aerosol particles acting as cloud condensation nuclei was of much lesser importance.

Not only the stratospheric aerosol plume produced by the Chisholm fire, but also the pyroCb convection itself was well captured by satellite observations [*Fromm and Servranckx*, 2003; *Rosenfeld et al.*, 2007]. Fortuitously, a NOAA Advanced Very High Resolution Radiometer (AVHRR) overpass occurred at 0220 UTC during the mature phase of the pyroCb convection. The anvil of the pyroCb is clearly visible in both the 0.65 μm channel (Figure 4.1a) and the thermal IR at 10.8 μm (Figure 4.1b).

The fire was located between approximately 55.0°N and 55.2°N at 114.3°W, below the southern edge of the pyroCb anvil. Due to strong southerly winds associated with the passing cold front, the convection cell was tilted to the north and the anvil spread to northward directions. The areas of maximum reflectance and the shadows cast in the 0.65 μm give a good indication of the location of the overshooting dome.

The cloud top temperatures of the pyroCb are much lower than those of the surrounding clouds that were not affected by the fire, showing that the fire induced convection reached much higher than ambient convection. As is the case for a number of other pyroCbs, the Chisholm pyroCb features a distinct pattern when observed from space with a thermal IR radiometer. While most of the anvil region is characterized by brightness temperatures of about -61°C to -59°C, corresponding to the tropopause cold point temperature level, a region with brightness temperatures that exceed those in the other parts of the anvil by 5-10 K is evident at the center of the pyroCb's top. This warm center structure is located above and

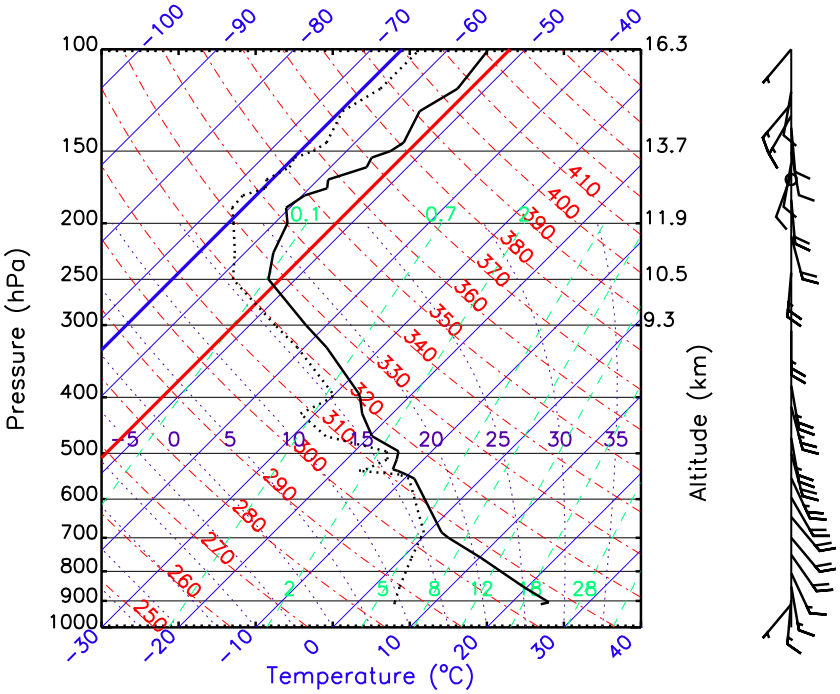

Figure 4.2: Skew-T diagram depicting vertical profiles of temperature (solid line) and dew point temperature (dotted line) measured at Edmonton at 00 UTC. The thick red and blue isotherms indicate the maximum and minimum cloud top brightness temperatures as measured by the AVHRR. These deviate substantially from background tropopause temperatures. This sounding was also used for the initialization of the background meteorology in the model simulations. The arrows indicate the wind profile, with every full barb corresponding to 10 $\mathrm{m\,s^{-1}}$.

downwind of the overshooting dome. In the upwind direction, the warm center is surrounded by an arch-shaped area of very cold temperatures. The background temperature profile at the time and location of the pyroCb convection was obtained from the radiosonde observations recorded at 00 UTC at Edmonton (Figure 4.2), at about 200 km distance and shortly before the time of the convective blow-up of the pyroCb. The cloud top temperature structure is very remarkable since the coldest temperature of −66°C is much colder than the tropopause cold point. Conversely, the warmest areas are warmer than −52°C. According to this sounding, temperatures were −53.7°C or lower throughout the lower stratosphere. The observed temperature maximum can therefore not be explained by the overshooting into warm areas of the lower stratosphere alone.

According to *Inoue* [1987], the actual cloud top temperature nearly equals the cloud top thermal temperature if the difference between the brightness temper-

atures recorded at 10.8 μm and 12.0 μm is within a fraction of a degree. Since the brightness temperature difference is near zero throughout the center of the Chisholm pyroCb's cloud top [*Rosenfeld et al.*, 2007], we conclude that the observed brightness temperature pattern is representative of the actual temperature structure at the cloud top.

The cold U/warm center structure of the Chisholm pyroCb was also captured by the Defense Meteorological Satellite Program (Rene Servranckx, personal communication, 2005) and shows up as a persistent feature in the GOES geostationary satellite imagery (Fromm et al., 2007a). Similar cloud top brightness temperature patterns were also observed for other pyroCbs [*Fromm et al.*, 2005] as well as regular thunderstorms (see Introduction), indicating that these are characteristic features of intensive convection.

4.3 Model setup

The numerical simulations presented here were performed with the Active Tracer High resolution Atmospheric Model (ATHAM), a non-hydrostatic cloud-resolving model originally designed for the simulation of the extreme dynamical conditions present in plumes. In earlier studies, ATHAM was employed to investigate volcanic eruptions [e.g., *Oberhuber et al.*, 1998; *Herzog et al.*, 1998; *Graf et al.*, 1999; *Textor et al.*, 2003] and wildfire induced convection [*Trentmann et al.*, 2002, 2006; *Luderer et al.*, 2006].

The dynamical core of ATHAM is such that it fully accounts for the effects of all tracers such as hydrometeors, aerosols and gaseous components on heat capacity and density. The feedback of liquid and frozen cloud particles on the convection dynamics is therefore explicitly represented. The Euler equation is solved for a gas-particle mixture under the assumption of zero net fluxes between its constituents for momentum and heat. The volume mean momentum is conserved. The tracer advection is formulated in mass-conserving form.

For realistic simulation of entrainment of environmental air into the the plume, as well as detrainment and mixing of smoke at the cloud top, subgrid scale turbulence is parameterized using a modified TKE scheme. In this approach, turbulent kinetic energy (TKE) is a prognostic variable from which the horizontal and vertical turbulent exchange coefficients are derived [*Herzog et al.*, 2003]. Cloud microphysical processes are represented using a two-moment microphysical scheme [*Textor et al.*, 2006a,b]. There are four hydrometeor classes, namely, cloud droplets (small, liquid), rain drops (large, liquid), ice crystals (small, frozen), and graupel (large, frozen), for each of which mass concentrations and number densities are pre-

dicted. A total of 13 processes transferring water between the four hydrometeor classes and the vapor phase are considered.

The model setup is identical to that used for the simulations presented in Chapter 5. The fire forcing is assumed to be constant during the simulation and is represented as a rectangular front of 15,000 m length and 500 m width. The model domain is 85 km in the direction along the fire front and 65 km across, with the upper boundary at 26 km. The number of grid points used is 110×85 in the x- and y-directions and 100 in the z-direction. We used a focusing grid with maximum resolution at the fire and its vicinity, where the gradients of tracer concentrations and temperature are largest. Towards the edges of the model domain, the grid spacing is larger. In the horizontal, the minimum grid spacing was set to 100 m perpendicular to the fire front and 500 m along the front. In the vertical, we used two regions of enhanced spatial resolution: the grid spacing was 50 m at the ground and, for more accurate simulation of troposphere-to-stratosphere transport, 150 m at the tropopause. In the mid-troposphere, the maximum vertical spacing was 300 m.

The fire was assumed to consume 9 kg m^{-2} of fuel at a rate of spread of 1.5 m s^{-1}. In this simulation run we assumed that 100% of the fire energy goes into the heating of the atmospheric layer over the fire, i.e., radiative losses were assumed to be zero. A fuel moisture value of 40% based on dry fuel mass was assumed. This yields a fire intensity, i.e., sensible heat release per unit fire front length, of 239×10^6 W m^{-1}, and a moisture release of 12.2 kg m^{-1} s^{-1}. For the aerosol emissions, we used an emission factor for total particulate matter (TPM) of 17.6 g_{TPM} kg_{fuel}^{-1} [*Andreae and Merlet*, 2001] and assumed, for the particles, a volume mean diameter of 0.2 μm, which is consistent with *Reid et al.* [2005].

Background meteorology was adopted from radiosonde observations that were performed at Edmonton (53.5° N, 114.1° W), located about 200 km south of the fire location, at 00:00 UTC, shortly before the time of the blow-up (Figure 4.2). This sounding is likely to closely match the meteorological background condition for the Chisholm pyroCb. Based on ECMWF reanalysis data, the dynamical tropopause (defined as the 2 PVU potential vorticity level) was located at a potential temperature of 332 K, corresponding to an altitude of 11.2 km. Here, we opted to use the tropopause definition in terms of potential vorticity (PV) since it is most meaningful in terms of troposphere-stratosphere exchange at mid-latitudes. Since the PV isosurfaces become strongly disturbed during the active convection, we use the 332 K isentrope of potential temperature to calculate the TST from the model simulation.

Given the complicated three-dimensional structure of the pyroCb, the interac-

tion of its dynamics with incident solar and thermal radiation from the fire are highly complex. Interactive broadband three-dimensional simulation of radiation is computationally much too expensive for simulations with cloud-resolving models such as ATHAM. Therefore, the following assumptions were made. Since most of the radiative energy from the fire is absorbed by the pyro-cloud, we assumed that the entire fire energy becomes available for the convection. This is consistent with the finding presented in *Luderer et al.* [2006, and Chapter 5] that the observed structure of the pyroCb can only be reproduced, if the radiative loss is small compared to the fire energy release. Moreover, effects of solar heating were assumed to be negligible. While it likely contributed substantially to the lofting of the stratospheric aerosol plume during the days after the Chisholm fire, solar heating is of low significance for the convective time scales of less than one hour and the large solar zenith angles during the convective phase considered here.

In order to compare the simulations with satellite observations of brightness temperature, an offline-simulation of the radiative properties of the pyroCb was performed using a one-dimensional, broadband, δ-four-stream radiative transfer model [*Fu and Liou*, 1993; *Hungershöfer*, 2007]. At each vertical column of the ATHAM grid, an independent-column calculation was performed. Up to an altitude of 26 km, the vertical model layers were adopted from ATHAM. For the remaining part up to the top of the atmosphere at 80 km, data for a standard mid-latitude summer atmosphere [*Anderson et al.*, 1986] were applied. In total, this resulted in 129 horizontally homogenous layers with a thickness varying from 50 m near the surface to 10 km in the mesosphere. The brightness temperature was determined from the upward-directed flux density at the top of the atmosphere for the wavelength band from 10.2 μm to 12.5 μm. In this atmospheric window region, only the absorption of water vapor and the effect of the hydrometers had to be taken into account. To determine the optical properties of the four hydrometeor classes, pre-calculated values were scaled with the respective mass concentrations simulated with the ATHAM model. In the case of water droplets, a constant effective radius of 5 μm was assumed. For ice crystals, a plate-like structure with an effective size of 25 μm was applied, which roughly corresponds to an effective radius of about 10 μm as obtained in the retrieval by *Rosenfeld et al.* [2007]. Aerosol optical properties were considered as well, but their influence was found to be small in the wavelength region considered.

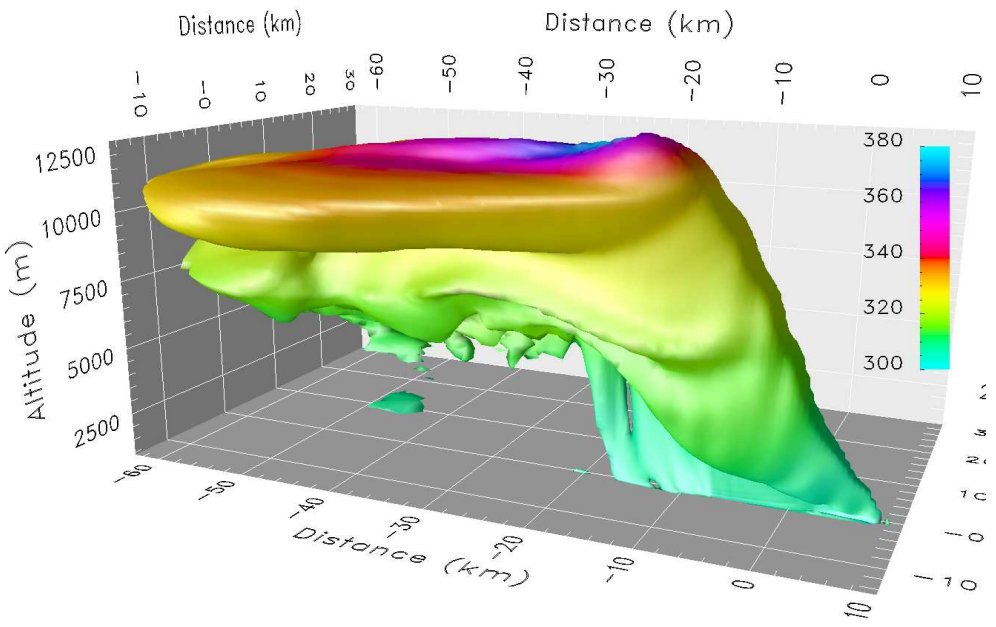

Figure 4.3: Three-dimensional representation of the aerosol plume after 40 min simulation time. The 50 $\mu g\,m^{-3}$ isosurface is color-coded with potential temperature in K.

4.4 Model Results

Two- and three-dimensional visualizations of the modeled smoke plume are provided in Figures 4.3 and 4.4. Figure 4.3 depicts the 50 $\mu g\,m^{-3}$ isosurface of aerosol mass concentration color coded with potential temperature θ. In the coordinate frame used for the simulations, the x-direction is aligned with the fire front orientation and is therefore rotated with respect to north by 165°. The overshooting cloud top is centered at $x = 15$ km, $y = -5$ km and reaches to a maximum altitude of about 13,000 m. At this altitude level, background winds were blowing from south-south-west, at an angle of about 25 ° to the x-axis. In order to optimally capture the overshooting cloud top and its substructure, the vertical 2d cross sections presented here were prepared along the $y = -5$ km line. The vertical cross section of the aerosol mass distribution depicted in Figure 4.4 shows that the plume reached a peak altitude of 13 km, well above the tropopause, which was located at 11.2 km. The maximum potential temperature at the cloud top was approximately 360 K.

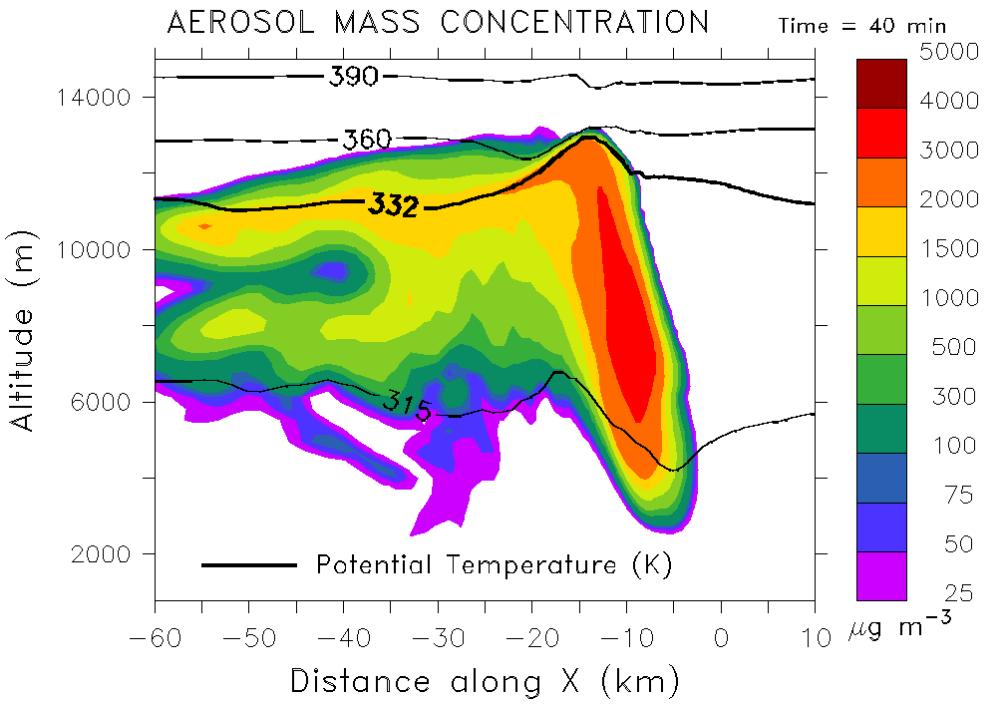

Figure 4.4: Aerosol mass concentration along the $y = -5$ km vertical cross section. Contour lines indicate potential temperature levels. The tropopause was located at θ=332 K.

4.4.1 Simulated radiative and thermal structure of the cloud top

Top views of the modeled smoke cloud at three different times are given in Figure 4.5. The pyroCb is represented by the 0.5 g kg^{-1} hydrometeor concentration isosurface and has been color-coded with the temperature field on this isosurface, thus showing the "skin temperature" of the cloud top. Similar to the satellite observations, the thermal structure of the cloud top features a warm center partially surrounded by an arch-shaped region of cold temperatures.

Figure 4.6 shows results from offline calculations of the pyroCb's radiative properties after 40 min simulation time. Figure 4.6(a) presents the extinction coefficient resulting from aerosols and hydrometeors in the AVHRR 10.8 μm wavelength channel. At this wavelength, scattering is much less significant than absorption, and the extinction is dominated by hydrometeors. The extinction coefficient is highly variable throughout the pyroCb, with maximum values of 0.25 m^{-1} in the non-frozen part of the updraft, and more moderate extinction at the cloud top and the anvil. Figure 4.6(b) depicts the total optical depth relative to the top of the atmo-

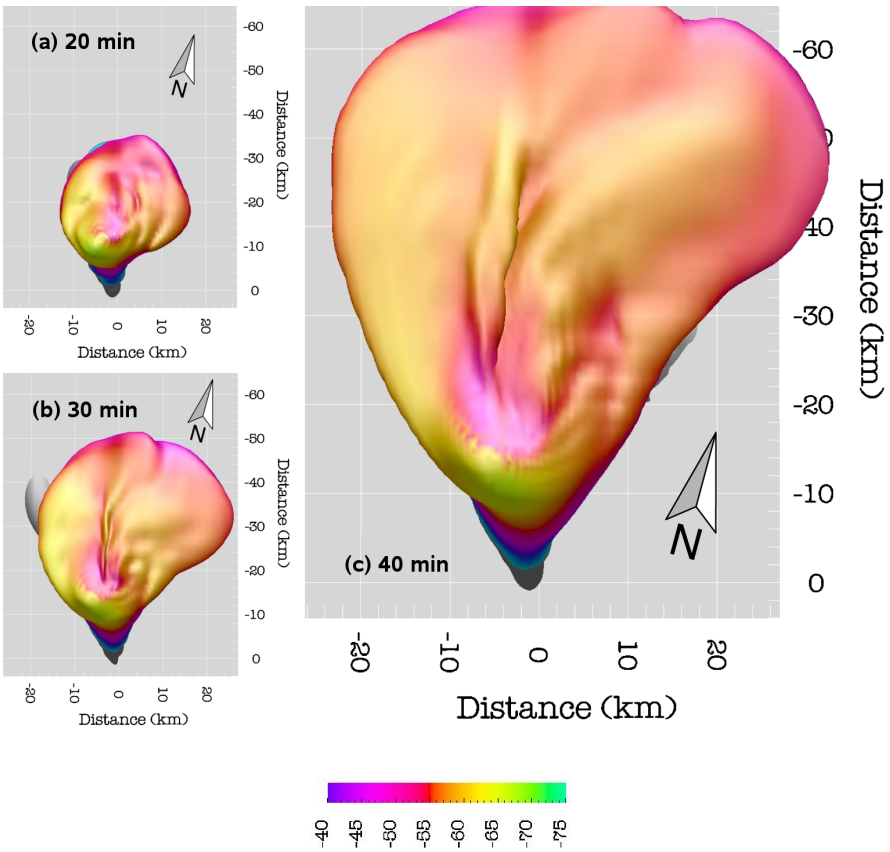

Figure 4.5: Cloud top temperatures in °C on the 0.5 g kg^{-1} hydrometeor concentration isosurface as simulated by ATHAM for three instances in time.

sphere. The τ=1 contour can be used to estimate the effective thermal emission level [e.g., *Thomas and Stamnes*, 1999]. Even though the aerosol and hydrometeor extinction is small at the cloud top compared to the pyroCb center, the τ=1 level is located very close to the cloud top, indicating that the temperature structure observed by the satellite radiometer is representative of the conditions at the cloud top. This explains the close agreement between modeled brightness temperature (Figure 4.7) and modeled in situ "skin temperature" (Figure 4.5c). As discussed in Section 4.2, the observations also support the conclusion that the cloud was optically thick in the thermal IR. Hence the occurrence of the cold U/warm center structure must have been due to dynamic effects at the cloud top rather than radiative effects.

The simulated cloud top brightness temperature structure (Figure 4.7) is in good agreement with the observations. When viewed from above, the warm center is located at the downwind side of the overshooting dome, while the minimum cloud top temperatures are found on the upwind side of the overshoot. For most of the anvil, brightness temperatures are in the −56 to −59°C range, roughly in

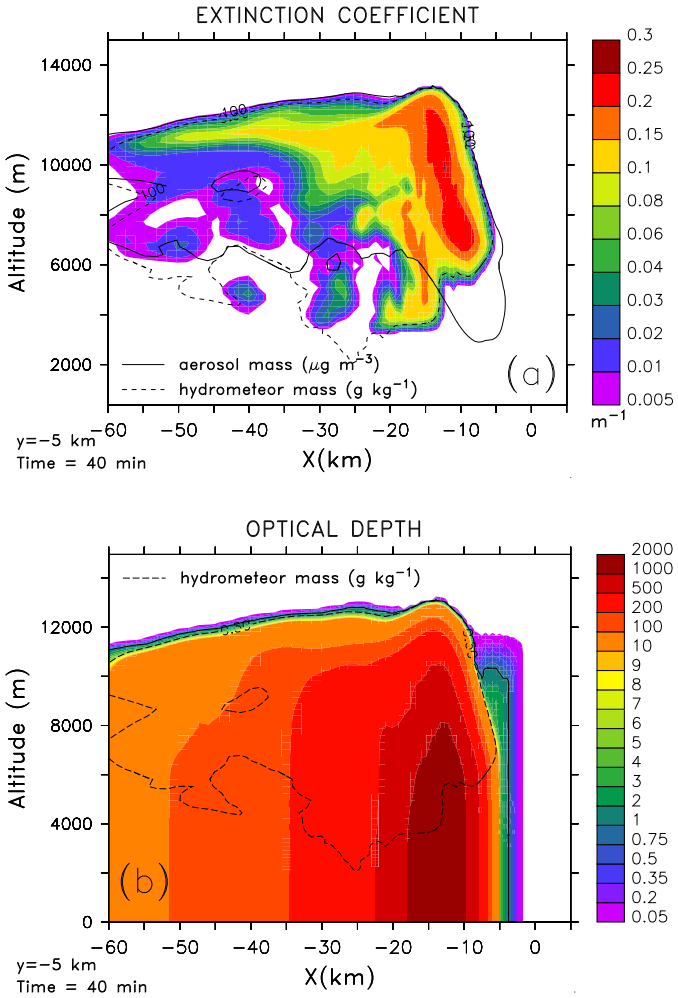

Figure 4.6: Results from offline calculation of radiative properties. (a) Extinction due to absorption and scattering by hydrometeors and aerosols at 10.8 μm. Contours of aerosol mass concentration (solid line) and hydrometeor concentration (dashed line) indicate the extent of the smoke plume and pyroCb. (b) Aerosol and hydrometeor extinction optical depth τ at 10.8 μm from the top of the atmosphere as a function of z. Note that the τ=1 contour (solid line), which can be used as an indication of the effective level of emission of the thermal radiation, is situated very close to the cloud top.

equilibrium with the tropopause temperature level at this altitude. These brightness temperatures are slightly warmer, by 2-3 K, than in the observations, but are consistent with the uncertainty in the background temperature profile and the anvil altitude, which might have been slightly underestimated by our ATHAM simulations. The maximum cloud top brightness temperature in the warm center is −48°C, substantially warmer than the −58°C of the ambient air at this altitude. On the other hand, the minimum brightness temperatures in the cold U region are

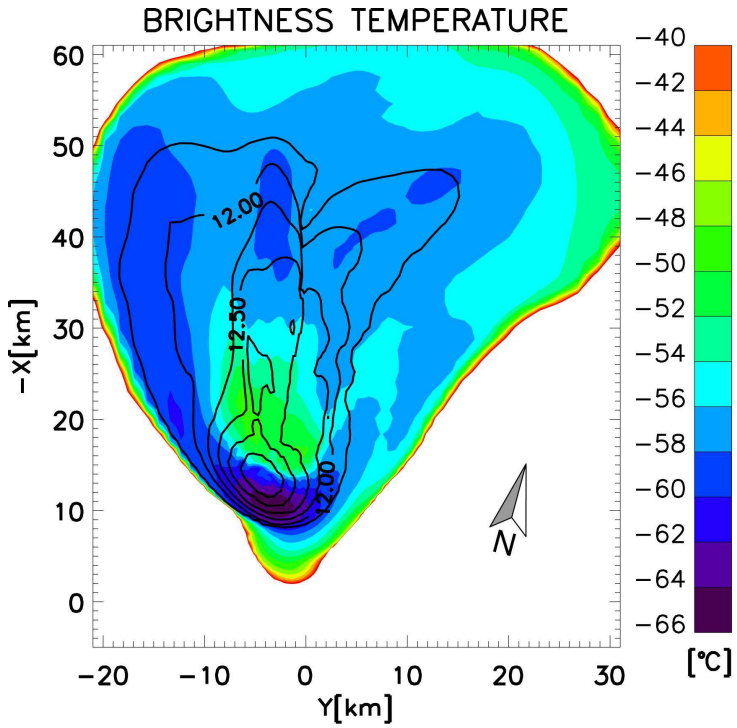

Figure 4.7: Brightness temperatures derived from upwelling radiance simulated for the 10.8 μm wavelength band. The contour lines indicate the altitude in km of the 100 μg m^{-3} isosurface of the aerosol mass concentration.

close to −65°C, about 5°C colder than the tropopause cold point. The difference of 17°C between the simulated maximum and minimum cloud top temperatures is in good agreement with the AVHRR brightness temperature field, where a difference of 15°C between the warm center and the cold U was recorded (see Section 4.2 and Figure 4.1b).

4.4.2 Gravity wave formation

Vertical cross sections through the pyroCb reveal the physical reason for the observed cloud top temperature structure. Figure 4.8(a, b) depict the temperature anomaly, i.e., the difference between in-situ temperature within the pyro-cloud and the background temperature at the corresponding altitude level on the vertical plane parallel to the fire front at $y = -5$ km. It shows a distinct bipolar temperature structure, featuring a strong negative temperature anomaly within the pyroCbs overshooting dome, accompanied by a strong positive temperature anomaly above and downwind (Figure 4.8b). A similar bipolar structure is also found in the pressure anomaly and vertical wind fields, indicating a stationary

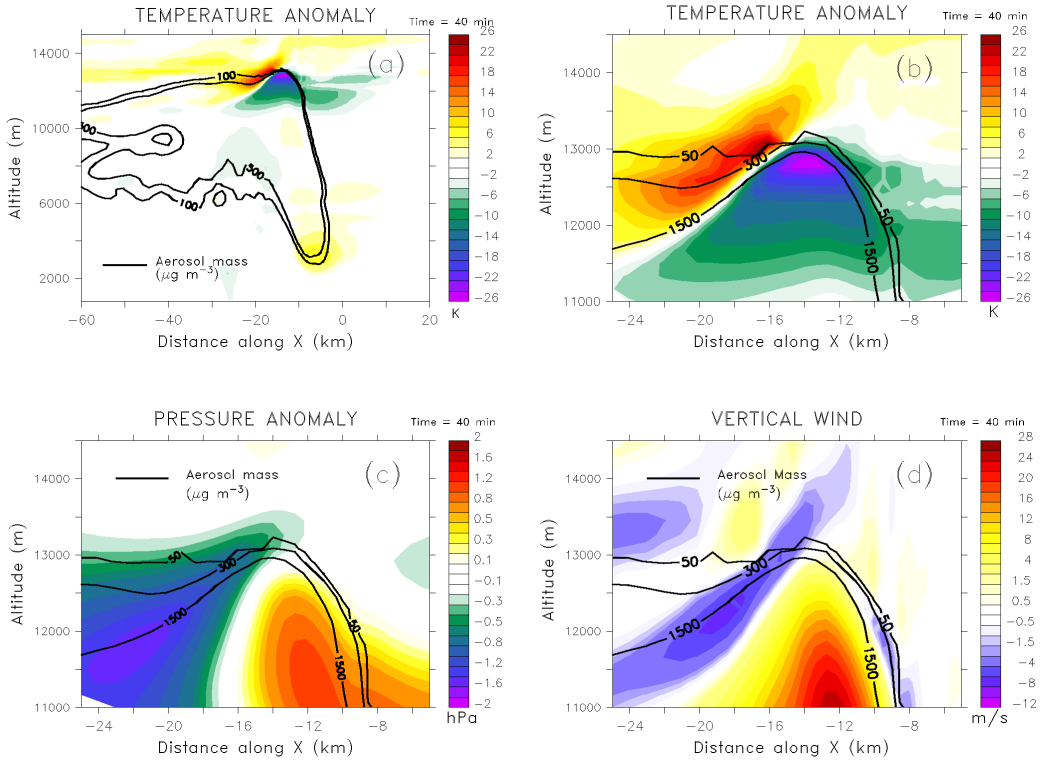

Figure 4.8: Vertical cross-sections of (a,b) temperature anomaly, (c) pressure anomaly, and (d) vertical wind field at y=-5km. Solid black lines indicate isolines of aerosol concentration. Temperature and pressure anomalies are defined as the difference with respect to the background temperature and pressure profiles. The distinct bipolar structure is a clear indication of gravity wave activity.

gravity wave induced by the overshoot: The cold overshooting air masses are negatively buoyant and tend to sink as they are advected downwind, thereby creating a negative pressure anomaly on the downwind side of the overshoot (Figure 4.8c). In turn, this negative pressure anomaly induces downward motion of air masses from above the cloud top (Figure 4.8d). Due to adiabatic heating, this process gives rise to the strong positive temperature anomaly above and downwind of the overshooting dome.

The gravity wave also shows up prominently as a strong perturbation in the potential temperature field (Figure 4.9g). The air masses in the warm area right above the cloud top feature θ-values of up to 380 K, indicating that these air masses originate from an altitude level of 13,600 m, having descended as much as 600 m.

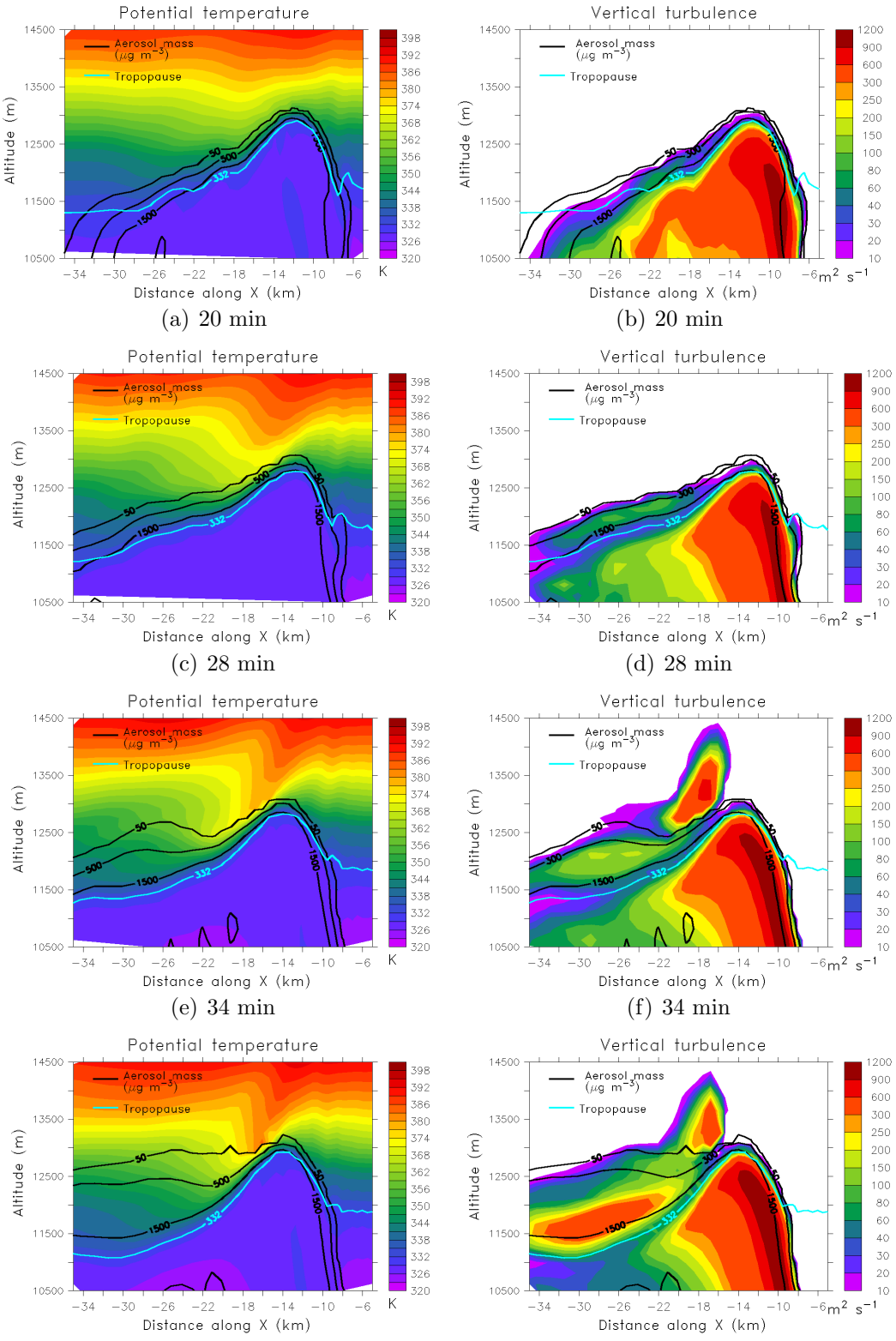

(a) 20 min (b) 20 min

(c) 28 min (d) 28 min

(e) 34 min (f) 34 min

(g) 40 min (h) 40 min

Figure 4.9: Vertical cross sections of potential temperature (left column) and vertical turbulent exchange coefficient (right column) for four different points in time. Due to the anisotropic treatment of turbulence in ATHAM [*Herzog et al.*, 2003], the verticlal turbulent exchange coefficient K_{ver} is related to the horizontal turbulent exchange coefficient K_{hor} as $K_{ver} = \sqrt{2}K_{ver}$.

4.4.3 Cross-isentrope transport due to small-scale mixing

The gravity wave induced by the overshooting cloud top enhances the cross-isentrope transport of smoke laden air into the lower stratosphere in two ways. First, the close proximity of the pyroCb's overshooting dome, with its strong negative temperature anomaly, to a region of air masses with stratospheric origin and positive temperature anomaly above and downwind of the dome results in very large gradients of potential temperature and trace gas concentration directly atop of the overshooting dome. Second, gravity wave breaking generates additional turbulence, thereby greatly enhancing the mixing efficiency.

Figure 4.9 depicts vertical cross sections through the fields of potential temperature (a, c, e, g) and of the vertical turbulent exchange coefficient, as simulated by ATHAM's turbulence scheme (b, d, f, h) for four points in time. During the first 20 min of the development of the pyroCb, the air masses in the cloud are highly turbulent, with maximum values of the vertical turbulent exchange coefficient of up to 1500 $m^2\ s^{-1}$ at the center of the updraft. The strong gradient of potential temperature above the overshooting dome, i.e., a very stable stratification, acts as a sink for turbulent kinetic energy. Therefore, the turbulent exchange coefficient strongly decreases at the cloud top.

After about 30 min of simulation time, the gravity wave becomes unstable due to the vertical wind shear at the tropopause level. Downwind of the overshooting dome, air masses with high potential temperature are transported below potentially colder air masses, resulting in gravity wave breaking (Figure 4.9e). Such gravity wave breaking is a highly efficient mechanism for the generation of turbulence (Figure 4.9f). It is evident from the potential temperature and turbulence fields after 40 min (Figures 4.9g, h) that the advection of gravity-wave generated turbulence along the cloud top results in very efficient mixing of smoke laden air masses of the pyro-cloud with potentially warm air masses of stratospheric origin.

As discussed in Section 4.4.2, such cloud top mixing of potentially warm stratospheric air with smoke and hydrometeor enriched pyroCb air gives rise to the warm center structure as observed in the thermal satellite imagery. This establishes a direct link between the thermal structure and TST above deep convection, hence the cold U/warm center feature as derived from satellite could serve as an indicator for the occurrence of TST above deep convection.

4.4.4 Troposphere-to-stratosphere transport

In order to assess troposphere-to-stratosphere transport (TST) of smoke tracers, it is instructive to consider vertical tracer distributions both as a function of altitude,

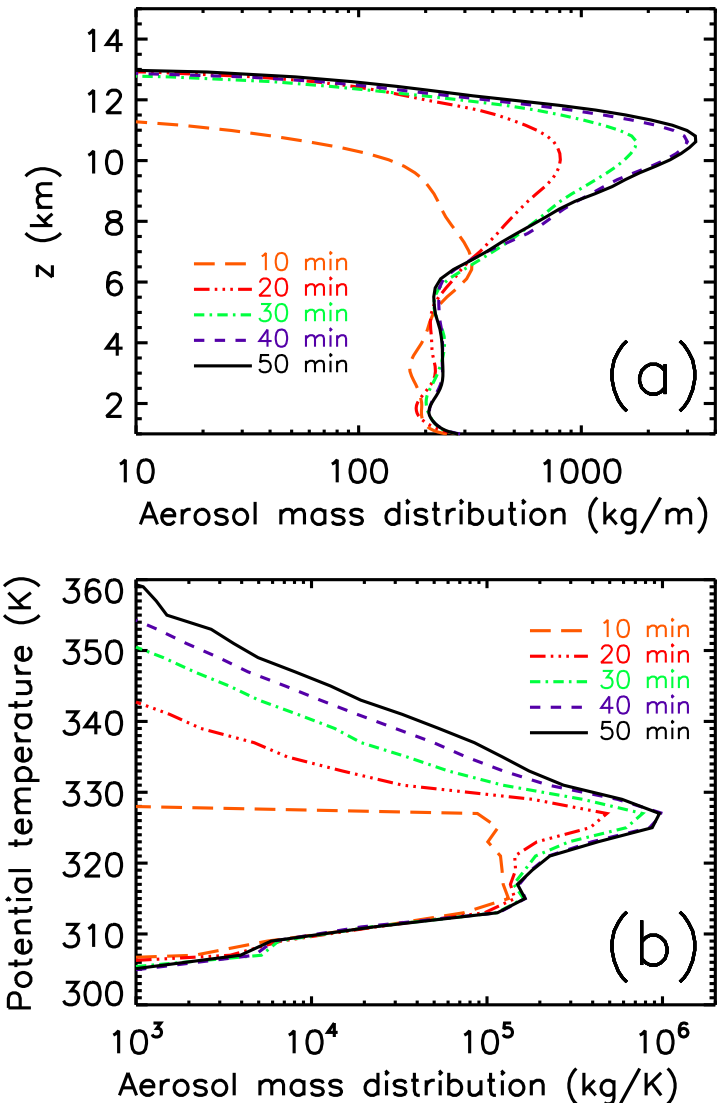

Figure 4.10: Temporal evolution of the vertical distributions of aerosol mass as a function of (a) altitude and (b) potential temperature.

and as a function of potential temperature. The temporal evolution of such vertical aerosol distributions is given in Figure 4.10.

The most notable feature of this analysis is the fact that the maximum penetration altitude is already reached after 20 min, whereas the aerosol distribution as a function of potential temperature continues to progress to higher values as the simulation advances in time.

As shown in Figure 4.10(a), the maximum penetration height is approximately 13,000 m. The main outflow height of the smoke is at 10,500 m, giving rise to

a peak in the vertical aerosol mass distribution at this level. Over the course of the simulation, due to the continuing convective vertical transport of smoke, increasing amounts of aerosol mass become injected and the layers above 7000 m become increasingly enriched in aerosol mass. The maximum penetration height, however, remains almost unchanged once the 13,000 m level is reached after about 20 min, i.e., the strong inversion in the lower stratosphere inhibits further vertical ascent of the air parcels in the overshoot to higher altitude levels.

In terms of TST, however, the aerosol distribution as a function of potential temperature θ is more meaningful (Figure 4.10b). In order to mask out the high temperatures directly above the fire, only smoke parcels above an altitude of 5000 m were considered for the analysis presented here. At this level, the sensible heat from the fire is sufficiently diluted, so that the high potential temperature tail of the aerosol distribution represents smoke located in the tropopause region only. In contrast to the maximum penetration altitudes, the maximum θ-values reached by the aerosol plume continue to rise to higher levels: The aerosol density exceeds 1000 kg K^{-1} up to a potential temperature level of 342 K after 20 min, 350 K after 30 min, 354 K after 40 min and 359 K after 50 min.

The continuous increase in maximum potential temperature without an increase in maximum altitude strongly supports the finding that, in addition to convective advection, other driving forces are responsible for the cross-tropopause transport at the cloud top. We can assess the relative importance of turbulent mixing by considering the energy balance of an individual air parcel.

The difference in potential temperature between the boundary layer and the lower stratosphere is typically of the order of several tens of K. According to traditional parcel theory, the most important heat source in an air mass ascending within a convection column is the latent heat from condensing water. The equivalent potential temperature incorporates the amount of latent heating that would be added if all the water vapor contained in the air parcel was condensed. In the case of the Chisholm fire, equivalent potential temperature was almost constant throughout the lower troposphere. If a modified equivalent potential temperature definition that also takes into account the latent heat of freezing is used, values are in a range between 320 and 322 K from the boundary layer to an altitude of about 8 km. The equivalent potential temperature of the tropopause, by contrast, was 332 K – hence latent heating alone would not have been sufficient to lift air masses into the lower stratosphere. For pyroCbs, of course, heating from the fire is an important additional contributor to the internal energy of air parcels. As discussed in Chapter 3, it is estimated that the fire heating contributed about 6 K to the temperature of air parcels at the anvil level of the Chisholm pyroCb. The

combined effect of latent heating and fire heating can yield potential temperatures of 328 K. This is in good agreement with the main outflow level of the pyroCb. On the other hand, as shown by Figure 4.10, a substantial fraction of the aerosol mass ends up at much higher potential temperature levels. Neglecting radiative heating, which is not significant on the short time scales considered here, any aerosol mass at $\theta > 328$ K must be the result of mixing with stratospheric air characterized by large values of potential temperature. We can thus conclude that the small-scale mixing processes, most importantly those induced by gravity wave breaking at the cloud top, increased the stratospheric penetration of the pyroCb smoke by as much as 20-30 K.

4.5 Summary and Conclusions

We investigated the cloud top of an intensive pyroCb and provide an explanation for the occurrence of the peculiar cold U/warm center cloud top temperature structure that has also been observed for other cases of severe thunderstorm convection. A close link between the cold U/warm center feature and TST induced by small-scale mixing processes at the cloud top could be established.

The model results presented here show that the cold U/warm center cloud top temperature pattern observed from satellite radiometry can be closely reproduced with the cloud resolving model ATHAM. Analysis of the simulated fields of potential temperature and other prognostic variables of the model demonstrates that this feature is due to dynamic processes at the cloud top: The pyroCb's overshooting dome induces a stationary gravity wave, which strongly enhances mixing of smoke laden air masses of the pyroCb with stratospheric air masses characterized by high potential temperatures. The gravity wave generates large gradients of potential temperature and tracer concentration, and turbulence produced by gravity wave breaking results in efficient mixing across isentropes. While convective advection, latent heating and sensible heating from the fire alone can explain only the transport of air masses to sub-tropopause levels of about 328 K, the small-scale mixing processes presented in this paper are of key importance for the injection of a small but significant fraction of smoke to lower stratospheric potential temperature levels of up to 360 K. Thus, small-scale mixing increased the stratospheric penetration of the smoke by as much as 30 K.

The results presented here are in good agreement with earlier studies of regular thunderstorm convection. Our explanation for the formation of the cold U/warm center structure based on small-scale mixing processes is consistent with the thunderstorm cloud top dynamics presented by *Schlesinger* [1984] and *Adler and Mack*

[1986]. The importance of gravity wave formation and breaking for TST of pyroCb smoke found here is very similar to the role of gravity waves in transporting water vapor to the lower stratosphere by mid-latitude convection as described by *Wang* [2003, 2007]. The close connection between the thermal structure of the cloud top as observed from satellite and TST, as demonstrated in this study, opens up the possibility of assessing the occurrence of TST induced by deep convection using IR satellite observations.

PyroCb induced smoke injection is an important source of trace gases and aerosols in the upper troposphere and lower stratosphere. Modeling studies are an important tool to advance our understanding of the relevant mechanisms. The Chisholm fire case study, presented here and in *Luderer et al.* [2006]; *Trentmann et al.* [2006], suggests that the principal ingredients for direct smoke injection by pyroCbs are 1) strong fire forcing through heat release, 2) favorable meteorological conditions, with, most importantly, sufficient moisture in the lower and mid-troposphere, and 3) small-scale mixing processes at the cloud top.

More studies are needed to further improve our understanding of the causes and effects of UT/LS aerosol plumes originating from forest fires. Moreover, more convection scale modeling studies also for other cases and geographical regions would be desirable. Regional simulations also considering radiative effects for longer timescales and larger spatial scales would enhance the understanding of the further development of lower stratospheric aerosol plumes induced by pyroCbs. Finally, global chemistry climate models should be used to assess the effect of forest fire smoke on radiative balance and lower stratospheric chemistry.

Chapter 5

Sensitivity studies[1]

Abstract. The Chisholm forest fire that burned in Alberta, Canada, in May 2001 resulted in injection of substantial amounts of smoke into the lower stratosphere. We used the cloud-resolving plume model ATHAM (Active Tracer High resolution Atmospheric Model) to investigate the importance of different contributing factors to the severe intensification of the convection induced by the Chisholm fire and the subsequent injection of biomass smoke into the lower stratosphere. The simulations show strong sensitivity of the pyro-convection to background meteorology. This explains the observed coincidence of the convective blow-up of the fire plume and the passage of a synoptic cold front.

Furthermore, we performed model sensitivity studies to the rate of release of sensible heat and water vapor from the fire. The release of sensible heat by the fire plays a dominant role for the dynamic development of the pyro-cumulonimbus cloud (pyroCb) and the height to which smoke is transported. While the convection is very sensitive to the heat flux from the fire, the emissions of water vapor play a less significant role.

The aerosol burden in the plume has a strong impact on the microphysical structure of the resulting convective cloud. The dynamic evolution of the pyroCb, however, is only weakly sensitive to the abundance of cloud condensation nuclei (CCN) from the fire. In contrast to previous findings by other studies of convective clouds, we found that fire CCN have a negative effect on the convection dynamics because they give rise to a delay in the freezing of cloud droplets. Even in a simulation without fire CCN, there is no precipitation formation within the updraft region of the pyroCb. Enhancement of convection by aerosols as reported from

[1]This Chapter is based on the manuscript "Modeling of biomass smoke injection into the lower stratosphere by a large forest fire (Part II): Sensitivity studies" by G. Luderer, J. Trentmann, T. Winterrath, C. Textor, M. Herzog, H.-F. Graf and M. O. Andreae, published in Atmospheric Chemistry and Physics [*Luderer et al.*, 2006].

studies of other cases of convection is therefore not found in our study.

5.1 Introduction

Large forest fires regularly release enough energy to lift the smoke-laden air beyond the condensation level, resulting in the formation of a cumulus cloud. Deep-convective storm clouds induced by fires are often referred to as pyro-cumulonimbus (pyroCb) [*Fromm et al.*, 2005; *Damoah et al.*, 2006]. Due to the fire emissions of sensible heat, latent heat in the form of water vapor, and aerosol particles that can act as cloud condensation nuclei (CCN), pyroCbs have unique dynamic and microphysical structures. It is well established that severe convection is an important mechanism for troposphere-to-stratosphere transport in the mid-latitudes [*Wang*, 2003; *Mullendore et al.*, 2005]. Similarly, pyroCbs can reach to the upper troposphere and lower stratosphere (UT/LS) [*Fromm and Servranckx*, 2003; *Fromm et al.*, 2005]. Due to the coincidence of the fire heating and the extremely high abundance of aerosol particles and trace gases, such as CO and NO_x, in forest fire smoke, pyro-convection is a very efficient mechanism for the vertical transport of these tracers and potentially contributes substantially to their budgets in the UT/LS.

Several studies report observations of smoke gases and aerosol particles in the stratosphere. *Fromm and Servranckx* [2003] analyzed satellite observations of the Chisholm fire plume and showed that it resulted in injection of smoke into the lower stratosphere. The number of such reports from different years suggests that severe pyro-convection with subsequent stratospheric injection is not a singular event but rather a fairly common phenomenon in boreal regions [*Fromm et al.*, 2004, 2000, 2005; *Waibel et al.*, 1999; *Jost et al.*, 2004]. Hence, biomass burning emerges as an additional, previously underestimated source of aerosol and trace gases to the UT/LS region. The residence time of smoke is greatly enhanced at such high altitudes due to the absence of efficient removal processes such as wet deposition.

Smoke aerosol particles scatter and absorb solar radiation and therefore exert a strong effect on the Earth's radiation budget. The radiative forcing significantly depends on the altitude of the aerosol, particularly in the case of absorbing aerosol [*Cook and Highwood*, 2004]. The stratospheric aerosol burden has a substantial influence on climate. It is well established that major volcanic eruptions have resulted in significant surface cooling on timescales of up to two to three years in low latitudes and have also altered atmospheric dynamics leading to mid-latitude winter warming over the northern continents [*Robock*, 2000]. Similar, yet

weaker effects are to be expected from stratospheric layers of biomass burning smoke [*Fromm et al.*, 2004]. The injection of smoke also has the potential to significantly perturb lower stratospheric chemistry. The smoke alters the ozone chemistry through both gas phase processes induced by the injected smoke gases as well as heterogenous processes on the aerosol particles. *Fromm et al.* [2005] report observations of enhanced ozone in a lower stratospheric smoke plume.

Detailed investigations of pyro-convection on the spatial scale of individual events using cloud-resolving models (CRMs) are very important for the study of the vertical and cross-isentropic transport mechanisms responsible for stratospheric injection. *Jost et al.* [2004] reported in-situ observations of smoke, originating from a boreal forest fire, deep in the stratosphere at potential temperatures of 380 to 390 K over Florida in July 2002. They also performed calculations with a Lagrangian transport model based on the European Center for Medium Range Weather Forecasting (ECMWF) reanalysis with a horizontal resolution of 0.5×0.5 degrees. The vertical transport in the model calculation, however, was not strong enough to reproduce the observed altitude of the smoke layer. Similarly, while *Damoah et al.* [2006] were able to reproduce the overall features of the smoke plume, their Lagrangian particle dispersion model simulations underestimated the observed plume height even when a convective transport parameterization was activated.

Atmospheric convection is one of the most complex problems in geophysical fluid dynamics [*Emanuel*, 1994]. The evolution of deep convection depends on the ambient profiles of temperature, humidity and wind shear [e.g. *Houze*, 1993]. Deep convection over land is typically initiated by inhomogeneities at the surface, such as orography, areas of low albedo and heat sources at the ground, or by frontal lifting in synoptic systems. In the case of convection triggered by forest fires, the fire emissions of sensible heat, latent heat in the form of water vapor, and aerosol particles acting as CCN are additional parameters influencing cloud dynamics. We assessed the effects of the parameters most relevant to pyro-convection individually in a series of model simulations. These variables interact in a complex and non-linear way. Due to the complexity of our simulations and computational limitations, it was not, however, possible to perform an exhaustive number of simulations to cover the entire multi-dimensional parameter space.

The sensitivity studies presented here enable us to provide a fundamental understanding of relevant physical processes and to identify the key mechanisms for the development of the extremely vigorous pyro-convection that occurred over the Chisholm fire [*Fromm and Servranckx*, 2003]. In the existing literature, there is not much knowledge about the relative significance of fire heating, moisture re-

lease, aerosol-microphysics interactions, and meteorology for the enhancement of wildfire-induced pyro-convection. For the scenario of large-scale urban fires created from a nuclear burst, *Penner et al.* [1986] concluded from numerical simulations that the amount of smoke deposited in the stratosphere critically depends on the intensity of the heat released, the background stability of the atmosphere, the amount of water vapor in the background atmosphere, and the background wind speeds. In a similar study, *Small and Heikes* [1988] found the sensitivity of the convection to ambient moisture to be particularly significant. This is consistent with evidence that the occurrence of pyroCbs tends to coincide with passing cold fronts, during which the convective instability and humidity of the background atmosphere is high [*Fromm and Servranckx*, 2003; *Fromm et al.*, 2005]. *Potter* [2005] postulated that moisture released by the fire itself can also play an important role in the dynamics of convection induced by wildfires.

Recent observational studies found evidence that microphysical effects of aerosol pollution can significantly enhance the vertical development of convection. *Andreae et al.* [2004] reported in-situ observation of pyro-convection and cumulus convection in smoky conditions in Amazonia which was significantly more vigorous than deep convection in clean conditions. From analysis of satellite data, *Koren et al.* [2005] found strong correlations between aerosol abundance and cloud top pressure for convective clouds over the northern Atlantic, indicating a positive feedback of aerosol pollution and convection dynamics. A modeling study of deep-convective tropical clouds by *Wang* [2005] showed that increasing CCN resulted in stronger convection caused by increased condensation. Such aerosol-cloud interactions, however, critically depend on the specific temperature and humidity profiles [*Graf*, 2004].

The Chisholm fire was located at 54.5° N, 114.5° W in Alberta, Canada and resulted in severe pyro-convection on 28/29 May 2001. It is a particularly well documented case of biomass smoke injection into the stratosphere and therefore is well suited as a case study. In their paper, *Fromm and Servranckx* [2003] were able to establish a direct connection between the observations of the Chisholm pyroCb convection and a smoke layer that was observed in the UT/LS region in the subsequent days. This event gave rise to significantly enhanced lower stratospheric aerosol burden in the northern summer of 2001 [*Fromm and Servranckx*, 2003]. Analysis of remote sensing data from space-borne platforms as well as radar data provide us with a detailed picture of the evolution of this pyroCb event [*Rosenfeld et al.*, 2007]

Whereas in Chapter 3 and Chapter 4 results from the reference simulation are presented and discussed, this Chapter presents sensitivity studies to fire activity

and background meteorology. It is organized as follows. In the next section, the ATHAM model and its setup for the simulation of the Chisholm fire are described. The variability of various parameters is discussed and the sensitivity studies conducted are described in Section 5.3. Results from the sensitivity studies are presented and discussed in Section 5.4. A summary and concluding remarks follow in the last section.

5.2 Model setup

All simulations presented here were performed with the Active Tracer High resolution Atmospheric Model (ATHAM) [*Oberhuber et al.*, 1998; *Graf et al.*, 1999; *Herzog et al.*, 1998]. The dynamic core of ATHAM is based on a centered differences discretization of the governing equations. The tracer advection is formulated in mass-conserving form. For realistic simulation of entrainment of environmental air into the plume, sub-grid scale turbulence is explicitly parameterized using an extended TKE approach with anisotropic representation of horizontal and vertical turbulence [*Herzog et al.*, 2003]. The microphysics is represented using a two-moment scheme with four hydrometeor classes (cloud droplets, rain drops, small ice crystals, graupel) [*Textor et al.*, 2006a,b].

For all simulation runs presented here, the model was set up in the same way as described in Chapter 3.2.2. The fire forcing is assumed to be constant during the time span simulated and represented as a rectangular front of 15 000 m length and 500 m width. The model domain is 85 km in the direction along the fire front and 65 km across, with the upper boundary at 26 000 m. The number of grid points used is 110×85 in the x- and y-directions and 100 in the z-direction. We used a focusing grid with maximum resolution at the fire and its vicinity, where the gradients of tracer concentrations and temperature are largest. Towards the edges of the model domain, the grid spacing is larger. In the horizontal, the minimum grid spacing was set to 100 m perpendicular to the fire front and 500 m along the front. In the vertical, we used two regions of enhanced spatial resolution: the grid spacing was 50 m at the ground and, for more accurate simulation of troposphere-to-stratosphere transport, 150 m at the tropopause. In the mid-troposphere, the maximum vertical spacing was 300 m.

The reference simulation (REF) is identical to the simulation presented in Chapter 3. The fire was assumed to consume $9\,\mathrm{kg\,m^{-2}}$ with a rate of spread of $1.5\,\mathrm{m\,s^{-1}}$. In this simulation run we assumed that 100% of the fire energy goes into the heating of the atmospheric layer over the fire, i.e., radiative losses were assumed to be zero. A fuel moisture value of 40% based on dry fuel mass was assumed.

Table 5.1: Values of fire emissions of sensible heat, moisture, and CCN number used in the experiments studying the sensitivity to fire activity. All quantities are given in per unit fire front length.

Simulation run	Heat 10^6 W m^{-1}	Moisture kg (m s)$^{-1}$	CCN 10^{12} (m s)$^{-1}$
REF	239	12.2	41.8
SH50	119	12.2	41.8
SH25	60	12.2	41.8
loCCN	239	12.2	0
noH2O	239	0	41.8

For the aerosol emissions, we used an emission factor for total particulate matter (TPM) of 17.6 $g_{TPM}\,kg_{fuel}^{-1}$ [*Andreae and Merlet*, 2001] and assumed a volume mean diameter of 0.2 μm, which is consistent with *Reid et al.* [2005]. Based on parcel model studies (Martin Simmel, personal communication), we estimated that 5% of the aerosol particles from the fire become activated as cloud droplets. This results in an effective CCN flux of 2.1×10^5 m^{-1} s^{-1} per unit length of the fire front. Background meteorology was adopted from radiosonde observations that were performed at Edmonton (53.5° N, 114.1° W), about 150 km south of the fire location, at 00:00 UTC, shortly before the time of the blow-up and is likely to closely match the meteorological background condition for the Chisholm pyroCb.

5.3 Sensitivity studies conducted

5.3.1 Fire activity

The combustion of biomass results in enormous emissions of sensible heat, latent heat in the form of water vapor, aerosol particles, and trace gases from forest fires. The emission of sensible heat clearly plays an important role in triggering convection and in adding to the buoyancy of smoky air parcels relative to the ambient air. For given assumptions on the amount of fuel burned, heat of combustion and rate of spread, the head fire intensity, i.e., the combustion energy per unit time and unit length of the fire front, can be readily calculated [*Byram*, 1959]. In the case of the Chisholm fire, these values are documented and discussed in *ASRD* [2001]. Large uncertainties are associated with these values, however. In addition, the fraction of the combustion energy that is lost radiatively without becoming

available for the convection is highly uncertain (cf. Chapter 3 and *Trentmann et al.* [2006]).

In order to assess the role of the fire sensible heat for the Chisholm pyro-convection, the two experiments SH50 and SH25 were conducted for which the sensible heat flux from the fire was reduced to 50 and 25% of the reference value, respectively (Table 5.1).

The combustion of biomass results not only in emission of sensible heat, but also releases water vapor. Moisture is released through the chemical transformation of the carbohydrates (combustion moisture) as well as the evaporation of water that was already contained in the fuel tissue (fuel moisture). According to the stoichiometric equation for the combustion process [*Byram*, 1959], in addition to the fuel moisture, about 0.5 kg of combustion moisture are released per kg of fuel. Due to the large amount of duff burned, we estimated that the effective fuel moisture content was 40%, which yields total water emissions of $0.9\,\mathrm{kg_{H_2O}\,kg_{fuel}^{-1}}$ (cf. Chapter 3). For the investigation of its impact on the pyro-convection, the simulation noH2O was set up neglecting water vapor emissions from the fire.

Since aerosol particles act as cloud condensation nuclei (CCN), the cloud microphysics is strongly affected by their abundance. It is well established that increased availability of condensation nuclei in polluted clouds results in a much larger number of cloud droplets being activated compared to clean clouds, giving rise to the indirect aerosol effects [*Lohmann and Feichter*, 2005]. Droplets compete for a given amount of water vapor available, therefore the droplet size distribution in polluted clouds is shifted to much smaller sizes. As various microphysical processes are strongly sensitive to the droplet size, the change in size spectrum induced by pollution with aerosol significantly alters the cloud properties and precipitation efficiency.

For deep-convective cloud systems, aerosol-microphysics interactions can have a strong impact on the convection dynamics. As proposed by *Rosenfeld* [2000], pollution from aerosols can result in vertically delayed onset or even complete suppression of precipitation through warm rain formation. On the other hand, if the convection is sufficiently strong, mixed phase microphysics can lead to stronger precipitation higher up [*Andreae et al.*, 2004]. The smoke emitted by the fire contains large numbers of aerosol particles acting as CCN. The co-existence of strong deep convection and extreme aerosol concentration makes pyro-clouds well-suited objects for the study of aerosol-microphysics interactions and their impact on convection dynamics. At the same time, pyro-clouds are peculiar in their dynamic structure because of the extreme vigor induced by the heating from the fire. There is also a strong influence of the dynamics, particularly the updraft velocities, on

cloud microphysics and precipitation formation. In smoky environments and pyro-convection in the Amazon region, *Andreae et al.* [2004] observed strongly delayed onset of precipitation compared to clouds in clean conditions, which resulted in more vigorous convection once the glaciation level was reached.

In the experiment loCCN, we tested the sensitivity of the Chisholm pyroCb to the enhanced availability of CCN from the fire by performing a sensitivity study in which we assumed that the aerosol particles emitted by the fires are inactive as CCN. In this scenario, the formation of clouds was based on the assumption of a CCN concentration of $200\,\mathrm{cm}^{-3}$, a value representative of clean conditions in remote continental areas [*Pruppacher and Klett*, 1997].

5.3.2 Background meteorology

The development of extremely strong pyroCbs in boreal regions is almost always observed to coincide with the passage of synoptic cold fronts [*Fromm et al.*, 2000, 2005; *Fromm and Servranckx*, 2003]. Typically, large pyroCb events are favored when hot and dry air masses associated with a high pressure system are replaced by colder, less stable air masses.

There are clear indications for a connection between a passing cold front and the intensification of the convection induced by the Chisholm fire. The development of the Chisholm pyroCb was captured by remote sensing from several platforms [*Rosenfeld et al.*, 2007]. Radar observations show a convective rain band propagating through the fire region from the southwest, a typical signature of a cold front. Whereas the fire convection was moderate and fanning before the passage of the front, it intensified into severe pyro-convection at 02:00 UTC, exactly upon the arrival of the rain band. Similarly, observations from the Advanced Very-High Resolution Radiometer (AVHRR) show that the blow-up occurred during the passage of the cloud band associated with the cold front [*Fromm and Servranckx*, 2003]. As measured by the automated weather stations in the Chisholm region, temperature dropped by more than 10 K between 1700 and 2000 LT (23:00–02:00 UTC) on 28/29 May [*ASRD*, 2001], just before the pyro-convection was observed to peak by the radar observations. This temperature decrease occurred before sunset and is much greater than the typical diurnal variation in the late afternoon.

Meteorological conditions affect deep pyro-convection in several ways. As shown for the reference simulation (Chapter 3 and *Trentmann et al.* [2006]), the energy budget of the Chisholm pyroCb is dominated by the release of latent heat from condensing water vapor. Most of this water vapor, however, is entrained from the ambient atmosphere, whereas the contribution of the water vapor released by the fire accounts for only a small fraction of less than 10% (cf. Chapters 3 and 6).

This underlines the dominant role of atmospheric conditions, especially the convective instability, humidity and wind shear for the evolution of pyro-convection. Wind speed and wind shear affect turbulent mixing and hence the amount of entrainment at various altitude levels. For the case of the Chisholm pyroCb, the amount of air entrained from intermediate tropospheric altitude levels is comparable to the entrainment within the boundary layer (Chapter 3). This has important implications for the sensitivity of the convection to the meteorological conditions, i.e., temperature, humidity and wind field in the middle troposphere.

Since the fire front is approximately linear, the orientation of the low level wind field relative to the fire front plays an important role. The passing cold front resulted in a change of the wind field, with surface wind gusts from changing directions [*ASRD*, 2001]. During the passage of the cold front, the surface wind was oriented almost parallel to the fire front. In this configuration, the air parcels were advected along the fire front, exposing them to the heating of the fire for a maximum period of time while minimizing the entrainment of ambient air.

Changing atmospheric conditions associated with frontal structures also have a strong influence on fire behaviour. For the case of the Mack Lake Fire, *Zimet et al.* [2007] show that strong subsidence associated with the replacement of an upper level ridge by a trough resulted in favorable fire weather conditions. Since we did not explicitly represent the feedback of the atmospheric conditions on the fire behavior in ATHAM, the assessment of the contribution of the atmosphere-fire-feedback to the sensitivity to background meteorology is not considered in this study. For our simulations, the fire activity as well as fluxes of sensible heat, moisture and aerosol particles were prescribed based on the observed fire activity as documented in *ASRD* [2001].

The meteorological situation at the time of the blowup is depicted in Figure 5.1. For the reference simulation, we used the sounding from RAOB station 71 119 (Edmonton, 150 km south of the fire) launched at 00:00 UTC.

In a set of sensitivity experiments, we assessed the influence of changing background meteorology on the fire convection. Since there were not a sufficient number of observations available, we relied on ECMWF reanalysis data for this purpose. We chose three meteorological profiles representative of pre-frontal (simulation PRE), frontal (FRONT), and post-frontal (POST) conditions from different locations in the operational ECMWF reanalysis for 29 May 2001, 00:00 UTC (Figure 1). For these three experiments, all parameters describing the fire forcing, namely the geometry of the forcing and the release of sensible heat, water vapor, as well as aerosol particles were set equal to those in REF.

The vertical profiles of temperature, dew point temperature, and wind vectors

Table 5.2: Background meteorological profiles used for the experiments studying the sensitivity to background meteorology. CAPE, water vapor column (WVC) and equivalent potential temperature θ_e in the boundary layer are given for comparison between the three simulations based on ECMWF meteorology and the reference simulation.

Simulation run	Location	CAPE [J kg^{-1}]	WVC [kg m^{-2}]	θ_e [K]
PRE	53° N, 111° W	40	17.8	319
FRONT	54° N, 116° W	1170	23.4	322
POST	56° N, 117° W	30	21.5	317
REF	53.5° N, 114° W	131	22.0	321

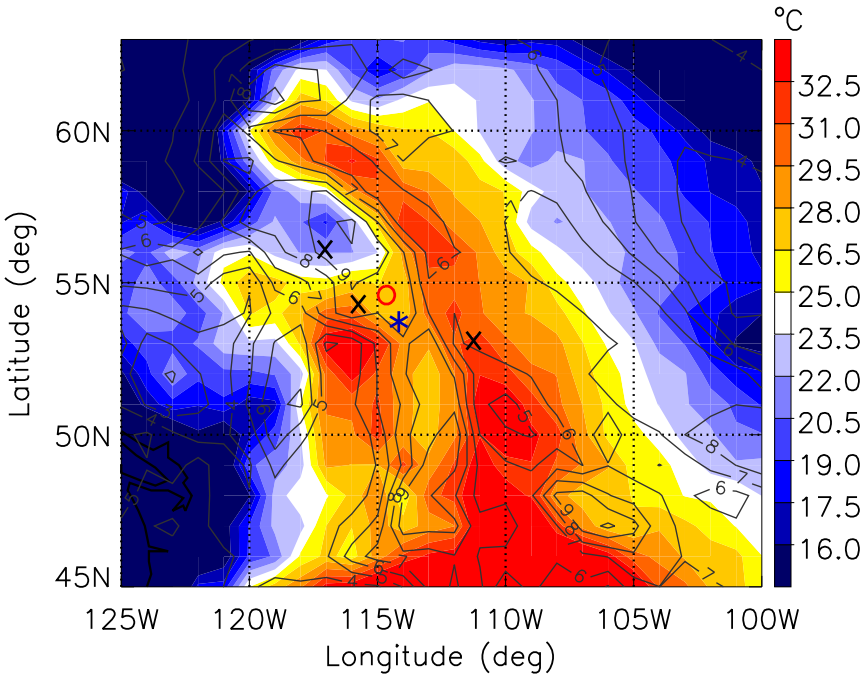

Figure 5.1: Surface fields of potential temperature (color shading) and specific humidity (contour lines) from ECMWF operational reanalysis for southwestern Canada. The red circle indicates the fire location, the blue asterisk is at the position where the radiosonde was launched (53.5° N, 114° W), and black crosses indicate the locations from which profiles representative of pre-frontal (53° N, 111° W), frontal (54° N, 116° W) and post-frontal (56° N, 117° W) conditions were adopted.

used are depicted in skew T-log(p) diagrams in Figures 5.2a–c. For comparison, the radiosonde sounding from 53.5° N, 114.1° W at 00:00 UTC, which was used for the reference simulation, is shown in Figure 5.2d. Table 5.2 gives values for

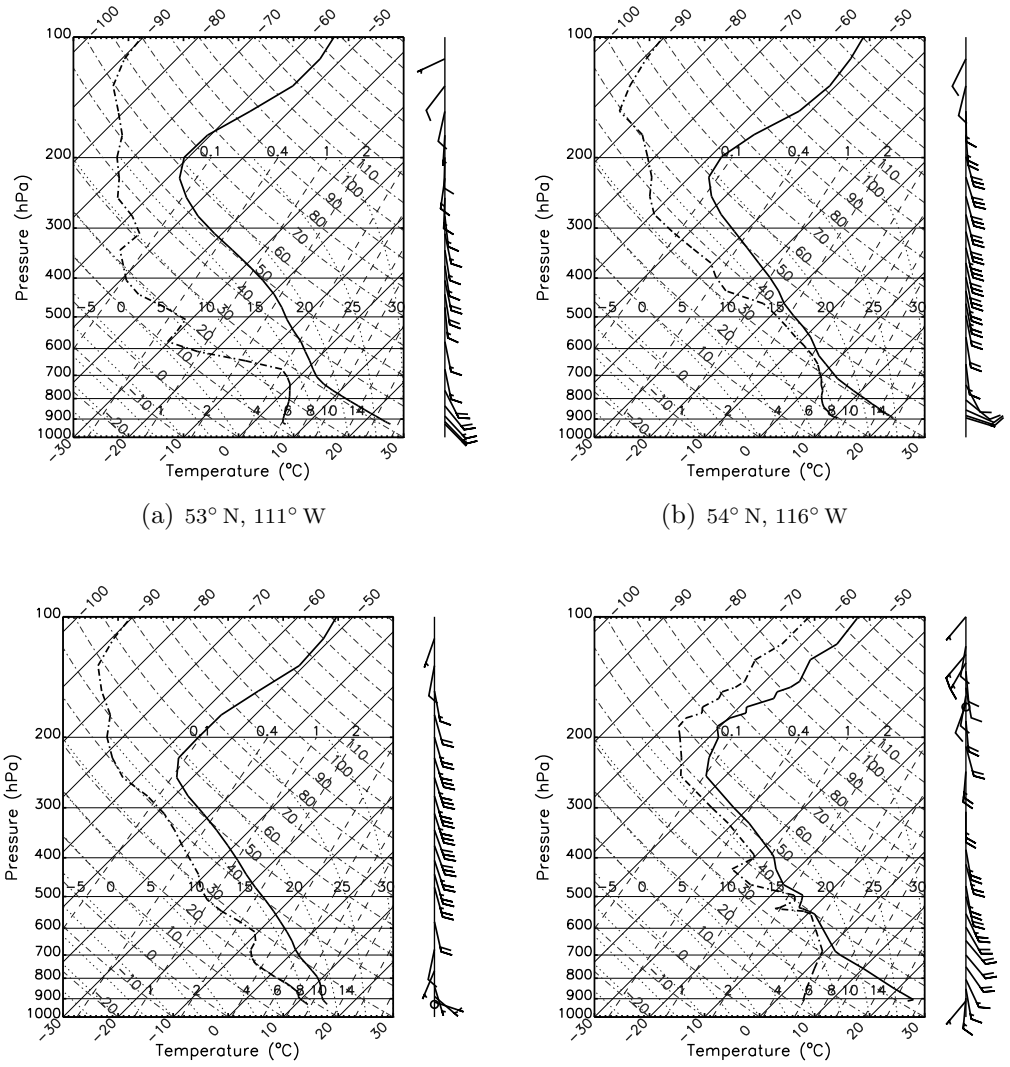

(a) 53° N, 111° W

(b) 54° N, 116° W

(c) 56° N, 117° W

(d) Observation

Figure 5.2: Profiles of temperature (dash-dotted) and dew point temperature profiles (solid) from ECMWF reanalysis for (a) pre-frontal, (b) frontal, (c) post-frontal conditions as well as (d) from radiosonde observations at 53.5° N, 114° W in skew T- $\log p$ representation. Arrows indicate vertical wind profiles with every full barb corresponding to 10 m s^{-1}. Thin skewed solid lines represent lines of constant temperature. Water vapor mixing ratios are given by the thin dashed lines. Dry adiabats are plotted as thin dash-dotted lines. Pseudo-adiabats are represented as thin dotted lines.

convective available potential energy (CAPE), water vapor column, and equivalent potential temperature for the four profiles.

The pre-frontal profile (53° N, 111° W) is characterized by rather warm temperatures throughout the lower and middle troposphere with low relative humidities around 30–40% at low levels and very dry air masses in the middle and upper troposphere above 600 hPa. In the boundary layer, the stratification is approximately neutral, and the temperature gradient is close to the saturated adiabatic lapse rate in the free troposphere. The low level wind speed is about $17\,\mathrm{m\,s^{-1}}$ from southeasterly directions.

For the frontal profile (54° N, 116° W), the boundary layer is still warm, whereas the free troposphere is already influenced by colder air masses. The air is rather moist throughout the lower and middle troposphere up to about 400 hPa. At this level, the wind continues to blow from southeasterly directions at slightly lower wind speeds than in the pre-frontal profile. At higher levels, in contrast, the upper level trough gives rise to strong southerly winds of around $30\,\mathrm{m\,s^{-1}}$.

The post-frontal profile (56° W, 117° N) is characterized by low level temperatures that are significantly cooler than in the pre-frontal and frontal profiles. The relative humidity is high in the boundary layer, but decreases strongly in the free troposphere. The atmosphere is stably stratified in the lower troposphere and the temperature decreases with an approximately moist-adiabatic lapse rate in the free troposphere. Whereas low level winds are rather weak, there is a strongly pronounced upper level jet blowing from southerly directions similar to the frontal profile.

Due to the high humidity and warm temperatures, the equivalent potential temperature in the boundary layer is greatest for frontal conditions (Table 5.2). Using parcel theory, its convective instability can be quantified in terms of the convective available potential energy (CAPE) [*Emanuel*, 1994]. It is greatest for the frontal profile with CAPE=$1170\,\mathrm{J\,kg^{-1}}$. For both the pre- and post-frontal profiles, the convective instability is rather low, with CAPE values of 40 and $30\,\mathrm{J\,kg^{-1}}$, respectively.

The radiosonde profile features a deep boundary layer similar to PRE with warm temperatures and 30% relative humidity at the surface. Due to the low humidity levels close to the ground, its nominal CAPE value is much lower than the one obtained for REF. Above 700 hPa, by contrast, the sounding is moist with humidities close to saturation. There is substantial entrainment of air into the pyroCb at intermediate levels, therefore the humidity there strongly influences the convection, which is not reflected in the calculation of CAPE. Upper level winds are significantly weaker than in FRONT and POST. Surface winds blow from the

Table 5.3: Numerical values of outflow height z_{out}, maximum penetration height z_{max}, mean updraft velocity $\overline{w}$, integrated buoyancy IB, total hydrometeor mass m_{ht}, and stratospheric aerosol injection m_{as} obtained for simulation runs with different fire activity after 40 min integration time. See text for definition of these quantities.

Simulation run	z_{out} [km]	z_{max} [km]	w_{max} [m s^{-1}]	$\overline{w}$ [m s^{-1}]	IB [kJ kg^{-1}]	m_{ht} [10^9 kg]	m_{as} [10^3 kg]
REF	10.6	12.2	38.0	18.1	2.07	9.7	710
SH50	8.1	10.7	29.0	11.8	1.11	6.1	1.4
SH25	7.0	9.5	23.2	8.7	0.61	2.9	0
noH20	10.4	11.9	37.5	17.1	2.02	9.0	430
loCCN	10.6	12.3	38.0	19.0	2.13	9.8	890

south and veer to southeasterly directions in the free troposphere.

5.4 Results

5.4.1 Definitions and analysis methods

We used different parameters and analysis methods to characterize the results from the various numerical experiments. The relevant definitions are introduced in the following. The resulting numerical values are summarized in Tables 5.3 and 5.4. Figures 5.3 and 5.8 show 3-D visualizations of the modeled smoke plumes as 100 μg m^{-3} aerosol iso-surfaces with potential temperature as color shading.

Stratospheric penetration and the height to which the smoke is transported were assessed by means of the vertical aerosol distribution as a function of geometrical height (Figure 5.4a) and potential temperature (Figure 5.4b). The outflow height z_{out} was defined as the geometrical level of the maximum of the vertical aerosol profile. We also defined the maximum penetration height z_{max} as the level below which 99% of the aerosol mass is located. All altitude levels are given as height above sea level. The ground level was 695 m, 940 m and 640 m, for PRE, FRONT and POST, respectively, and 770 m for REF.

In the absence of diabatic processes (radiation, microphysical processes, turbulent mixing), long range transport of air parcels in the lower stratosphere occurs along isentropes. The aerosol mass distribution as a function of potential temperature (Figure 5.4b) is therefore useful for the assessment of troposphere-to-stratosphere transport. Due to the large gradients of the potential temperature

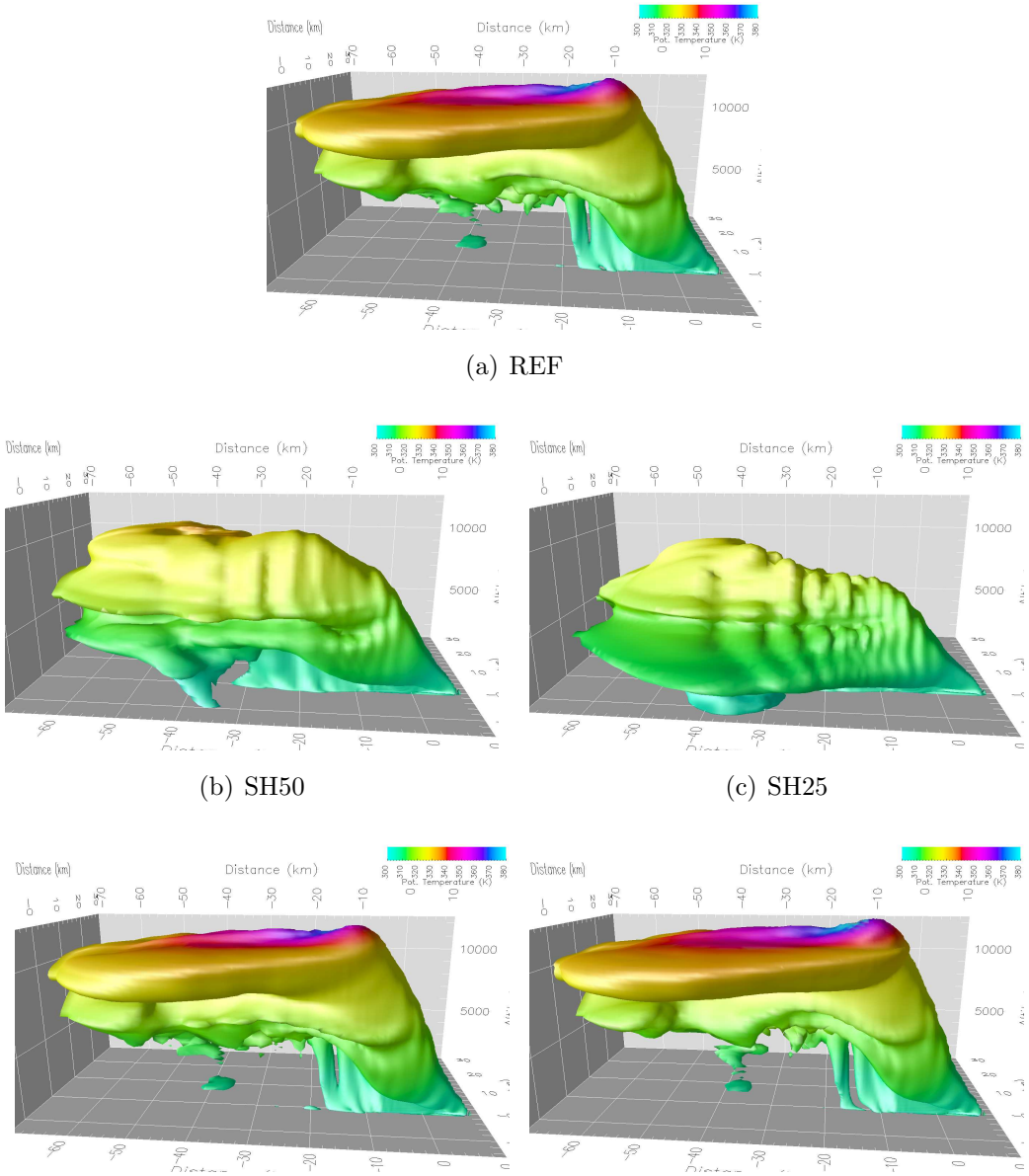

(a) REF

(b) SH50

(c) SH25

(d) noH20

(e) loCCN

Figure 5.3: 100 μg m^{-3} iso-surface of aerosol concentration after 40 min integration time for (a) the reference simulation, (b) the sensitivity studies SH50, (c) SH25, (d) noH2O, and (e) loCCN. The color shading indicates potential temperature.

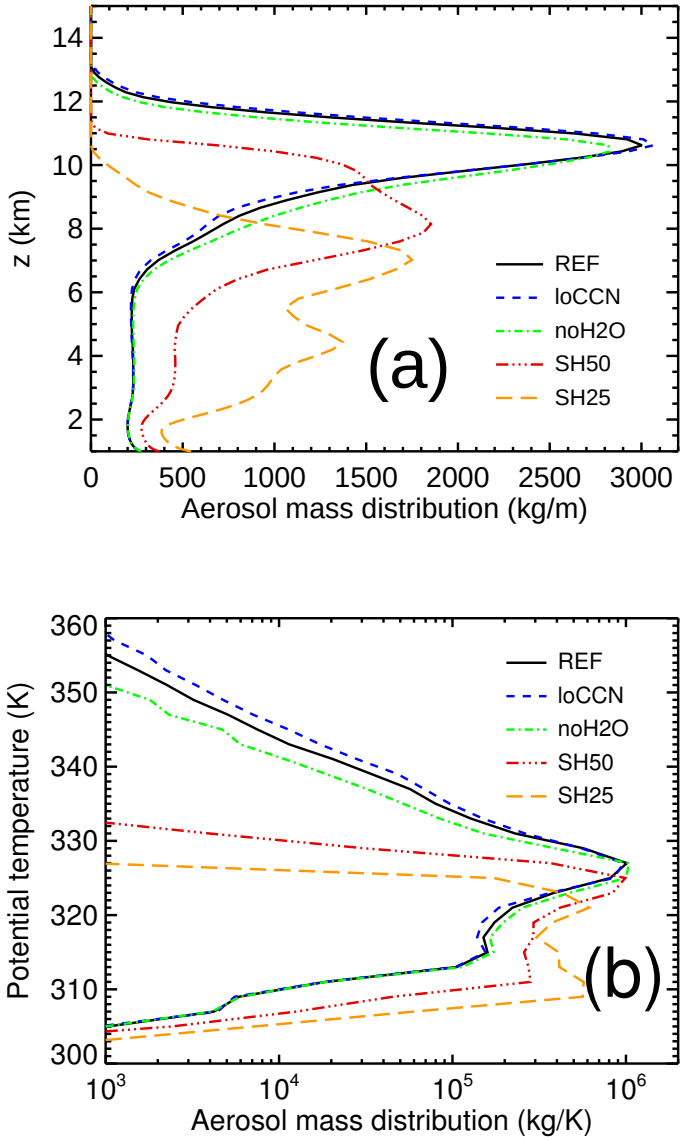

Figure 5.4: Vertical distribution of aerosol mass as a function of altitude (a) and as a function of potential temperature (b) after 40 min integration time. The 2 PVU tropopause is located at 332 K/11.0 km.

at the tropopause and above, this region is better resolved in this representation compared to the lower troposphere. In order to better represent the low yet significant aerosol mass above the tropopause we used a logarithmic scale. We masked out the region of high temperatures directly above the fire by only considering aerosol above 5 km.

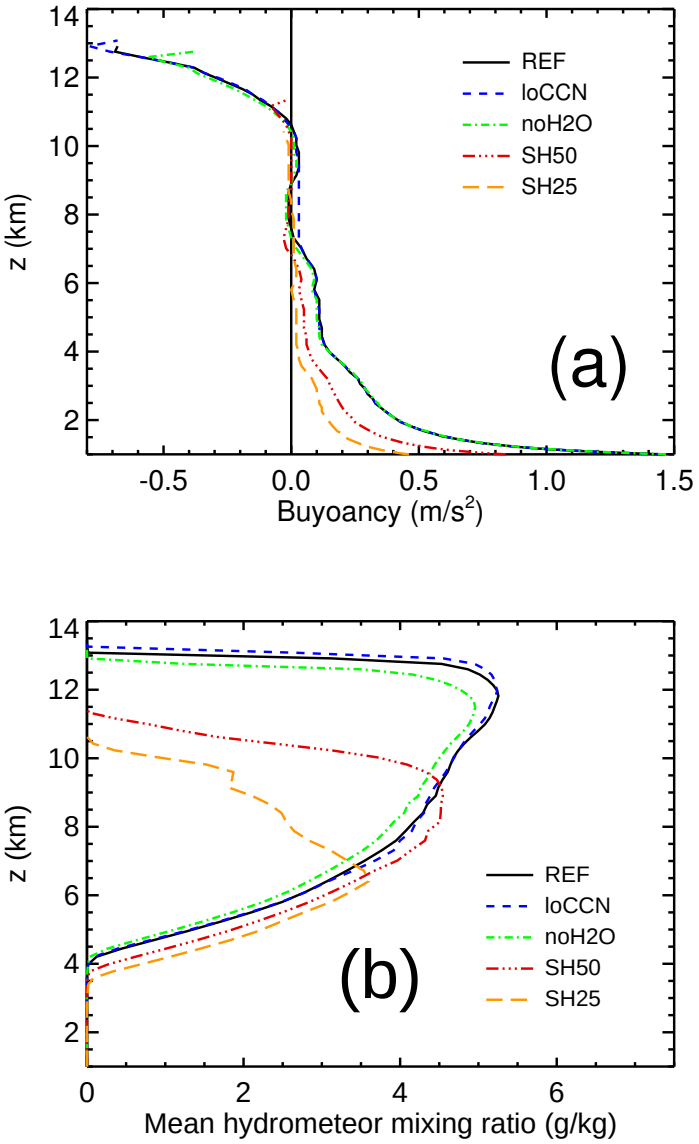

Figure 5.5: Vertical profiles of (a) mean buoyancy $\overline{b}$ and (b) mean hydrometeor content in the pyroCb's updraft region.

The dynamical tropopause (PV=2 PVU) over the Chisholm region was located at a potential temperature of about 332 K at 11 km altitude. The stratospheric aerosol injection was estimated as total mass, m_{as}, above this potential temperature level. The tropopause level was similar for the PRE, FRONT, and POST profiles, hence for all simulation runs the same threshold value of 332 K was assumed for the estimation of aerosol injection into the stratosphere. Whereas m_{as}

is very useful for comparing the different simulations, its absolute value should be treated with caution. Due to the large vertical gradient in the aerosol concentration near the tropopause, it is extremely sensitive to the tropopause definition and the simulation time. Since our simulations did not account for removal by scavenging of interstitial aerosol particles, the numerical value of m_{as} can be considered an estimate of the upper limit of aerosol mass injected into the stratosphere.

We also used different parameters to characterize the vigor and the energy budget of the pyro-convection for the various cases. The maximum vertical velocity $w_{\max}$ is located close to the ground and mostly influenced by the fire forcing. Therefore, we additionally defined the mean updraft velocity as a parameter that is more characteristic of the convection throughout the entire vertical column of the cloud:

$$\overline{w} = \frac{1}{\int c_a dV} \int w c_a dV. \tag{5.1}$$

In order to represent the conditions in the updraft region of the pyro-cloud, the integration was performed over all grid boxes with more than $0.05\,\mathrm{g\,kg^{-1}}$ hydrometeor content and vertical velocity $w{\geq}5\,\mathrm{m\,s^{-1}}$, and the aerosol mass concentration c_a was used as a weight function.

For the characterization of the pyroCb's updraft region, we defined the mean vertical profile of any quantity Q as

$$\overline{Q}(z) = \frac{\int Q(x,y,z) w(x,y,z) c_a(x,y,z)\, dxdy}{\int w c_a dxdy}, \tag{5.2}$$

where the vertical aerosol flux wc_a was used as a weight function and the integration was performed for $w{>}0$.

Vertical profiles of the buoyancy and the mean hydrometeor mixing ratio are depicted in Figures 5.5 and 5.10. The buoyancy b was calculated as

$$b(x,y,z) = g\, \frac{\rho(x,y,z) - \rho_e(z)}{\rho_e(z)}, \tag{5.3}$$

where g is the acceleration of gravity and the in situ density $\rho(x,y,z)$ and environmental density $\rho_e(z)$ were determined with consideration of the density effects of water vapor and hydrometeor content.

The vertical mean buoyancy $\overline{b}$ can be readily determined according to Eq. (5.2). The integrated buoyancy IB can then be defined as

$$IB = \int_{Z_0}^{Z_{LNB}} \overline{b}(z) dz, \tag{5.4}$$

where the integration is performed from ground level Z_0 to the level of neutral buoyancy Z_{LNB} with $\overline{b}(Z_{\mathrm{LNB}})$=0. IB indicates the amount of potential energy a

smoky air parcel extracts from its buoyancy traveling from the fire to its LNB. It is closely related to CAPE. Whereas the CAPE concept considers the energy of an air parcel traveling from the boundary layer to its LNB and neglects effects of mixing, the IB concept calculates the effective energy for the vertical column under full consideration of entrainment, and also accounts for the effects of additional heat sources such as the fire forcing. In contrast to CAPE, however, detailed information about vertical profiles of temperature, moisture and hydrometeor loading within the convection is required.

The results obtained for the reference simulation REF are presented in detail in Chapter 3 and *Trentmann et al.* [2006]. In the following, the results of the sensitivity experiments are compared with those of REF.

5.4.2 Fire release of sensible heat

From the results obtained for SH50 and SH25, the sensitivity studies with the sensible heat release from the fire reduced to 50 and 25% of the original value, respectively, a strong dependence of the cloud vertical plume development on the fire heating is clearly evident (Figures 5.3 and 5.4). In the reference simulation REF most of the smoke outflow from the pyroCb occurs in the tropopause region and slightly below. Stratospheric penetration can be inferred from the high potential temperatures at the plume top, with red, purple and blue colors in Figure 5.3a indicating potential temperatures above ∼335 K. The plume exhibits a region where the cloud-aerosol mixture overshoots beyond the level of the anvil. Near the overshoot, the plume reaches maximum potential temperatures in excess of 350 K. Satellite observations of this "warm core" were also reported by *Fromm and Servranckx* [2003]. By contrast, for the SH50 simulation and to a yet larger extent for SH25, the vertical development of the plume is much weaker with a much less established updraft region (Figure 5.3b, c). Gravity-wave-like features are apparent, however there is no distinct overshoot nor any warm core region. In both simulations, the plumes do not reach beyond the tropopause and remain at tropospheric potential temperature and altitude levels.

For the simulations with reduced sensible heat release, the vertical distribution of aerosol mass is more diffuse and strongly shifted towards lower altitudes (Figure 5.4a), with outflow heights at 8.1 km for SH50 and 7.0 km for SH25, compared to 10.6 km for REF. REF had a maximum penetration height $z_{\max}$=12.2 km, whereas SH50 and SH25 only reached to $z_{\max}$=10.7 km and $z_{\max}$=9.5 km, respectively (Table 5.3).

In Figure 5.4b, the difference between SH25, SH50 and REF is even more evident than in Figure 5.4a. In REF, 7.1×10^5 kg of aerosol mass, a minor yet

significant fraction (7%) of the total 8.9×10^6 kg of aerosol released by the fire, is injected above the tropopause after 40 min integration time. Both the SH50 and the SH25 plumes, on the other hand, are not able to overcome the tropopause mixing barrier. The SH50 plume features large amounts of aerosol mass in the upper troposphere with the maximum of the distribution about 5 K below the tropopause, however there is almost no aerosol above 332 K (Figure 5.4b).

Both the $\overline{w}$ and $w_{\max}$ strongly depend on the amount of sensible heat released by the fire: $\overline{w}$ after 40 min integration time drops from 18.1 m/s for REF to 11.8 m/s for SH50 and 8.7 m/s for SH25, with a similar decrease in $w_{\max}$ (5.3). IB was found to be almost linearly proportional to the released sensible heat: Whereas REF resulted in a value of 2070 J/kg, IB was reduced to 1110 J/kg for SH50 and 610 J/kg for SH25.

Also the hydrometeor formation is very sensitive to the sensible heat forcing by the fire. After 40 min, 9.7×10^9 kg of hydrometeor mass was formed in REF, significantly more than the 6.1×10^9 kg and 2.9×10^9 kg obtained for SH50 and SH25, respectively. The vertical profiles of hydrometeor mixing ratios (Figure 5.5b) show that particularly at higher levels much less water is condensed for SH50 and SH25, because the pyroCbs do not reach as high and become diluted at a much lower level. Hence, the higher the release of sensible heat by the fire, the more efficient is the pyroCb at accessing the latent heat available from the background and fire moisture. Considering that the latent heat from the condensation of hydrometeors contributes much more to the potential temperature gain of air parcels in the pyroCb than the fire energy (cf. Chapter 3), this positive feedback is an important aspect for the explanation of the invigoration of the pyro-convection due to fire heating.

5.4.3 Fire release of moisture

In contrast to the sensible heat, the release of latent heat by the fire was found to be of rather low significance for the evolution of the Chisholm pyroCb. The 3-D structure of the plume obtained for noH2O, the simulation without any moisture release from the fire, is similar to that obtained for REF (Figure 5.3a, d). The differences in IB, maximum and mean vertical updraft speed are also rather small (Table 5.3). The total hydrometeor mass for noH2O only decreased by 8% compared to REF. This is consistent with the result from *Trentmann et al.* [2006] and Chapter 3, where it was reported that the fire moisture only accounts for less than 5–10% of the pyro-cloud's water budget, whereas most of the humidity and condensed water within the cloud stems from entrained environmental air. The low contribution of the fire moisture to cloud water and convection dynam-

ics found here does not support the hypothesis from *Potter* [2005], who stated that it constituted a major portion of the cloud water and significantly influenced convection.

Considering the vertical aerosol mass distribution, we found that the outflow level z_{out} of the pyro-cloud and the maximum penetration height z_{max} are shifted by only 0.2 and 0.3 km towards lower altitudes for noH2O compared to REF (Figure 5.4a). Due to the lack of latent heat released from the fire, however, the aerosol distribution as a function of potential temperature (Figure 5.4b) exhibits significantly lower aerosol mass at potential temperatures above the peak outflow level. Consequently, the total aerosol mass above 332 K is 4.3×10^5 kg for noH20, i.e., 35% lower than for REF.

5.4.4 Sensitivity to CCN emissions

For the loCCN simulation, the sensitivity study assuming that the fire aerosol particles are inactive as CCN, we found rather small effects of the aerosol burden on the dynamics. In contrast to results from observational studies of pyro-clouds in the Amazon [*Andreae et al.*, 2004], our results suggest that the vertical development of the Chisholm pyroCb would have been even slightly more vigorous without the fire aerosol. As depicted in Figure 5.3e, the 3-D structure of the smoke plume is very similar to the one obtained for REF, albeit with a slightly higher overshoot and somewhat increased potential temperatures in the warm core region. The vertical aerosol mass distribution is also almost equal to the result for REF, but features a maximum penetration height z_{max} that is about 100 m higher than that of REF (Figure 5.4a). Again, the differences between loCCN and REF are more pronounced in the distribution of aerosol mass as a function of potential temperature. As shown in Figure 5.4b, there is significantly more aerosol mass in the distribution's upper tail at high potential temperatures. We found an aerosol mass of 8.9×10^5 kg injected above the 332 K tropopause level for loCCN, substantially more than the 7.1×10^5 kg found for REF.

The other parameters describing the dynamic evolution of the pyroCb also show that the omission of aerosol effects results in marginally stronger updraft dynamics. Both the mean updraft velocity $\overline{w}$ and the maximum updraft w_{max} are slightly larger than in REF (Table 5.3). Also, IB obtained for loCCN is 2130 J kg^{-1}, about 40 J kg^{-1} more than in REF.

In contrast to the dynamics, the cloud microphysics is strongly impacted by the fire aerosol. As expected, the size of the hydrometeors in the reference study is much smaller than in loCCN (Figure 5.6). The hydrometeors of the small classes (cloud droplets and ice crystals) are most abundant in the updraft region above the

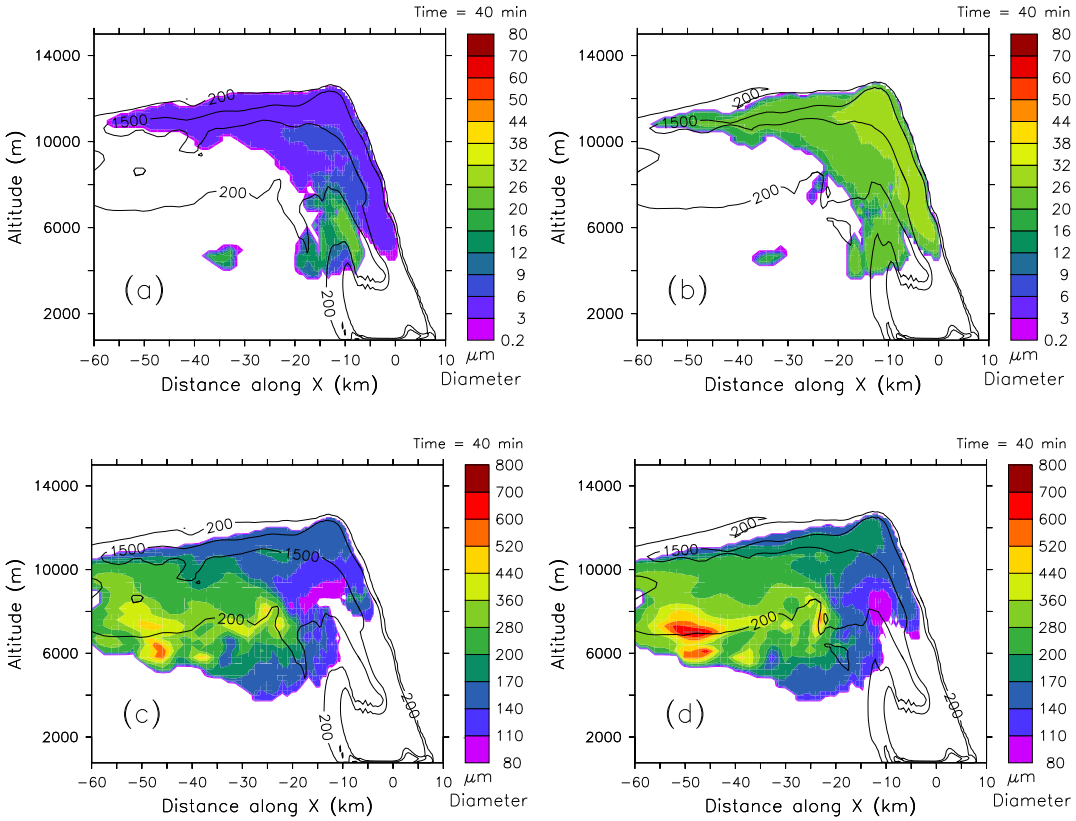

Figure 5.6: Sensitivity of hydrometeor volume mean diameter (VMD) to CCN abundance. Diameters are depicted for (a) small size classes (cloud droplets and ice crystals) in REF, (b) small size classes in loCCN, (c) large size classes (rain drops and graupel) in REF, (d) large size class in loCCN. Contour lines give aerosol concentration in μg m^{-3}.

fire and the upper part of the anvil. For REF their volume mean diameters (VMD) are smaller than 10 μm throughout this region, with the exception of cloud areas outside of the smoke plume or regions greatly diluted with ambient air masses (Figure 5.6a). For droplets of this size, autoconversion, i.e., formation of larger drops as a result of collision and coalescence among small droplets, is inefficient, hence warm rain formation is strongly suppressed. For loCCN, on the other hand, the VMD of the cloud droplets and ice crystals are 20–30 μm (Figure 5.6b), a size where coagulation of droplets becomes active [*Pruppacher and Klett*, 1997]. For the large hydrometeors, however, the difference between REF and loCCN is somewhat less pronounced. This size class is dominated by graupel throughout the anvil. For loCCN, the VMD of graupel at the top of the updraft region is almost 200 μm. In the anvil, the graupel grows to a VMD of up to 400–700 μm. For REF, the VMD of the graupel at the top of the updraft region is about 150 μm

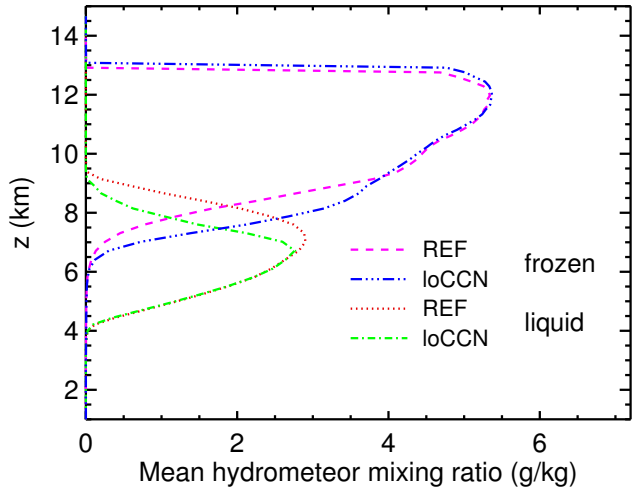

Figure 5.7: Mean content of liquid and frozen hydrometeors for REF and loCCN.

(Figure 5.6a). Its growth is somewhat delayed further downwind compared to loCCN with VMD of about 300–500 μm in the lower part of the anvil, which is dominated by sedimenting graupel.

Our results show that there is no precipitation formation within the updraft region in both the reference case and the case without "CCN-pollution". At a mean vertical velocity of some 17 m s^{-1}, air parcels are traveling from cloud base at 4000 m to the outflow level at 11 000 m in about 7 min, which is insufficient for the development of precipitation even in clean conditions. Hydrometeors large enough to settle under gravity and precipitate are only developing outside the updraft, downwind of the fire and the updraft. This is consistent with the finding that, even though the Chisholm pyroCb was very large and strong, almost no precipitation was recorded at the ground near the fire location [*ASRD*, 2001]. Also, in either case, all the cloud water reaches glaciation, hence the amount of latent heat of freezing released is equal for both simulations. For the small droplet sizes characteristic of polluted clouds, however, freezing is greatly delayed [*Rosenfeld and Woodley*, 2000]. Immersion freezing can be described by the stochastic hypothesis [*Bigg*, 1953]. According to this theory, which is implemented in ATHAM, the freezing probability is proportional to the droplet mass. Consequently, the glaciation level for the smaller droplets in REF is much higher than for the bigger ones in loCCN. In fact, for REF most of the droplets do not freeze until they reach the level of homogeneous freezing of about −39°C at approx. 9 km.

Figure 5.7 depicts the mean liquid and frozen hydrometeor contents for REF and loCCN, which were calculated according to Eq. (5.2), i.e., by using the upward

Table 5.4: Numerical values of outflow height z_o, maximum penetration height $z_{\max}$, mean updraft velocity $\overline{w}$, integrated buoyancy IB, total hydrometeor mass m_{ht}, and stratospheric aerosol injection m_{as} obtained for simulation runs with different meteorological setups after 30 min integration time.

Simulation run	z_{out} [km]	z_{max} [km]	w_{max} [m s^{-1}]	$\overline{w}$ [m s^{-1}]	IB [kJ kg^{-1}]	m_{ht} [10^9 kg]	m_{as} [10^3 kg]
PRE	6.0	10.8	41.6	16.8	1.97	2.5	12
FRONT	10.2	11.8	40.5	17.2	2.29	6.2	350
POST	6.6	9.7	41.2	15.3	1.86	3.5	2.3
REF	10.6	12.1	38.2	16.8	2.04	6.4	300

aerosol flux as a weight function. It is found that freezing in REF is shifted by about 1 km to higher altitudes compared to loCCN. The lower freezing level of loCCN explains its slightly stronger vertical development: The earlier release of the latent heat of freezing and consequent increase of buoyancy results in higher updraft velocities and stronger overshooting. This is clearly evident from the vertical profiles of the mean buoyancy (Figure 5.5a). The profiles for REF and loCCN are equal throughout almost the entire troposphere. Between 7 and 9 km, however, air parcels in REF are approximately neutrally buoyant, whereas those in loCCN remain significantly positively buoyant. This matches exactly the altitude range of the delayed glaciation.

5.4.5 Sensitivity to background meteorology

3-D visualizations of the aerosol plumes simulated for different meteorological conditions after a simulation time of 30 min are shown in Figure 5.8. Because of stronger upper level winds of the ECMWF profiles, the plumes reached the boundaries of the model domain earlier than in the simulations with the radiosonde profiles. Therefore we had to limit the simulations to a 30 min integration time. The aerosol iso-surfaces for PRE, FRONT and POST, the three experiments with ECMWF background profiles, are distinctly different from each other, and also differ from the one obtained for the reference simulation, for which the meteorological profiles from radiosonde observations were used.

For PRE, the experiment conducted with pre-frontal meteorological background conditions, the plume overshoots to levels close to the tropopause, however most of the aerosol remains in the mid-troposphere. The upper level winds are weaker than those in FRONT and POST, therefore the plume is more compact and less

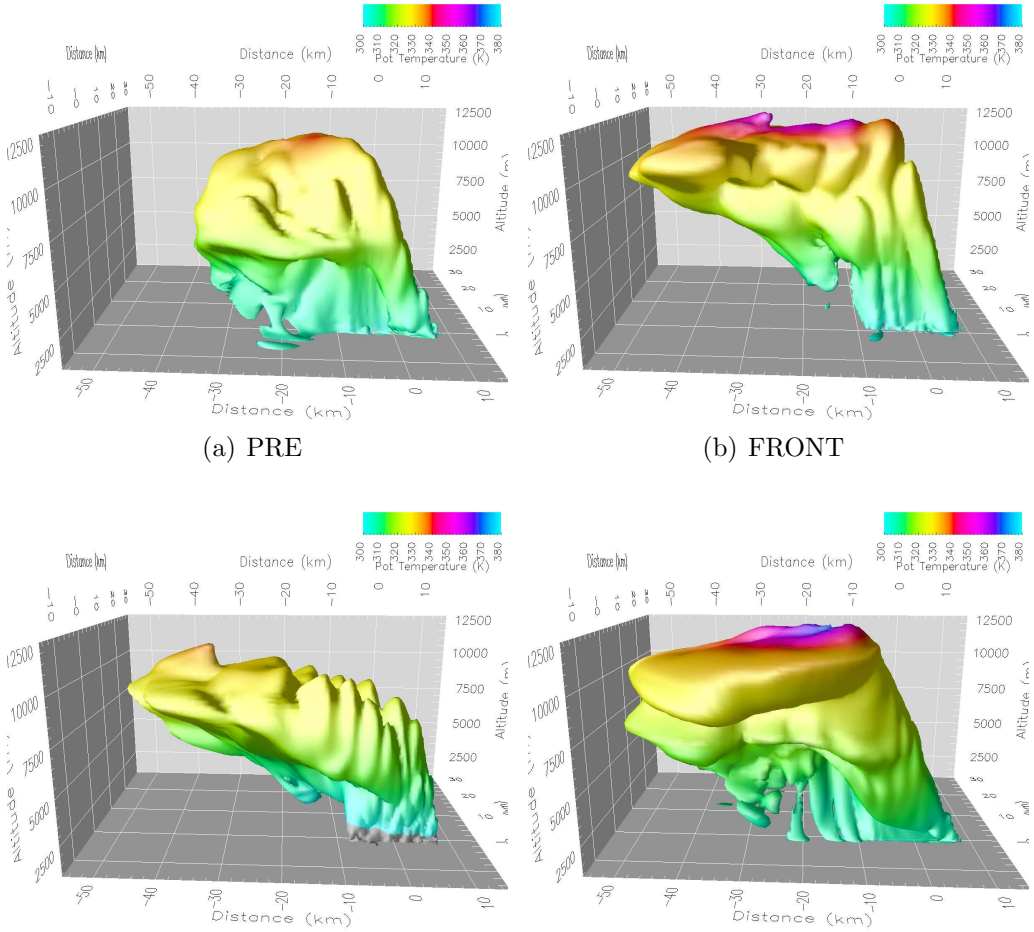

(a) PRE (b) FRONT

(c) POST (d) REF

Figure 5.8: 100 μg m^{-3} iso-surface of aerosol concentration for three simulations (a) PRE, (b) FRONT, (c) POST with different ECMWF background meteorology and (d) the baseline simulation REF after 30 min integration time.

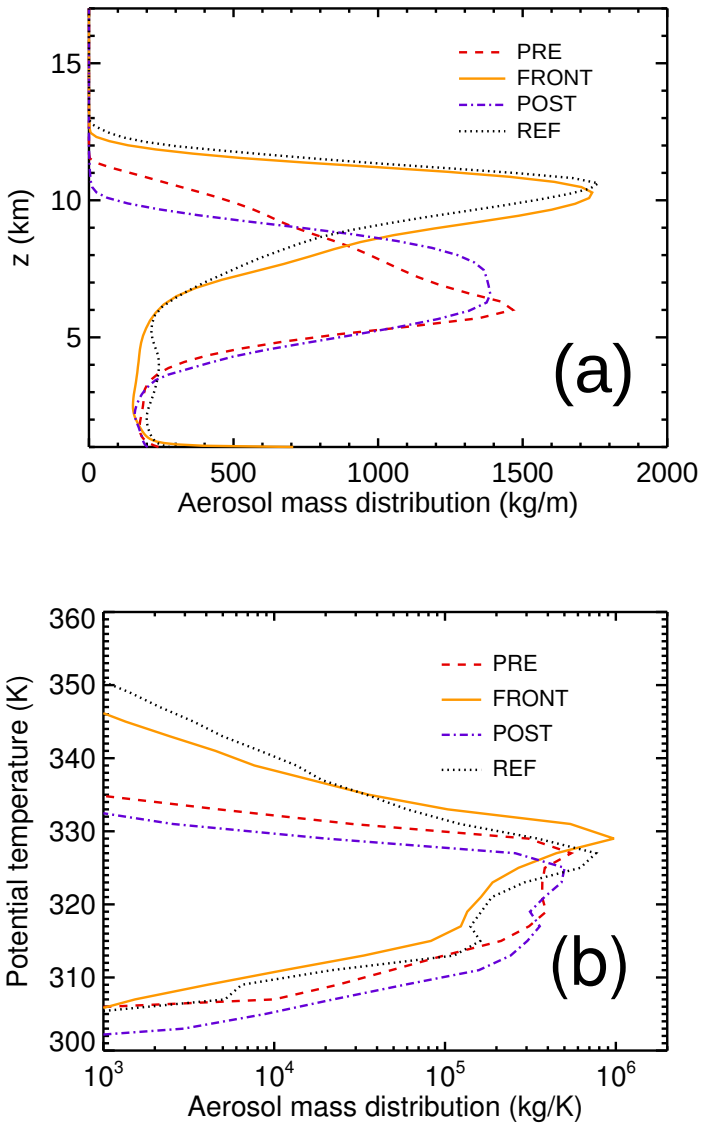

Figure 5.9: Vertical distribution of aerosol mass (a) as a function of altitude and (b) as a function of potential temperature after 30 min integration time.

ambient air is entrained into the pyroCb. As shown in Figure 5.9a and Table 5.4, the maximum height of smoke injection is at about 11 km, the vertical aerosol distribution for PRE has a maximum at 6.0 km altitude, where most of the outflow occurs.

This distribution can be understood in terms of the temperature and humidity profiles (Figure 5.2a, Section 5.3.2). Due to the warm potential temperatures in

the boundary layer, the air masses of the portion of the smoke plume situated below cloud base are highly buoyant (Figure 5.10a). Compared to the more moist conditions in FRONT and POST, however, the dry ambient air in PRE results in a higher cloud base and less latent heat released (Figure 5.10b). The total hydrometeor mass in the pyroCb simulated for PRE is 2.5×10^9 kg, compared to 6.2×10^9 kg for FRONT. Also, background mid and upper tropospheric temperatures are substantially warmer. Consequently, air parcels in the pyroCb already become strongly negatively buoyant at about 6 km altitude. Air parcels overshooting this level therefore tend to sink back, giving rise to the observed peak in the aerosol distribution at this altitude. No aerosol is transported beyond potential temperatures of about 335 K, consequently the amount injected above the tropopause level is very small compared to that in FRONT (Figure 5.9b, Table 5.4).

In the POST case, the aerosol plume only penetrates to $z_{\max}$=9.7 km. Due to strong upper level winds, the plume is quickly advected to northwesterly directions and the maximum altitude is reached far downwind of the fire location. The air in the boundary layer is colder and more stably stratified than in PRE and FRONT (Figure 5.2), therefore the air masses in the plume are significantly less buoyant in the lowermost 4 km of the troposphere. Above approx. 6 km, the air parcels in the smoke plume become negatively buoyant, resulting in an outflow level at z_{out}=6.6 km altitude. Due to the high humidity in the boundary layer (about 9 g kg^{-1}) and the colder temperatures (15°C at ground level), the pyroCb's cloud base is at 3.5 km, lower than for PRE and FRONT. The latent heat release results in a temperature lapse rate within the plume that is only slightly larger than the ambient lapse rate. Consequently, the plume air parcels are almost neutrally buoyant between 5 km and 9 km (Figure 5.10a). Along with the strong wind shear, this explains that the aerosol mass is almost evenly distributed in this altitude range (Figure 5.9a). There is no significant amount of aerosol above 330 K (Figure 5.9b). The aerosol mass injected into the stratosphere is therefore very small (Table 5.4).

Due to the warm and moist air masses in the boundary layer (Figure 5.2b), the profile used in FRONT is strongly convectively unstable. The air parcels in the updraft region of the pyroCb therefore remain positively buoyant up to a level of about 10 km (Figure 5.10a). Between approximately 7 and 8 km the buoyancy is reduced to almost zero, due to the delayed glaciation induced by the aerosol effect on microphysics described in Section 5.4.4. The pyroCb significantly overshoots into the tropopause inversion and reaches a maximum penetration height of $z_{\max}$=11.8 km. The aerosol distribution as a function of potential temperature features a maximum at 330 K. 3.5×10^5 kg of aerosol mass is injected above the

332 K tropopause, slightly more than in REF.

Even though FRONT and REF are similar in terms of vertical aerosol distribution, the total masses of condensed hydrometeors and stratospheric aerosol injection, as well as the 3-D shape of the plumes are significantly different (Figures 5.8). In REF the anvil spreads into a round, umbrella-like shape, while the anvil obtained for FRONT is advected much faster into the downwind direction because of a much more pronounced jet in the UT/LS region in this simulation. The cloud top structure obtained for REF more closely resembles observations from radar and satellite borne radiometers and should therefore be considered the best approximation of the real world situation.

The integrated buoyancy IB is rather large for all background profiles used. It is largely dominated by the contribution from the fire heating at low levels, where the smoky air parcels are least diluted. The difference in IB between the various numerical experiments correlates well with the mean vertical velocities. For FRONT, IB is highest at 2290 J kg^{-1}, and $\overline{w}$=17.2 m s^{-1}. For PRE and POST, IB is somewhat lower with 1970 J kg^{-1} and 1860 J kg^{-1}, respectively, and $\overline{w}$ is reduced to 16.8 m s^{-1} and 15.3 m s^{-1}, respectively (Table 5.4).

5.5 Summary and conclusions

We have presented numerical experiments studying the sensitivity of deep-convective transport of smoke from the Chisholm wildfire into the UT/LS to fire emissions and background meteorology. From our results we conclude that the evolution of the pyroCb convection and the transport to the UT/LS is dominated by the heat release from the fire and the background meteorology. The release of water vapor and aerosol particles were found to be of much lower significance.

The finding that sensible heat release is the most important parameter influencing the Chisholm pyroCb convection is consistent with other studies [*Penner et al.*, 1986; *Lavoué et al.*, 2000], and should apply similarly to other cases of pyro-convection. Air parcels receiving greater input of heat from the fire ascend to higher altitudes, thereby condensing and freezing more of the available water and releasing additional latent heat, thus giving rise to a positive feedback. The strength of this feedback strongly depends on the meteorological conditions, such as the background temperature and moisture profiles.

As discussed in Chapter 3, there is significant uncertainty about the partitioning of the combustion energy between sensible heat available for convection and energy that is lost radiatively. According to our simulations, the structure, altitude and penetration height observed during the peak activity of the Chisholm

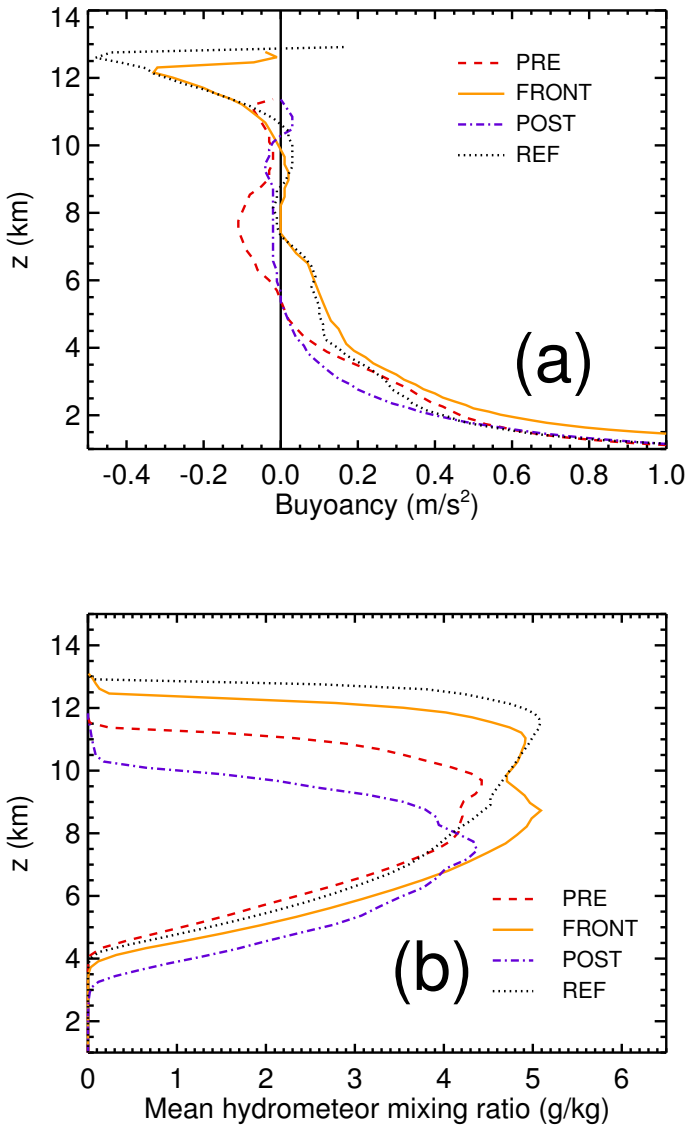

Figure 5.10: Vertical profiles of (a) mean buoyancy $\overline{b}$ and (b) mean hydrometeor content in the pyroCb's updraft region.

pyroCb can only be reproduced if the radiative loss is assumed to be small compared to the heat available for convection. Consequently, the radiative loss is likely to be smaller than the values of 30–60% obtained from laboratory and field studies of small fires [*McCarter and Broido*, 1965; *Packham*, 1969]. Possibly, a major portion of the radiation becomes intercepted by the pyroCb itself, which is rather intransparent in the thermal IR. It is also conceivable that there is a

scale effect involved: the larger the fire, the larger the volume of air-mass getting entrained into the convection and the higher the ratio of fire radiation absorbed within that region. Radiative energy absorbed on small spatial scales results in sensible heating, consequently reducing the radiative loss.

The low sensitivity of the pyro-convection dynamics to the release of fire moisture is in contrast with the results of *Potter* [2005], who postulated, based on theoretical considerations and observations, that the fire moisture could account for a large portion of the liquid water content and strongly contribute to the updraft dynamics for many pyro-clouds. Certainly, the relative contribution of the fire moisture to the cloud liquid water depends strongly on the environmental humidity, entrainment and fuel moisture. Its impact on convection dynamics is determined by the ratio of latent to sensible heat released by the fire. This ratio is constrained by reasonable ranges of fuel moisture and radiative losses. In a comment to *Potter* [2005], *Luderer et al.* [2007a] show based on the combustion equation that the assumptions used in *Potter* [2005] are inconsistent with the relative amounts of combustion heat and released moisture (cf. also Chapter 6). Hence, for pyro-convection the role of fuel moisture is generally less important than that of sensible heat.

According to our model experiments, the updraft dynamics of the Chisholm pyroCb is only weakly affected by CCN effects on microphysics. While previous studies reported stronger convection with increasing CCN pollution [*Andreae et al.*, 2004; *Koren et al.*, 2005; *Wang*, 2005], our findings are opposite: The updraft dynamics in the reference experiment is slightly weaker than without CCN inputs from the fire. In *Andreae et al.* [2004] and *Koren et al.* [2005], the invigoration of deep convection with increasing aerosol abundance is explained by a delay in precipitation formation and consequent suppression of downdrafts and warm rain. In this scenario, convection reaches higher and is more likely to reach the freezing level, thereby releasing additional latent heat. Because of the lack of precipitation formation within the updraft region for both the reference and the loCCN simulations, there are no invigorating effects of CCN on dynamics for the special case of mid-latitude pyro-convection studied here. The weak negative feedback can be explained by the delay in the freezing of the small cloud droplets in the polluted case, resulting in later release of the latent heat of freezing and decreased buoyancy.

Two-moment microphysics schemes such as the one used in this study are limited in their ability to simulate the development of precipitation-sized hydrometeors. The width of the hydrometeor size distribution is prescribed, therefore the broadening of the droplet spectrum through collision and coalescence is not

reproduced. As a consequence, the simulated precipitation formation might be underestimated. We had to limit ourselves to this approach due to computational constraints. Efforts to implement a more complex spectral hydrometeor scheme [*Khain et al.*, 2000] for further investigations are under way.

From sensitivity experiments with different background profiles we inferred that meteorological effects are of major importance for the convection dynamics. Due to the large contribution of latent heat release from entrained moisture to the total convection energy and the significant entrainment at intermediate levels [*Trentmann et al.*, 2006, and Chapter 3], the convection is strongly influenced by the humidity in the low and mid-troposphere. Whereas initialization with a frontal profile resulted in substantial stratospheric smoke injection, the vertical development was much weaker for the pre-frontal and post-frontal profiles. This finding is in good agreement with the severe intensification of the pyro-convection upon the passage of a cold front that was observed for the Chisholm pyroCb (*Fromm and Servranckx*, 2003; *Rosenfeld et al.*, 2007) as well as other pyroCbs [*Fromm et al.*, 2005].

The recently discovered phenomenon of biomass smoke injection into the lower stratosphere by severe pyro-convection might have substantial impact on atmospheric chemistry and climate. For the case of the Chisholm pyroCb, we were able to reproduce the stratospheric smoke injection. We identified fire heating and background meteorology as the most important contributing factors. Assessing the effects of pyro-convection on a global scale is challenging. It requires not only accurate knowledge about the frequency of pyroCb events but also about the altitude and potential temperature level to which biomass smoke is transported. For this purpose, and the development of parameterizations, additional studies of other pyroCb events with a variety of atmospheric conditions and fire activities are required.

Chapter 6

The role of fire-released moisture on the dynamics of atmospheric pyro-convection[1]

Abstract. We investigate the hypothesis, stated in a recent paper published in this journal [*Potter*, 2005], that the moisture released by wildland fires can be a dominant contributor to the water budget and the convection dynamics of pyro-clouds forming atop fire plumes. Using an approach based on stoichiometric principles and parcel theory of convection, we assess the relative contribution of sensible heat and latent heat to the convection energy. In contrast to *Potter* [2005], we find that moisture release is of much lesser importance for the fire convection than the fire's sensible heat. We conclude from theoretical considerations that it is highly unlikely that the decrease of the cloud base of pyro-cumulus compared to that of ambient free convection (reported by *Potter* [2005]) is due to the fire-released moisture alone.

In addition, numerical simulations of a specific case study are presented. They show that the fire-released moisture accounts only for a small portion of the total water in the pyro-cumulus cloud. Also, the effect of the fire-released moisture on the convection dynamics and the height of injection is found to be small compared to the effect of the sensible heat release from the fire.

[1]This Chapter is based on the manuscript "The role of fire-released moisture on the dynamics of atmospheric pyro-convection" by G. Luderer, J. Trentmann, and M. O. Andreae, submitted for publication in the International Journal of Wildland Fire [*Luderer et al.*, 2007a].

6.1 Introduction

Convection induced by large fires is a very efficient mechanism for the vertical transport of smoke to higher atmospheric layers. Depending on fire intensity and the meteorological conditions in the ambient atmosphere, smoky air parcels ascending above the fire can become saturated in water vapor. The latent heat resulting from the condensation of water vapor results in additional buoyancy and gives rise to substantially enhanced vertical development of convection. Such so-called pyro-cumulus clouds [*Glickmann*, 2000] are regularly observed for a variety of fire types and geographical locations, such as deforestation fires in the tropics [*Reid et al.*, 1998; *Andreae et al.*, 2004], mid-latitude and boreal forest fires [*Radke et al.*, 1991; *Fromm and Servranckx*, 2003; *Fromm et al.*, 2005], and under subtropical conditions [*Fromm et al.*, 2006].

Understanding of the dynamics of pyro-convection is highly relevant for both atmospheric research and fire management. It is well known that fire behavior is very sensitive to atmospheric conditions, and, in turn, atmospheric convection triggered by the fire has the potential to influence the fire. Because biomass burning plays a large role in atmospheric chemistry and climate [*Crutzen and Andreae*, 1990; *Penner et al.*, 1992; *Andreae and Merlet*, 2001], pyro-convection, as a highly efficient vertical transport mechanism, is of great importance for the spatial distribution of trace gases and aerosol particles emitted from biomass burning.

A recent paper published in this journal has discussed the role of moisture released by wildfires, and its influence on the convection dynamics of fire plumes [*Potter*, 2005, hereafter abbreviated as Po05]. Two hypothesis stated are stated in this paper: First, it is argued that moisture released by the fire can constitute a large portion of the total water content of fire plumes. Second, Po05 hypothesizes that the convection dynamics is not only influenced by the fire moisture, but that fire moisture constitutes a dominant contribution to the dynamics, unless fire plumes are too small to result in condensation and cloud formation, or unless the convection is wind-induced.

Both observational evidence and theoretical considerations are specified in support of these hypotheses. For one case, namely the Mack Lake fire [*Simard et al.*, 1983], the estimated cloud base altitude is compared with the lifting condensation level (LCL) that ambient convection without fire forcing would have had. From the finding that the pyro-cloud base was significantly lower than the LCL of the ambient atmosphere, the importance of moisture input from the fire is concluded. For three more cases of pyro-convection, the approximate plume heights are compared with the ambient environmental equilibrium height. For all cases, the plume heights substantially exceeded the environmental equilibrium heights. For further

theoretical support, Po05 presents calculations of convective available potential energy (CAPE) for different assumptions of temperature and humidity increases from the fire. For the assumptions used, Po05 found the impact of fire moisture to be substantial.

The ratio of released latent heat in the form of water vapor and sensible heat is constrained by the stoichiometric combustion equation, as well as reasonable values of fuel moisture and radiative losses. Based on this consideration, we will argue in the following sections that 1) the observed increase of cloud height is mostly due to the heating from the fire rather than the moisture released, 2) the observed decrease in cloud base was most likely not due to released moisture, and 3) the assumptions used for the calculations of the respective effects of fire heating and moisture on the convection dynamics are not consistent with the relative release of heat and moisture according to the combustion equation, and resulted in misleading conclusions. In Section 6.4, we present results from numerical simulations and sensitivity studies of the Chisholm fire, demonstrating the minor significance of released moisture on convection dynamics for this particular case study.

6.2 Theoretical considerations

There are two terms contributing to the moisture released from vegetation fires: First, the fuel moisture, i.e., the water already contained in the fuel. Second, water vapor is released as a product of the chemical transformation of carbohydrates during the combustion process. This term is referred to as combustion moisture.

In the combustion equation as formulated by *Ward* [2001], both terms are represented explicitly:

$$\begin{aligned} &4\,C_6H_9O_4 + 25\,O_2 + [0.322\,M\,H_2O + 94.0\,N_2] \\ \longrightarrow\ &18\,H_2O + 24\,CO_2 + [0.322\,M\,H_2O + 94.0\,N_2] \\ &+11.6 \cdot 10^6\,\mathrm{J/mol}, \end{aligned} \tag{6.1}$$

where M is the wood moisture content in mass percent relative to the dry mass. Here, water from fuel moisture and nitrogen of the air are bracketed, since they are not chemically transformed. This equation somewhat simplifies biomass combustion. Since combustion is typically incomplete, and since biomass fuels contain a variety of components in addition to cellulose ($C_6H_9O_4$), there are further trace compounds emitted by the fire that are not considered in Eq. (6.1). They are, however, not relevant in the context of this study.

There is significant uncertainty about fuel moistures characteristic of wildfire conditions. Po05 states that "actual fuel moistures are often in the 10% range". It must be considered, however, that large wildfires typically also burn a major fraction of the surface duff layer and living canopy [e.g., *FIRESCAN Science Team*, 1996]. The duff and living fuels tend to be wetter than dead surface fuels, giving rise to effective fuel moistures of up to 60-80% (BM Wotton, personal communication, January 2007).

Eq. (6.1) allows us to compare the relative contributions of the release of sensible heat and latent heat in the form of water vapor from the fire. With the molecular weights of water and $C_6H_9O_4$, it yields a total water vapor emission factor (EF) per unit dry fuel mass of $EF_{\mathrm{H_2O}} = (0.56 + 0.01M)\ \mathrm{kg_{H_2O}/kg_{fuel}}$. With the latent heat of vaporization $L = 2.5 \cdot 10^6 \mathrm{J/kg_{H_2O}}$ this corresponds to a latent heat release of

$$EF_{\mathrm{LH}} = (1.4 + 0.025M)\ \mathrm{MJ/kg_{fuel}}. \tag{6.2}$$

From Eq. (6.1), the heat of combustion can be also calculated as

$$EF_{\mathrm{H}} = (20.0 - 0.025M)\ \mathrm{MJ/kg_{fuel}}, \tag{6.3}$$

where the subtrahend is introduced to account for the consumption of a certain portion of the combustion energy released by the fire for the vaporization of fuel moisture. For dry to moderately dry fuels, the combustion moisture dominates the fire released moisture. For effective fuel moistures larger than 56%, by contrast, the release of fuel moisture exceeds that of combustion moisture. It is important to note that the total latent heat release accounts only for less than 20% of the total fire energy.

Not all of the heat released becomes available for convection. While the conduction of heat into the ground is rather insignificant [*Byram*, 1959], a substantial fraction of the fire energy is lost by radiative processes. There is significant uncertainty about the radiative losses. Estimates based on laboratory studies and field experiments with small fires range from values close to zero [*Wooster*, 2002; *Wooster et al.*, 2005] to values as high as 50% [*McCarter and Broido*, 1965; *Packham*, 1969].

For the further derivations, it is useful to introduce the perturbation ratio r between temperature increase due to sensible heating, and humidity increase due to released moisture, which is constrained by their respective emission factors:

$$\begin{aligned} r &\equiv \frac{\Delta T}{\Delta q} = \frac{(1 - 0.01l)\ EF_{\mathrm{H}}}{c_p\ EF_{\mathrm{H_2O}}} \\ &= \frac{(1 - 0.01l)(20.0 - 0.025M)}{1.005(0.56 + 0.01M)} \left[\frac{\mathrm{K}}{\mathrm{g/kg}}\right], \end{aligned} \tag{6.4}$$

where l is the radiative loss in percent and a value of $c_p = 1005\,\mathrm{J\,kg^{-1}\,K^{-1}}$ was used for the specific heat capacity of air. The perturbation ratio concept relies on two assumptions: First, it is assumed that radiative cooling and other losses of sensible heat are confined to the region very close to the fire, and second, sensible heat and fire moisture are assumed to dilute at the same rate over the further course of the plume development. The first assumption is justified by the short timescales of pyro-convection (∼10-20 min) and the fact that the temperature anomalies above the fire decrease rapidly with increasing altitude [*Byram*, 1959; *Trentmann et al.*, 2006]. The second assumption is consistent with observational evidence that the eddy diffusivity for heat and trace gases are equal under neutrally stratified conditions [*Stull*, 1988]. For the complex dynamics present in convection, by contrast, the eddy diffusivity for heat tends to exceed that of trace gases such as water vapor [*Deardorff*, 1980]. This is a key limitation of our approach and requires further study. However, the results of numerical simulations presented in Section 6.4, which account for the difference between turbulent transport of heat and moisture, suggest that this effect is not important.

The perturbation ratio r as a function of the radiative loss is given in Figure 6.1 for three different fuel moistures. For reasonable ranges of fuel moisture (0-80%) and radiative losses (0-50%), the perturbation ratio is in the range of 6.6-35 $\mathrm{K(g/kg)^{-1}}$. In other words, a humidity increase of 1 g/kg corresponds to a temperature increase of at least 6.6 K. Since 1 g/kg of water vapor corresponds to 2.5 K of latent heat, this means also that, even for extreme assumptions on both radiative loss rate (50%) and fuel moisture (80%), the release of sensible heat exceeds that of latent heat by a factor of 2.6.

This is in contrast with Po05's statement that released moisture can play a dominant role in fire-induced atmospheric convection. Po05 demonstrated the importance of released moisture by calculating the effects of temperature increases of 2 K and 3 K as well as those of humidity increases of 2 g/kg and 3 g/kg on CAPE. The results presented by Po05 suggest that the effects of latent heat are even greater in magnitude than those of sensible heating. This is inconsistent with the perturbation ratios in the range of 6.6-35 $\mathrm{K(g/kg)^{-1}}$ obtained with our approach, and casts doubt on the validity of the conclusions about the role of fire-released moisture on the dynamics of pyro-convection drawn by Po05. If humidity and temperature increases had been compared at perturbation ratios of 6.6 $\mathrm{K(g/kg)^{-1}}$ or larger, the effects of moisture would have been found to be smaller by at least a factor of six and hence of smaller significance compared to sensible heating by the fire.

In addition to the moisture released directly by the fire, drying of soil and other

unburned material might contribute to the plume's water budget. *Clements et al.* [2006] conducted measurements of water vapor and heat fluxes from a prescribed grass fire. They report that the fire enhanced the sensible heat flux by 1155 W m^{-2} while the latent heat flux was increased by 347 W m^{-2}, corresponding to a perturbation ratio of 8.3 $K(g/kg)^{-1}$. The fire experiment was conducted in the morning when significant amounts of moisture were released by the soil and vegetation, hence a substantial portion of the enhancement in the latent heat flux might have been due to increased vertical transport of surface moisture due to the fire convection. If this effect is considered, the actual perturbation ratio might have been substantially larger than 8.3 $K(g/kg)^{-1}$. This value is in good agreement with the result of our theoretical considerations and exceeds the perturbation ratio of 1 $K(g/kg)^{-1}$ used by Po05 by almost an order of magnitude.

6.3 Effects on convection characteristics

6.3.1 Plume height

The observational support in Po05 relies on two aspects, enhanced plume heights and lowered cloud base in pyro-cumulus compared to ambient clouds. Po05 lists reports of pyro-convection, for all of which the plume extended well above the environmental equilibrium height. However, as acknowledged by Po05, this can not be attributed conclusively to the effect of released moisture. While enhanced plume heights indicate that the fire forcing substantially influences the atmospheric dynamics and invigorates the convection, they do not give any indication about the relative contribution of fire heating and released moisture. As discussed above, sensible heat strongly dominates over latent heat even for large fuel moistures and strong radiative losses, suggesting that the increase in plume height is mostly due to sensible heat inputs.

6.3.2 Condensation level

A second aspect discussed by Po05, namely a possible decrease in the condensation level of pyro-convection compared to convection in ambient air, is difficult to explain based on fire emissions. Po05 cites the pyro-cloud produced by the Mack Lake fire from 1980 [*Simard et al.*, 1983], the cloud base of which was estimated from a photograph to be 2300 m. From a meteorological sounding taken 185 km away on the same day, the estimated LCL for convection in the ambient atmosphere would have been 3150 m, substantially higher than the estimate from the photograph. It is important to note that the fire influences the LCL in two ways:

On the one hand, the increased temperature within the plume tends to result in higher saturation vapor pressures, hence delayed condensation. The released moisture, on the other hand, tends to result in decreased LCL.

This leads to the question of which effect dominates for given parameters such as ambient humidity, temperature and fuel moisture. We can address this issue analytically in terms of parcel theory of convection [*Rogers and Yau*, 1989]. Let us consider the pressure at the LCL, p_{LCL}, for which we can make use of the saturation condition [e.g., *Rogers and Yau*, 1989]

$$p_{LCL} = \frac{\epsilon\, e_s(T_{LCL})}{q}, \tag{6.5}$$

where $\epsilon \approx 0.622$ is the ratio between the molar mass of water vapor and that of air, $e_s(T_{LCL})$ the saturation vapor pressure at the parcel temperature at the LCL, and q the air parcel's specific humidity.

Assuming that the air parcel ascends adiabatically from a reference level with pressure p and temperature T we can also make use of

$$T_{LCL} = T \cdot \left(\frac{p_{LCL}}{p}\right)^{\kappa}, \tag{6.6}$$

where $\kappa \approx 0.286$ is the ratio between the gas constant and specific heat at constant pressure [e.g., *Rogers and Yau*, 1989].

We can assess the effect of increases of temperature ΔT and humidity Δq by applying a linearization approach to Eq. (6.5). As described in the Appendix, a functional relationship between the relative change of the pressure lifting condensation level and the temperature and humidity perturbations can be derived from Eqs. (6.5) and (6.6):

$$\frac{\Delta p_{LCL}}{p_{LCL}} = \frac{\frac{\Delta q}{q} - \frac{L}{R_v T_{LCL}}\frac{\Delta T}{T}}{\frac{\kappa L}{R_v T_{LCL}} - 1}. \tag{6.7}$$

Assuming that the humidity perturbation is proportional to the temperature perturbation according to Eq. (6.4), we can assess the *combined effect* of temperature and humidity perturbation on the lifting condensation level. Substituting $\Delta q = \Delta T / r$ and rearranging Eq. (6.7) yields a change in pressure lifting condensation level per unit fire heating of

$$\frac{\Delta p_{LCL}}{\Delta T} = \frac{\frac{1}{rq} - \frac{L}{R_v T T_{LCL}}}{\frac{\kappa L}{R_v T_{LCL}} - 1} \cdot p_{LCL}. \tag{6.8}$$

A positive value of $\Delta p_{LCL}/\Delta T$ would indicate a decrease in cloud base altitude due to the fire effect, while a negative value would indicate a higher cloud base.

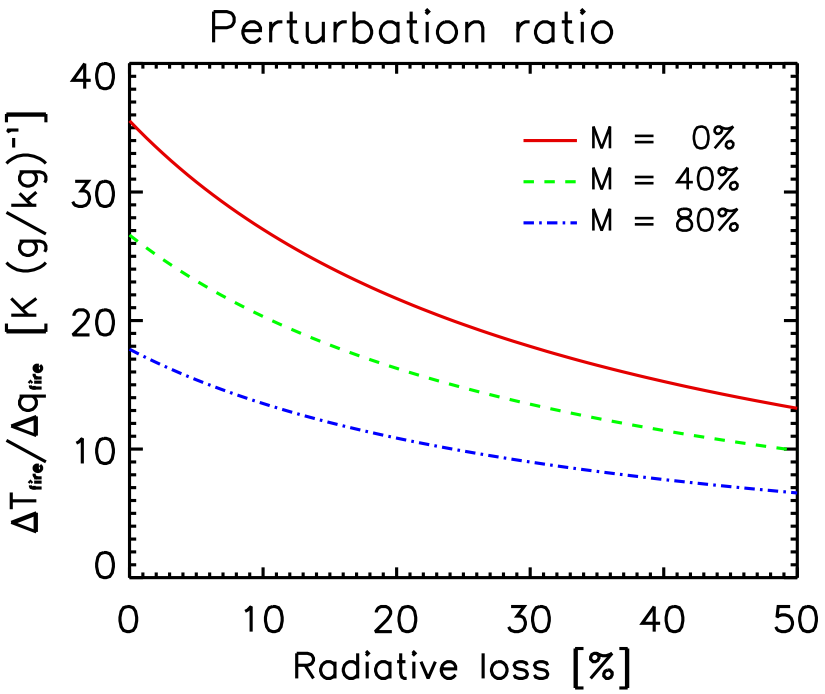

Figure 6.1: Ratio between temperature and humidity perturbation as a function of radiative loss for different values of fuel moisture M.

Figure 6.2 shows $\Delta p_{LCL}/\Delta T$ as a function of q and r, where reference temperature $T = 300$ K and pressure $p = 1000$ hPa were assumed, T_{LCL} and p_{LCL} were calculated from T and q, and $\Delta q = \Delta T/r$ was used. For temperatures lower than 1500 K and hence for all conditions in ambient tropospheric air, the denominator on the right side of Eq. (6.8) is positive. The sign of (6.8) is therefore equal to the right side's enumerator's sign. It is positive if and only if the perturbation ratio satisfies the inequality

$$r = \frac{\Delta T}{\Delta q} < \frac{R_v T\, T_{LCL}}{q\, L}. \tag{6.9}$$

Since the relative variability of q is much greater than that of T, inequality (6.9) is mostly dependent on specific humidity and r. Figure 6.2 shows that $\Delta p_{LCL}/\Delta T$ is only positive for extremely dry conditions $q < 2.5$ g/kg and very low perturbation ratios. For most realistic values of q and r negative values are obtained for $\Delta p_{LCL}/\Delta T$. Thus, the combined effect of released moisture and heat from the fire forcing almost always results in a decrease of p_{LCL}, i.e., a higher cloud base compared to ambient conditions.

From the meteorological conditions at the site of the fire Mack Lake fire [*Simard et al.*, 1983; *Potter*, 2005], the ambient humidity can be calculated as 5.3 g/kg.

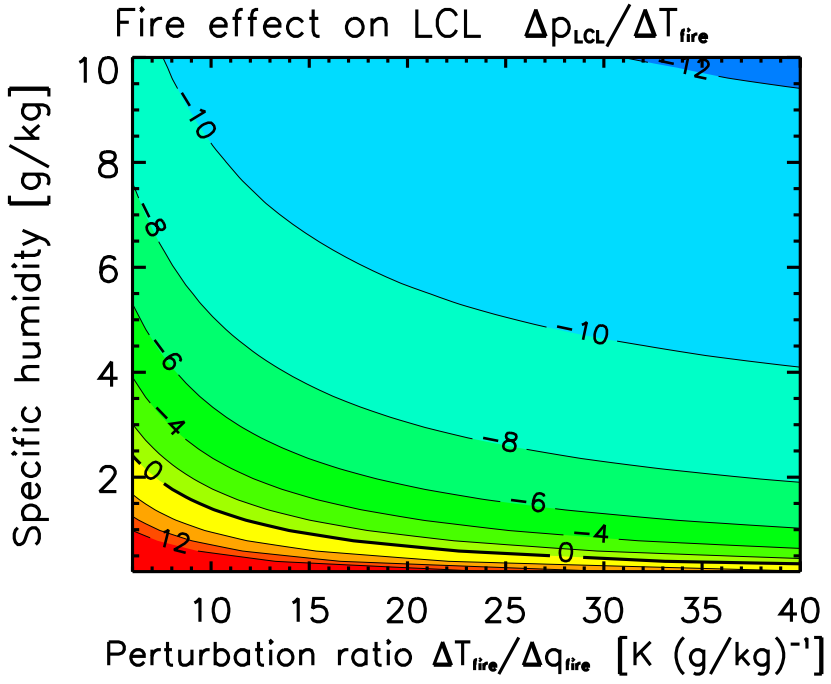

Figure 6.2: Sensitivity of p_{LCL} to the combined effects of released moisture and fire heating. Contours show $\Delta p_{LCL}/\Delta T$ in hPa/K as a function of perturbation ratio $r{=}\Delta T/\Delta q$ and specific humidity.

Assuming typical values of $T = 300$ K, $T_{LCL} = 270$ K, condition (6.9) becomes $r < 2.8$ K(g/kg)$^{-1}$. As discussed in Section 6.2, for realistic values of fuel moisture and radiative losses, r must have been much higher.

It is rather difficult to reconcile this result with the findings reported by Po05. Very intensive pyro-cumulus convection is typically observed to coincide with the passage of synoptic cold fronts [*Fromm et al.*, 2000; *Fromm and Servranckx*, 2003; *Fromm et al.*, 2005]. As documented by *Simard et al.* [1983], the major run of the Mack Lake fire occurred just before the passage of a dry cold front, hence the temperature and humidity profiles were subject to rapid change. Since the radiosonde profile used by Po05 to determine the LCL of free convection in the background atmosphere was recorded at 185 km distance from the fire and six hours later, a likely explanation would be that the atmospheric humidity and temperature profiles at the time and location of the photograph used for the estimate of the cloud base were different than those from the radiosonde.

It is also conceivable that the fire radiation and surface winds induced by the pyro-convection significantly enhance the moisture flux from the soil and other unburned material. This additional moisture is not part of the fire-released mois-

ture, yet it could significantly contribute to the moisture excess in pyro-convection compared to free convection. This effect is not accounted for in the approach presented here nor in Po05. Such convection-induced inflow of additional environmental moisture can also, at least to some extent, explain the observed lowering of the cloud base because it decreases the temperature due to evaporative cooling and increases the humidity of the air flowing into the convective updraft. The effect on convection dynamics, by contrast, is small since the drying of unburned material merely results in a redistribution between sensible and latent heat budgets.

6.4 Results from numerical simulations

In order to study the relative importance of fire heating and fire moisture taking into full consideration the complex effects of turbulence, dilution, convection dynamics and cloud microphysics, it is necessary to perform numerical simulations of the fire plume development. For a specific case study, *Luderer et al.* [2006] present a detailed investigation of the sensitivity of the dynamical development of pyro-convection and subsequent stratospheric injection to various parameters, such as fire emissions of heat and moisture, cloud microphysical effects induced by aerosol particles contained in the smoke, and background meteorology (cf. also Chapter 5).

Numerical simulations of pyro-convection, performed using the Active Tracer High resolution Atmospheric Model (ATHAM) similar to those given in *Trentmann et al.* [2006] and *Luderer et al.* [2006] are considered here in order to specifically focus on the role of fire moisture in the water budget and the convection dynamics of the fire plume (cf. also Chapter 5). ATHAM is a cloud-resolving model especially designed for the simulation of the extreme dynamics associated with eruptive events such as volcanic eruptions and fire convections [*Oberhuber et al.*, 1998; *Herzog et al.*, 2003; *Trentmann et al.*, 2002]. The Chisholm wildfire, a very large forest fire that burned in Alberta, Canada, in May 2001 [*ASRD*, 2001], and resulted in injection of smoke into the upper troposphere and lower stratosphere by pyro-convection [*Fromm and Servranckx*, 2003], is used as a case study. The Chisholm fire is well studied in terms of its fire characteristics [*ASRD*, 2001] as well as its atmospheric impacts [*Fromm and Servranckx*, 2003; *Trentmann et al.*, 2006; *Luderer et al.*, 2006; *Rosenfeld et al.*, 2007]. We operated ATHAM in a three-dimensional setup with a model domain of 85 km x 65 km x 26 km and 110 x 85 x 100 grid boxes in the x-, y- and z-directions, respectively. The total integration time was 40 min. The model setup was equal to that used in *Trentmann et al.* [2006] and therein described in detail.

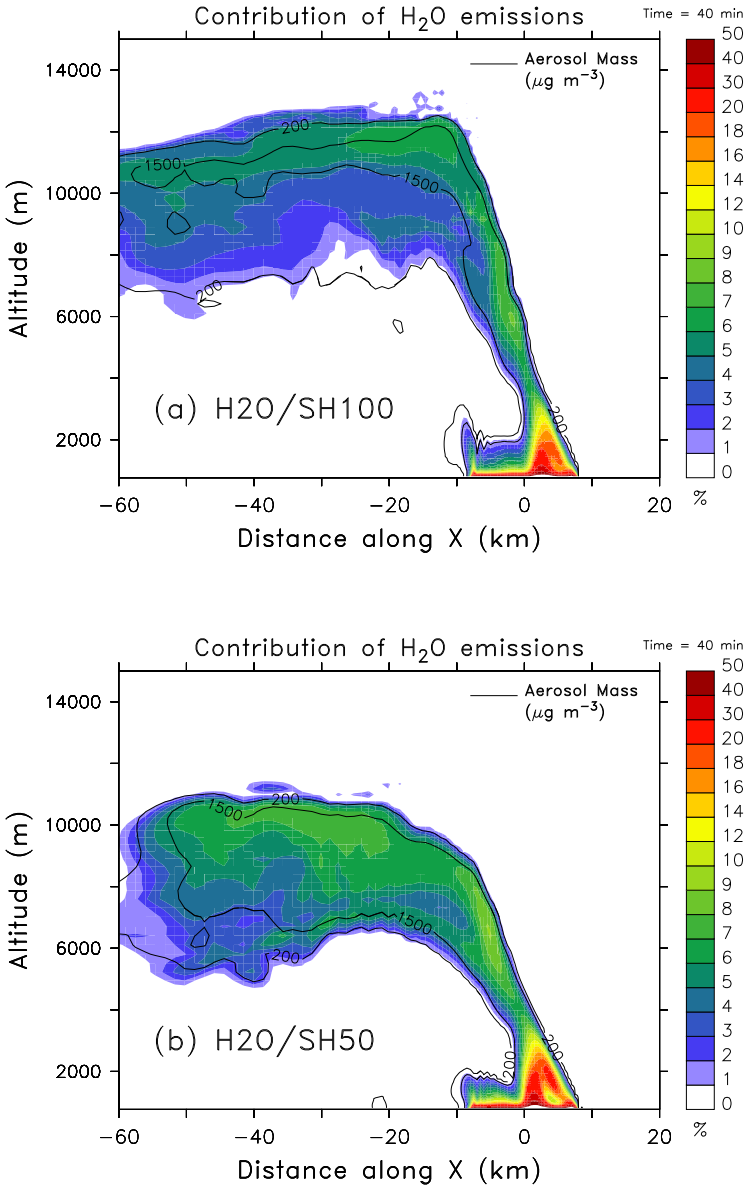

Figure 6.3: Relative contribution of the fire-released moisture to the total water content simulated for the Chisholm fire plume for the assumptions that (a) 100% of the fire energy becomes available for convection or (b) 50% becomes available for convection. The black solid lines indicate isolines of aerosol concentration. Partially adopted from *Trentmann et al.* [2006].

Here we present a set of four simulations in order to demonstrate the relative importance of the fire emissions of sensible heat and water vapor. For the first simulation, H2O/SH100, the water release from the fire was fully considered and

the radiative loss was assumed to be zero, hence 100% of the combustion energy is released as sensible heat. For the second simulation, noH2O/SH100, the water emission from the fire was set to zero, while the sensible heat release remained at 100%. In the third simulation, H2O/SH50, the full fire moisture emissions were considered and the sensible heat release was reduced to 50% of the original value, corresponding to a radiative loss of 50%. For the last simulation, noH2O/SH50, the fire moisture release was set to zero and the sensible heat release was reduced to 50%. For the simulations H2O/SH100 and H20/SH50, we assumed a value of 40% for the fuel moisture content. According to Eq. (6.4), this corresponds to perturbation ratios of 18 $K(g/kg)^{-1}$ for H2O/SH100 and 10 $K(g/kg)^{-1}$ for H2O/SH50.

The numerical model allows us to estimate the relative contribution of the fire released moisture to the total water (i.e., water vapor and condensed water) within the fire plume. Figure 6.3 shows a cross section of the ratio between fire moisture and total water obtained for the H2O/SH100 and H2O/SH50 runs. It shows that the water vapor emitted by the fire is rapidly diluted before reaching the condensation level. Within the pyro-cumulus, the fire moisture is small compared to the moisture entrained from the environment. With values of up to 10% in the updraft region, the relative contribution of the fire-released moisture in H2O/SH50 is slightly greater than in H2O/SH100, where the maximum value is 7%. This is due to the enhanced entrainment of environmental air in the more vigorous case of higher sensible heat release.

The horizontally integrated vertical aerosol distributions for the four cases after 40 min simulation time are depicted in Figure 6.4. From these results, it is evident that the influence of the fire-released moisture is small compared to the influence of the sensible heat released by the fire. Whereas the reduction of the sensible heat flux by 50% results in a decrease in the maximum plume altitude of about 1.5 km, eliminating the fire moisture release results in a decrease of only 200 m between the H2O/SH100 and noH2O/SH100 simulations, and 600 m between the H2O/SH50 and the noH2O/SH50 simulations. Hence, the sensible heat release from the fire plays a much more important role for the vertical plume development than the release of latent heat. For the two simulation runs H2O/SH50 and noH2O/SH50, the reduced sensible heat flux corresponds to a radiative loss of 50%. The difference in the plume height decrease between H2O/SH100 and noH2O/SH100 compared to the decrease between H2O/SH50 and noH2O/SH50 shows that the sensitivity of the convection dynamics to fire-released moisture increases with decreasing radiative losses. There are two reasons for this behavior: First, in the case of reduced sensible heat flux, the relative contribution of the latent heat from the fire-released

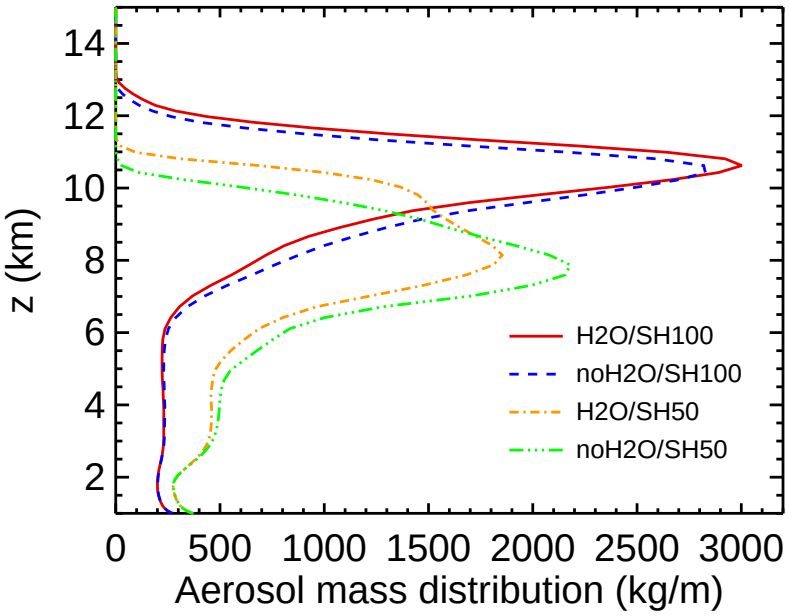

Figure 6.4: Horizontally integrated vertical aerosol distributions for four numerical simulations of the Chisholm pyroCb with varying assumptions on the release of fire moisture and sensible heat.

moisture to the total energy of the pyroCb is larger. Second, in the case of the full sensible heat flux of the fire, the plume reaches into the lower stratosphere. In this case, the additional latent heat flux from the fire-released moisture results only in a small increment in plume altitude because of the strong thermal inversion at the tropopause level, which inhibits vertical transport.

For the background atmosphere, the LCL was located at an altitude of 3250 m. The cloud base in the updraft column is at 3900 m for the simulation run H2O/SH50 and at 4200 m for H2O/SH100. Hence, the combined effect of fire heating and moisture release results in a substantial increase in cloud base altitude, rather than a decrease as reported by Po05. The higher cloud base for the case without radiative loss (H2O/SH100) compared to the simulation with 50% radiative loss is consistent with the derivation presented in Section 6.3.2.

6.5 Summary and conclusions

We have presented different approaches to investigate the role of fuel moisture in the dynamical development of atmospheric pyro-convection, and found it to be much less significant than hypothesized in Po05, even if much higher fuel moistures

are assumed than those used by Po05. We were able to attribute the disagreements between our study and Po05 to substantial discrepancies in the ratio of temperature and humidity perturbations calculated here and the assumptions used in Po05. From theoretical considerations, based on the stoichiometric release ratio between fire sensible heat and moisture, we conclude that, under all reasonable assumptions, fuel moisture and radiative losses perturbation ratios must be in the range of 6.6-35 $\mathrm{K(g/kg)^{-1}}$. These perturbation ratios exceed those used by Po05 by more than a factor of six, and imply that the fire input of latent heat originating from combustion moisture and fuel moisture is substantially smaller than the sensible heating from the fire.

Using an analytical model based on parcel theory, we also assessed the combined effects of fuel moisture and fire heating on the cloud base level. Our results show that the fire moisture has the potential to lower the cloud base level only for a rather unlikely combination of extremely dry background atmosphere ($q < 2.5$ g/kg) and a moderate to high fuel moisture content, in conjunction with high radiative losses. For all other cases, the increase in the lifting condensation level due to the heat input from the fire dominates over the decrease due to fire moisture. The contrasting result reported by Po05 is likely due to discrepancies between the atmospheric sounding used and the actual conditions during the pyro-convection, or convection-induced enhanced moisture-flux from unburned material at the ground, or a combination of both.

Numerical simulations performed for a specific case study with the three-dimensional cloud-resolving model ATHAM also suggest that the role of fire moisture is of rather low significance. For the Chisholm fire, we found that the fire moisture accounts for only about 10% of the total water in the plume, with the remainder of the water originating from the background atmosphere. From sensitivity studies, we conclude that the effect of the moisture release from the fire is small compared to the effect from the fire heating.

The theoretical derivations presented in Sections 6.2 and 6.3.2 are based on universal principles, and are therefore generally valid under the assumptions made. The simulations of a specific case study presented in Section 6.4 additionally support these analytical results based on a complex numerical model fully accounting for entrainment and dilution due to turbulence. Additionally, the model results show that the water budget of the cloud formed by the pyro-convection is strongly dominated by moisture entrained from the environment, while the fire moisture only contributes a small fraction.

In order to further advance our understanding of the different factors contributing to the dynamics of pyro-convection, further observational and modeling efforts

are both required. More in-situ or remote sensing measurements of temperature and moisture perturbation in biomass burning plumes would be of great use for the validation of models. There is still large uncertainty about the transfer of energy in the form of radiation. Also, the possible increase of environmental moisture, because of enhanced evaporation due to fire radiation and the surface wind shear induced by the pyro-convection, should be investigated in more detail.

6.6 Appendix: Derivation of Equation (6.7)

In order to assess the respective effects of temperature and humidity perturbations on the lifting condensation level, we can apply a linearization approach

$$\Delta p_{LCL} = \frac{\partial p_{LCL}(T_{LCL}, q)}{\partial q}\,\Delta q \;+\; \frac{\partial p_{LCL}(T_{LCL}, q)}{\partial T_{LCL}}\,\Delta T_{LCL} \tag{6.10}$$

to Eq. (6.5):

$$\begin{aligned}\Delta p_{LCL} = &-\frac{\epsilon\, e_s(T_{LCL})}{q^2}\Delta q \\ &+ \quad \frac{\epsilon}{q}\frac{\mathrm{d}e_s(T_{LCL})}{\mathrm{d}T_{LCL}}\left(\frac{\partial T_{LCL}}{\partial p_{LCL}}\,\Delta p_{LCL} + \frac{\partial T_{LCL}}{\partial T}\Delta T\right).\end{aligned} \tag{6.11}$$

Note that T_{LCL} itself is a function of the temperature at the reference level T and the lifting condensation level p_{LCL}, hence both its partial derivatives need to be considered as well. From Eq. (6.6), they can be calculated as

$$\frac{\partial T_{LCL}}{\partial T} = \left(\frac{p_{LCL}}{p}\right)^{\kappa} = \frac{T_{LCL}}{T} \tag{6.12}$$

$$\frac{\partial T_{LCL}}{\partial p_{LCL}} = \frac{\kappa T}{p_{LCL}}\left(\frac{p_{LCL}}{p}\right)^{\kappa} = \kappa\frac{T_{LCL}}{p_{LCL}}. \tag{6.13}$$

The differential temperature dependence of the saturation water vapor partial pressure is given by the Clausius-Clapeyron equation [e.g., *Rogers and Yau*, 1989]

$$\frac{\mathrm{d}e_s(T)}{\mathrm{d}T} = \frac{Le_s}{R_v T^2}, \tag{6.14}$$

so we can convert

$$\frac{\epsilon}{q}\frac{\mathrm{d}e_s(T_{LCL})}{\mathrm{d}T_{LCL}} = \frac{\epsilon e_s L}{R_v q T_{LCL}^2} = \frac{p_{LCL} L}{R_v T_{LCL}^2}. \tag{6.15}$$

Substituting Eqs. (5), (A6), (A4), and (A3) into Eq. (A2) yields

$$\Delta p_{LCL} = -p_{LCL}\frac{\Delta q}{q} + \frac{p_{LCL} L}{R_v T_{LCL}^2}\left(\kappa\frac{T_{LCL}}{p_{LCL}}\Delta p_{LCL} + \frac{T_{LCL}}{T}\Delta T\right). \tag{6.16}$$

Rearranging results then in the form presented in Eq. (6.7):

$$\frac{\Delta p_{LCL}}{p_{LCL}} = \frac{\frac{\Delta q}{q} - \frac{L}{R_v T_{LCL}} \frac{\Delta T}{T}}{\frac{\kappa L}{R_v T_{LCL}} - 1}. \tag{6.17}$$

Chapter 7

Conclusion and outlook

7.1 Summary and discussion

The major goal of the modeling study presented in this dissertation was to assess the nature of troposphere-to-stratosphere transport by pyroCb convection. For this purpose, the pyroCb that developed over the Chisholm fire in May 2001 was simulated and sensitivity studies were conducted.

The simulated structure and shape of the pyroCb is in good agreement with the observations. In the simulation, the Chisholm pyroCb reaches to an altitude of 12.5 km, slightly lower than the maximum altitude of 13.5 km derived from the observations. The pyroCb spreads into a large, roughly circular anvil. Above the updraft region, an overshooting dome is formed which exceeds the anvil level by about 1000 m. At and downwind of the overshoot, in good agreement with the observations, the pyroCb is characterized by anomalously warm cloud top brightness temperatures. At the same time, brightness temperatures in an arch-shaped region at the upwind side of the overshooting dome are much colder than the minimum tropopause temperatures.

The numerical results yield valuable insights for the interpretation of the observations. The detailed analysis of the modeled cloud top structure presented in Chapter 4 demonstrates that the bipolar cloud top brightness temperature pattern, found both in observations and the simulation, was due to dynamical processes at the cloud top. The overshooting dome of the pyroCb induced the formation of a stationary gravity wave. The large gradients of potential temperature and turbulence generated by the gravity wave induced mixing of downwelling, potentially warm stratospheric air with smoke-laden pyroCb air masses. This mechanism gives rise to the observed region of warm air at the cloud top and significantly enhances the troposphere-to-stratosphere transport of smoke.

Microphysically, the Chisholm pyroCb was extremely continental. Low radar reflectivities in the updraft region and satellite retrieval of hydrometeor effective radius show that the pyroCb was characterized by very small cloud droplets and that its anvil mainly consisted of small ice particles. Due to the small droplet size in combination with large updraft velocities that left little time for droplet coagulation, the pyroCb was very inefficient in forming precipitation. The numerical simulations succeed in reproducing this microphysical structure, and show that it was due to the extremely high abundance of aerosol particles acting as cloud condensation nuclei (CCN). Whereas the fire aerosol has a strong effect on the pyroCb's microphysics, there is only little effect on the dynamics.

Background meteorological conditions strongly affect the convection dynamics. A series of three simulations with meteorological conditions representative of pre-frontal, frontal, and post-frontal conditions, respectively, were conducted (Chapter 5.4.5). The convective intensity and injection height reach a maximum for the frontal conditions, whereas pre-frontal and post-frontal conditions result in much less efficient vertical transport. This result is consistent with the severe intensification of pyro-convection shortly before the arrival of a synoptic cold front observed for the Chisholm fire and other cases of pyroCb convection.

The convection dynamics are also found to be very sensitive the fire heating. For sensitivity simulations with reduced fire release of sensible heat, the vertical development is much weaker than in the reference simulation, and no significant amounts of smoke are injected into the stratosphere. The large sensitivity of the model results on meteorological conditions and fire heating suggests that the uncertainty in these parameters dominates the uncertainty in the model results.

In a sensitivity study, in which the moisture release from the fire was deactivated, it was found that the fire moisture has only little effect on the dynamical development and vertical extent of the pyroCb. This finding can be explained by an analysis of the pyroCb's water budget. According to the model results, the fire-released moisture only accounts for a small fraction of the total water mass in the pyroCb. Most of the water and hence latent heat originates from entrainment of environmental air. This result is in disagreement with the hypothesis stated by *Potter* [2005], according to which fire moisture has the potential to play a dominant role in the dynamics of pyro-convection. As shown based on general principles in Chapter 6, fire release of sensible heat always dominates over the fire release of latent heat.

An analysis with passive, inert tracers shows that, in addition to air masses from the boundary layer, air masses entrained at low- and mid-tropospheric levels contribute significantly to the pyroCb air. This finding has important implica-

tions for the convection dynamics and indicates that the pyroCb development is particularly sensitive to humidity and temperature profiles at mid-tropospheric levels.

As part of this work, for the first time ever, a comprehensive modeling study of deep convective transport of biomass smoke into the lower stratosphere was conducted. The presented numerical simulations confirm the observational evidence that large boreal forest fires in combination with favorable meteorological conditions have the potential to directly inject fire smoke into the upper troposphere and lower stratosphere. In summary, according to our results, the key ingredients for direct smoke injection into the lower stratosphere are 1) strong thermal forcing through the release of sensible heat by the fire, 2) favorable meteorological conditions with significant convective instability and sufficient low and mid-level moisture in the background atmosphere, and 3) the enhancement of stratospheric injection due to small-scale mixing processes at the cloud top.

A large fraction, about 12 K, of the potential temperature gain of air parcels ending up in the upper part of the pyroCb originates from latent heating due to condensation and freezing of moisture, most of which is entrained from the ambient atmosphere. By contrast, due to significant dilution in the updraft region, the effect of the sensible heat release from the fire corresponds to only 6 K. Despite the dominance of latent heating, simulations with different levels of fire sensible heat release show that the vertical development of the pyroCb is highly sensitive to the fire heating. The stronger vertical development induced by stronger fire forcing results in larger amounts of latent heat release, hence further enhancing the vertical development. Furthermore, for sufficiently large fire-forcing, small-scale transport processes induced by the overshooting dome result in significantly enhanced troposphere-to-stratosphere transport. This effect corresponds to a potential temperature gain of as much as 20-30 K.

The modeling results presented in this thesis in conjunction with a growing body of observational findings suggest that deep convection induced by pyroCbs is an important source of stratospheric aerosol and trace gases and must be considered in addition to other sources like volcanism. This might have important implications for the radiative balance of the atmosphere and the chemistry of the lower stratosphere.

7.2 Future research needs

The study of deep convective transport of biomass smoke into the upper troposphere and lower stratosphere is a rather new field of research in the Atmospheric

Sciences. There are still a number of open questions that should be addressed by further research in order to advance our understanding of this phenomenon and its implications for the atmosphere.

More studies are needed to further improve our understanding of the causes and effect of UT/LS aerosol plumes originating from forest fires. Observational studies of pyroCb clouds would be desirable to obtain further constraints on the dynamical and microphysical structure of pyroCbs. Observations from Doppler radar, for instance, could provide valuable information on velocity fields and convection dynamics. Aircraft measurements could provide information on trace gases, composition and size distribution of aerosol particles, and microphysical properties.

More convection-scale modeling work for other case studies and geographical regions would be also desirable. Regional simulations for longer timescales and larger spatial scales also considering radiative effects would enhance the understanding of the further development of lower stratospheric aerosol plumes induced by pyroCbs.

While the results presented here suggest that aerosol-microphysics interactions did not have a strong effect on convection dynamics for the specific case of the Chisholm fire, studies for other conditions, such as *Andreae et al.* [2004], come to different conclusions. Modeling studies comparing microphysics-dynamics interactions for a variety of cases could provide valuable new insights.

Two-moment microphysics schemes such as the one used in this study are limited in their ability to simulate the development of precipitation-sized hydrometeors. The width of the hydrometeor size distribution is prescribed, therefore the broadening of the droplet spectrum through collision and coalescence is not reproduced. As a consequence, the simulated precipitation formation might be underestimated. We had to limit ourselves to this approach due to computational constraints. Modeling studies with more complex cloud microphysical schemes would be desirable.

One of the most important challenges to be addressed by convection-scale modeling of pyroCbs is the quantification of the amount of particulate matter injected into the upper troposphere and lower stratosphere regions. The estimates presented here only account for nucleation scavenging in a parameterized form, and neglect the possible effect of impaction scavenging. Explicit treatment of aerosol transport within the hydrometeors fully accounting for all scavenging processes would enhance our understanding of vertical transport of particulate matter in convective columns, and reduce the uncertainty in quantitative estimates of stratospheric injection.

PyroCb convection results not only in injection of particulate matter, but also

transports large amounts of gaseous trace gases to the upper atmosphere. Little is known about the effect of pyroCb convection on trace gas chemistry of the upper troposphere and lower stratosphere. *Fromm et al.* [2005] report observations of significantly enhanced ozone in a lower stratospheric biomass burning plume. Chemical transport modeling on both the scale of convection and larger scale is necessary to enhance our understanding of the potential impact of forest fire smoke on upper atmospheric chemistry and composition.

In order to further estimate their relevance for the atmosphere, it would be desirable to establish a climatology of the frequency and geographical distribution of pyroCb events. For the studies with large scale models, it will be necessary to derive parameterizations of injection height as a function of meteorological conditions and fire intensity. Global coupled chemistry climate models could then be used to assess the large-scale and long-term effect of pyroCb convection on atmospheric radiation, stratospheric chemistry, and climate.

Appendix A

List of abbreviations

ATHAM	Active Tracer High resolution Atmospheric Model
AVHRR	Advanced Very High Resolution Radiometer
CAPE	convective available potential energy
CCN	cloud condensation nuclei
CLDN	Canadian Lightning Detection Network
DMSP	Defense Meteorological Satellite Programme
ECMWF	European Centre for Medium-Range Weather Forecast
GOES	Geostationary Operational Environmental Satellite
IN	ice nuclei
LCL	lifting condensation level
LFC	level of free convection
LNB	level of neutral buoyancy
MDT	Mountain Daylight Time (=UTC−6 h)
MISR	Multi-angle Imaging Spectral Radiometer
MODIS	Moderate Resolution Imaging SpectroRadiometer
PV	potential vorticity
pyroCb	pyro-cumulonimbus
RAOB	radiosonde observations
TKE	turbulent kinetic energy
TPM	total particulate matter
TST	troposphere-to-stratosphere exchange
UT/LS	upper troposphere and lower stratosphere
UTC	Coordinated Universal Time
VMD	volume mean diameter

List of Figures

List of Tables

References

Adler, R. F., and R. A. Mack, Thunderstorm cloud top dynamics as inferred from satellite observations and a cloud top parcel model, *J. Atmos. Sci.*, *43*(18), 1945–1960, 1986.

Anderson, G. P., S. A. Clough, F. X. Kneizys, J. H. Chetwynd, and E. P. Shettle, AFGL atmospheric constituent profiles (0–120 km), *Tech. Rep. AFGL-TR-86-0110*, Air Force Geophys. Lab., Hanscom Air Force Base, Mass., 1986.

Andreae, M. O., The influence of tropical biomass burning on climate and the atmospheric environment, in *Biogeochemistry of Global Change: Radiatively Active Trace Gases*, edited by R. S. Oremland, pp. 113–150, Chapman & Hall, New York, NY, 1993.

Andreae, M. O., and P. Merlet, Emission of trace gases and aerosols from biomass burning, *Global Biogeochem. Cycles*, *15*(4), 955–966, 2001.

Andreae, M. O., D. Rosenfeld, P. Artaxo, A. A. Costa, G. P. Frank, K. M. Longo, and M. A. F. Silva-Dias, Smoking rain clouds over the Amazon, *Science*, *303*, 1337–1342, 2004.

Andreae, M. O., C. D. Jones, and P. M. Cox, Strong present-day aerosol cooling implies a hot future, *Nature*, *435*, 1187–1190, doi:10.1038/nature03671, 2005.

Antle, J., et al., Ecosystems and their goods and services, in *Climate Change 2001: Impacts, Vulnerability and Adaptation. Contribution of Working Group II to the Third Assessment Report of the Intergovernmental Panel on Climate Change*, edited by J. J. McCarthy, O. F. Canziani, N. A. Leary, D. J. Dokken, and K. S. White, pp. 239–288, Cambridge University Press, Cambridge, United Kingdom and New York, NY, USA, 2001.

Arakawa, A., and V. R. Lamb, Computational design of the basic dynamical processes of the ucla general circulation model, in *General circulation models of the atmosphere*, pp. 173–265, Academic Press, New York, 1977.

Asner, G. P., D. E. Knapp, E. N. Broadbent, P. J. C. Oliveira, M. Keller, and J. N. Silva, Selective Logging in the Brazilian Amazon, *Science*, *310*, 480–482, doi:10.1126/science.1118051, 2005.

ASRD, Final Documentation Report - Chisholm Fire (LWF-063), Forest Protection Division, ISBN 0-7785-1841-8, *Tech. rep.*, Alberta Sustainable Resource Development, 2001.

Banta, R. M., L. D. Olivier, E. T. Holloway, R. A. Kropfli, B. W. Bartram, R. E. Cupp, and M. J. Post, Smoke.column observations from two forest fires using doppler lidar and doppler radar, *J. Appl. Meteorol.*, *31*, 1328–1349, 1992.

Bigg, E. K., The formation of atmospheric ice crystals by the freezing of droplets, *Q. J. R. Meteorol. Soc.*, *79*, 510–519, 1953.

Bluth, G. J. S., S. D. Doiron, C. C. Schnetzler, A. J. Krueger, and L. S. Walter, Global tracking of the SO2 clouds from the June, 1991 Mount Pinatubo eruptions, *Geophys. Res. Lett.*, *19*, 151–154, 1992.

Brasseur, G., and S. Solomon, *Aeronomy of the Middle Atmosphere*, D.Reidel Publishing Company, Dordrecht, The Netherlands, 1984.

Byers, H. R., *Elements of Cloud Physics*, The University of Chicago Press, 1965.

Byram, G. M., Combustion of forest fuels, in *Forest Fire Control and Use*, edited by K. P. Davis, McGraw-Hill, New York, 1959.

Carpenter, F. A., Convectional clouds induced by forest fires, *Mon. Wea. Rev.*, *47*(3), 143–144, 1919.

Chuang, C. C., J. E. Penner, and L. L. Edwards, Nucleation scavenging of smoke particles and simulated drop size distributions over large biomass fires, *J. Atmos. Sci.*, *49*(14), 1264–1275, 1992.

Clark, T. L., M. A. Jenkins, J. Coen, and D. Packham, A coupled atmosphere-fire model: Convective feedback on fire-line dynamics, *J. Appl. Meteorol.*, *35*(6), 875–901, 1996.

Clark, T. L., J. Coen, and D. Latham, Description of a coupled atmosphere-fire model, *Int. J. Wildland Fire*, *13*, 49–63, 2004.

Clements, C. B., B. E. Potter, and S. Zhong, In situ measurements of water vapor, heat, and CO_2 fluxes within a prescribed grass fire, *Int. J. Wildland Fire*, *15*, 299–306, 2006.

Coen, J., Simulation of the Big Elk Fire using coupled atmosphere-fire modeling, *Int. J. Wildland Fire*, *14*, 49–59, 2005.

Colarco, P. R., M. R. Schoeberl, B. G. Doddridge, L. T. Marufu, O. Torres, and E. J. Welton, Transport of smoke from Canadian forest fires to the surface near Washington, D.C.: Injection height, entrainment, and optical properties, *J. Geophys. Res.*, *109*, D06203, doi:10.1029/2003JD004248, 2004.

Cook, J., and E. Highwood, Climate response to tropospheric absorbing aerosol in an intermediate general-circulation model, *Q. J. R. Meteorol. Soc.*, *130*, 175–191, 2004.

Crutzen, P., Climatic change albedo enhancement by stratospheric sulfur injections: A contribution to resolve a policy dilemma?, *Climatic Change*, *77*, 211–220, doi:10.1007/s10584-006-9101-y, 2006.

Crutzen, P., and J. Birks, The atmosphere after a nuclear war: Twilight at noon, *Ambio*, *11*, 114–125, 1982.

Crutzen, P. J., and M. O. Andreae, Biomass burning in the tropics: Impact on atmospheric chemistry and biogeochemical cycles, *Science*, *250*, 1669–1678, 1990.

Cunningham, P., S. L. Goodrick, M. Y. Hussaini, and R. R. Linn, Coherent vortical structures in numerical simulations of buoyant plumes from wildland fires, *Int. J. Wildland Fire*, *14*, 61–75, 2005.

Damoah, R., et al., A case study of pyro-convection using transport model and remote sensing data, *Atmos. Chem. Phys.*, *6*, 173–185, 2006.

Deardorff, J. W., Stratocumulus-capped mixed layers derived from a 3-dimensional model, *Boundary Layer Meteorology*, *18(4)*, 495–527, 1980.

Emanuel, K. A., *Atmospheric Convection*, Oxford Univesity Press, New York, 1994.

FIRESCAN Science Team, Fire in ecosystems of boreal eurasia: The bor forest island fire experiment, fire research campaign asia-north (FIRESCAN), in *Biomass Burning and Global Change*, edited by J. S. Levine, pp. 848–873, MIT Press, Cambridge, Mass., 1996.

Fischer, H., et al., Deep convective injection of boundary layer air into the lowermost stratosphere at midlatitudes, *Atmos. Chem. Phys.*, *3*, 739–745, 2003.

Fromm, M., J. Alfred, K. Hoppel, J. Hornstein, R. Bevilacqua, E. Shettle, R. Servranckx, Z. Li, and B. Stocks, Observations of boreal forest fire smoke in the stratosphere by POAM III, SAGE II, and lidar in 1998, *Geophys. Res. Lett.*, *27*(9), 1407–1410, 2000.

Fromm, M., R. Bevilacqua, B. Stocks, and R. Servranckx, New directions: Eruptive transport to the stratosphere: Add fire-convection to volcanoes, *Atmos. Environ.*, *38*, 163–165, 2004.

Fromm, M., R. Bevilacqua, R. Servranckx, J. Rosen, J. Thayler, J. Herman, and D. Larko, Pyro-cumulonimbus injection of smoke into the stratosphere: Observations and impact of a super blowup in northwestern Canada on 3-4 August 1998, *J. Geophys. Res.*, *110*(16), D08205, doi:10.1029/2004JD005350, 2005.

Fromm, M., A. Tupper, D. Rosenfeld, R. Servranckx, and R. McRae, Violent pyroconvective storm devastates Australia's capital and pollutes the stratosphere, *Geophys. Res. Lett.*, *33*, L05815, doi:10.1029/2005GL025161, 2006.

Fromm, M., O. Torres, D. Diner, D. Lindsey, B. V. Hull, R. Servranckx, E. Shettle, and Z. Li, The stratospheric impact of the Chisholm Pyro-Cumulonimbus eruption: nadir satellite perspective, *in preparation for J. Geophys. Res.*, 2007a.

Fromm, M., et al., The stratospheric impact of the Chisholm Pyro-Cumulonimbus eruption: vertical profile perspective, *in preparation for J. Geophys. Res.*, 2007b.

Fromm, M. D., and R. Servranckx, Transport of forest fire smoke above the tropopause by supercell convection, *Geophys. Res. Lett.*, *30*(10), 1542, doi: 10.1029/2002GL016820, 2003.

Fu, Q., and K. N. Liou, Parameterization of the radiative properties of cirrus clouds, *J. Atmos. Sci.*, *50*(13), 2008–2025, 1993.

Gassó, S., and D. A. Hegg, Comparison of columnar aerosol optical properties measured by the MODIS Airborne Simulator with *in situ* measurements: A case study, *Remote Sens. Environ.*, *66*, 138–152, 1998.

Glickmann, T. S. (Ed.), *Glossary of Meteorology*, 2nd ed., American Meteorological Society, http://amsglossary.allenpress.com/glossary, 2000.

Goldammer, J. G., and C. Price, Potential impacts of climate change on fire regimes in the tropics based on MAGICC and a GISS GCM-derived lightning model, *Climatic Change*, *39*, 273–296, 1998.

Gostintesev, Y. A., N. P. Kopylov, A. M. Ryzhov, and I. R. Khazanov, Numerical modeling of convective flows above large fires at various atmospheric conditions, *Combust., Expl., Shock Waves*, *27*(6), 656–662, 1991.

Graf, H.-F., The complex interactions of aerosols and clouds, *Science*, *303*, 1309–1311, 2004.

Graf, H.-F., M. Herzog, J. M. Oberhuber, and C. Textor, The effect of environmental conditions on volcanic plume rise, *J. Geophys. Res.*, *104*(D20), 24,309–24,320, 1999.

Hanisco, T. F., et al., Observations of deep convective influence on stratospheric water vapor and its isotopic composition, *Geophys. Res. Lett.*, *34*, L04814, doi: 10.1029/2006GL027899, 2007.

Herzog, M., Simulation der dynamik eines multikomponentensystems am beispiel vulkanischer eruptionswolken., Ph.D. thesis, University of Hamburg, 1998.

Herzog, M., H.-F. Graf, C. Textor, and J. M. Oberhuber, The effect of phase changes of water on the development of volcanic plumes, *J. Volcanol. Geotherm. Res*, *87*, 55–74, 1998.

Herzog, M., J. M. Oberhuber, and H.-F. Graf, A prognostic turbulence scheme for the nonhydrostatic plume model ATHAM, *J. Atmos. Sci.*, *60*, 2783–2796, 2003.

Heymsfield, G. M., and R. H. Blackmer, Jr, Satellite-observed characteristics of midwest severe thunderstorm anvils, *Mon. Wea. Rev.*, *116*, 2200–2224, 1988.

Heymsfield, G. M., G. Sezejwach, S. Schotz, and R. H. Blackmer, Jr, Upper level structure of Oklahoma tornadic stroms on 2 may 1979. II: Proposed explanation of "V" pattern and internal warm region in infrared observation, *J. Atmos. Sci.*, *40*, 1756–1767, 1983.

Hobbs, P. V., and J. D. Locatelli, Ice nuclei from a natural forest fire, *J. Appl. Meteorol.*, *8*, 833–834, 1969.

Hobbs, P. V., J. S. Reid, J. A. Herring, J. D. Nance, R. E. Weiss, J. L. Ross, D. A. Hegg, R. D. Ottmar, and C. Liousse, Particle and trace-gas measurements in the smoke from prescribed burns of forest products in the Pacific Northwest, in *Biomass Burning and Global Change*, edited by J. S. Levine, pp. 697–715, MIT Press, Cambridge, Mass., 1996.

Hobbs, P. V., P. Sinha, R. J. Yokelson, T. J. Christian, D. R. Blake, S. Gao, T. W. Kirchstetter, T. Novakov, and P. Pilewskie, Evolution of gases and particles from a savanna fire in South Africa, *J. Geophys. Res.*, *108*(D13), 8485, doi: 10.1029/2002JD002352, 2003.

Hodzic, A., R. Vautard, H. Chepfer, P. Goloub, L. Menut, P. Chazette, J. L. Deuzé, A. Apituley, and P. Couvert, Evolution of aerosol optical thickness over Europe during the August 2003 heat wave as seen from CHIMERE model simulations and POLDER data, *Atmos. Chem. Phys.*, *6*, 1853–1864, 2006.

Hodzic, A., S. Madronich, B. Bohn, S. Massie, L. Menut, and C. Wiedinmyer, Wildfire particulate matter in Europe during summer 2003: meso-scale modeling of smoke emissions, transport and radiative effects, *Atmos. Chem. Phys. Discuss.*, *7*, 4705–4760, 2007.

Holton, J. R., P. H. Haynes, M. E. McIntyre, A. R. Douglass, R. B. Rood, and L. Pfister, Stratosphere-troposphere exchange, *Reviews of Geophysics*, *33*(4), 403–439, 1995.

Houghton, J. T., Y. Ding, D. J. Griggs, M. Noguer, P. J. van der Linden, X. Dai, K. Maskell, and C. A. Johnson (Eds.), *Climate Change 2001: The Scientific Basis. Contribution of Working Group I to the Third Assessment Report of the Intergovernmental Panel on Climate Change*, Cambridge University Press, Cambridge, United Kingdom and New York, NY, USA, 2001.

Houze, R. A., *Cloud Dynamics*, Academic Press, San Diego, 1993.

Hungershöfer, K., Optical properties of aerosol particles and radiative transfer in connection with biomass burning, Ph.D. thesis, Institute for Meteorology, University of Leipzig, 2007.

Immler, F., D. Engelbart, and O. Schrems, Fluorescence from atmospheric aerosol detected by a lidar indicates biogenic particles in the lowermost stratosphere, *Atmos. Chem. Phys.*, *5*, 345–355, 2005.

Inoue, T., A cloud type classification with NOAA 7 split-window measurements, *J. Geophys. Res.*, *92*, 3991–4000, 1987.

Jaffe, D., I. Bertschi, L. Jaegle, P. Novelli, J. S. Reid, H. Tanimoto, R. Vingarzan, and D. L. Westphal, Long-range transport of siberian biomass burning emissions and impact on surface ozone in western north america, *Geophys. Res. Lett.*, *31*, L16106, doi:10.1029/2004GL020093, 2004.

Jenkins, M. A., Investigating the Haines Index using parcel model theory, *Int. J. Wildland Fire*, *13*, 297–309, 2004.

Jost, H.-J., et al., In-situ observation of mid-latitude forest fire plumes deep in the stratosphere, *Geophys. Res. Lett.*, *31*, L11101, doi:10.1029/2003GL019253, 2004.

Jungwirth, P., D. Rosenfeld, and V. Buch, A possible new molecular mechanism of thundercloud electrification, *Atmospheric Research*, *76*, 190–205, 2005.

Kasischke, E. S., J. N. L. Christensen, and B. J. Stocks, Fire, global warming, and the carbon balance of boreal forests, *Ecological Applications*, *5*, 437–451, doi:10.2307/1942034, 1995.

Khain, A., M. Ovtchinnikov, M. Pinsky, A. Pokrovsky, and H. Krugliak, Notes on the state-of-the-art numerical modeling of cloud microphysics, *Atmos. Res.*, *55*, 159–224, 2000.

Khain, A., A. Pokrovsky, M. Pinsky, A. Seifert, and V. Phillips, Simulation of effects of atmospheric aerosols on deep turbulent convective clouds using a spectral microphysics mixed-phase cumulus cloud model. Part I: Model description and possible applications, *J. Atmos. Sci.*, *61*, 2963–2982, 2004.

Koren, I., Y. J. Kaufman, D. Rosenfeld, L. A. Remer, and Y. Rudich, Aerosol invigoration and restructuring of Atlantic convective clouds, *Geophys. Res. Lett.*, *32*, doi:10.1029/22005GL023187, 2005.

Kurz, W., and M. Apps, A 70 year retrospective analysis of carbon fluxes in the canadian forest sector, *Ecological Applications*, *9*, 526–547, 1999.

Lane, T. P., and R. D. Sharman, Gravity wave breaking, secondary wave generation, and mixing above deep convection in a three-dimensional cloud model, *Geophys. Res. Lett.*, *33*, L23813, doi:10.1029/2006GL027988, 2006.

Lane, T. P., R. D. Sharman, T. L. Clark, and H.-M. Hsu, An Investigation of Turbulence Generation Mechanisms above Deep Convection., *J. Atmos. Sci.*, *60*, 1297–1321, 2003.

Lavoué, D., C. Liousse, H. Cachier, B. J. Stocks, and J. G. Goldammer, Modeling of carbonaceous particles emitted by boreal and temperate wildfires at northern latitudes, *J. Geophys. Res.*, *105*(D22), 26,871–26,890, 2000.

Levizzani, V., and M. Setvák, Multispectral, high-resolution satellite observations of plumes on top of convective storms, *J. Atmos. Sci.*, *53*(3), 361–369, 1996.

Linn, R., J. Winterkamp, J. J. Colman, C. Edminster, and J. D. Bailey, Modeling interactions between fire and atmosphere in discrete element fuel beds, *Int. J. Wildland Fire*, *14*, 37–48, 2005.

Livesey, N. J., M. D. Fromm, J. W. Waters, G. L. Manney, M. L. Santee, and W. G. Read, Enhancements in lower stratopsheric CH_3CN observed by the Upper Atmosphere Research Satellite Microwave Limb Sounder following boreal forest fires, *J. Geophys. Res.*, *109*, D06308, doi:10.1029/2003JD004055, 2004.

Lohmann, U., and J. Feichter, Global indirect aerosol effects: A review, *Atmos. Chem. Phys.*, *5*, 715–737, 2005.

Luderer, G., J. Trentmann, T. Winterrath, C. Textor, M. Herzog, H.-F. Graf, and M. O. Andreae, Modeling of biomass smoke injection into the lower stratosphere by a large forest fire (Part II): Sensitivity studies, *Atmos. Chem. Phys.*, *6*, 5261–5277, 2006.

Luderer, G., J. Trentmann, and M. O. Andreae, The role of fire-released moisture on the dynamics of atmospheric pyro-convection, *submitted to Int. J. Wildland Fire*, 2007a.

Luderer, G., J. Trentmann, K. Hungershoefer, M. Herzog, M. Fromm, and M. O. Andreae, Small-scale mixing processes enhancing troposphere-to-stratosphere transport by pyro-cumulonimbus storms, *Atmos. Chem. Phys. Discuss.*, *7*, 10,371–10,403, 2007b.

Manis, P. C., Cloud heights and stratospheric injections resulting from a thermonuclear war, *Atmos. Environ.*, *19*(8), 1245–1255, 1985.

Mason, S. A., R. F. Field, R. J. Yokelson, M. A. Kochivar, M. R. Tinsley, D. E. Ward, and W. M. Hao, Complex effects arising in smoke plume simulations due to inclusion of direct emissions of oxygenated organic species from biomass combustion, *J. Geophys. Res.*, *106*(D12), 12,527–12,539, 2001.

McCarter, R. J., and A. Broido, Radiative and convective energy from wood crib fires, *Pyrodynamics*, *2*, 65–85, 1965.

Mitchell, R. M., D. M. O'Brien, and S. K. Campbell, Characteristics and radiative impact of the aerosol generated by the Canberra firestorm of January 2003, *J. Geophys. Res.*, *111*, D02204, doi:10.1029/2005JD006304, 2006.

Morton, B. R., S. G. Taylor, and J. S. Turner, Turbulent gravitational convection from maintained and instantaneous sources, *Proc. R. Soc. Ser. A*, *234*(1196), 1–23, 1956.

Mullendore, G. L., D. R. Durran, and J. R. Holton, Cross-tropopause tracer transport in midlatitude convection, *J. Geophys. Res.*, *110*, D06113, doi: 10.1029/2004JD005059, 2005.

Murakami, M., Numerical modeling of the dynamical and microphysical evolution of an isolated convective cloud − The 19 july 1981 CCOPE cloud, *J. Met. Soc. Japan*, *68*(2), 107–128, 1990.

Nedelec, P., V. Thouret, J. Brioude, B. Sauvage, J.-P. Cammas, and A. Stohl, Extreme CO concentrations in the upper troposphere over northeast Asia in June 2003 from the in situ MOZAIC aircraft data, *Geophys. Res. Lett.*, *32*, L14807, doi:10.1029/2005GL023141, 2005.

Nepstad, D. C., et al., Large-scale impoverishment of Amazonian forests by logging and fire, *Nature*, *398*, 505–508, 1999.

Oberhuber, J. M., M. Herzog, H.-F. Graf, and K. Schwanke, Volcanic plume simulation on large scales, *J. Volcanol. Geotherm. Res*, *87*, 29–53, 1998.

Packham, D. R., Heat transfer above a small ground fire, *Aust. For. Res.*, *5*, 19–24, 1969.

Penner, J. E., L. C. Haselman, Jr., and L. L. Edwards, Smoke-plume distribution above large-scale fires: Implications for simulations of "Nuclear Winter", *J. Climate and Appl. Meteorol.*, *25*, 1434–1444, 1986.

Penner, J. E., M. M. Bradley, C. C. Chuang, L. L. Edwards, and L. F. Radke, A numerical simulation of the aerosol-cloud interaction and atmospheric dynamics of the hardiman township, ontario, prescribed burn, in *Global Biomass Burning: Atmospheric, Climatic, and Biospheric Implications*, edited by J. S. Levine, pp. 420–426, MIT Press, Cambridge, Mass., 1991.

Penner, J. E., R. E. Dickerson, and C. A. O'Neill, Effects of aerosol from biomass burning on the global radiation budget, *Science*, *256*, 1432–1434, 1992.

Pickering, K. E., et al., Convective transport of biomass burning emissions over Brazil during TRACE A, *J. Geophys. Res.*, *101*, 23,993–24,012, doi:10.1029/96JD00346, 1996.

Pittman, J. V., et al., Transport in the subtropical lowermost stratosphere during the Cirrus Regional Study of Tropical Anvils and Cirrus Layers-Florida Area Cirrus Experiment, *J. Geophys. Res.*, *112*(D11), D08304, doi:10.1029/2006JD007851, 2007.

Potter, B. E., The role of released moisture in the atmospheric dynamics associated with wildland fires, *Int. J. Wildland Fire*, *14*, 77–84, 2005.

Pruppacher, H. R., and J. D. Klett, *Microphysics of Clouds and Precipitation*, Kluwer Academic Publishers, 1997.

Radke, L., D. Hegg, J. Lyons, C. Brock, P. Hobbs, R. Weiss, and R. Rasmussen, Airborne measurements on smoke from biomass burning, in *Aerosols and Climate*, edited by P. V. Hobbs and P. McCormick, pp. 411–422, A. DEEPAK Publishing, 1988.

Radke, L. F., D. A. Hegg, P. V. Hobbs, J. D. Nance, J. H. Lyons, K. K. Laursen, R. E. Weiss, P. J. Riggan, and D. E. Ward, Particulate and trace gas emissions from large biomass fires in north america, in *Global Biomass Burning: Atmospheric, Climatic, and Biospheric Implications*, edited by J. S. Levine, pp. 209–224, MIT Press, Cambridge, Mass., 1991.

Ray, E. A., et al., Evidence of the effect of summertime midlatitude convection on the subtropical lower stratosphere from CRYSTAL-FACE tracer measurements, *J. Geophys. Res.*, *109*(D18), D18304, doi:10.1029/2004JD004655, 2004.

Reid, J. S., and P. V. Hobbs, Physical and optical properties of young smoke from individual biomass fires in Brazil, *J. Geophys. Res.*, *103*(D24), 32,013–32,030, 1998.

Reid, J. S., P. V. Hobbs, R. J. Ferek, D. R. Blake, J. V. Martins, M. R. Dunlap, and C. Liousse, Physical, chemical, and optical properties of regional hazes dominated by smoke in Brazil, *J. Geophys. Res.*, *103*(D24), 32,059–32,080, 1998.

Reid, J. S., R. Koppmann, T. F. Eck, and D. P. Eleuterio, A review of biomass burning emissions part II: intensive physical properties of biomass burning particles, *Atmos. Chem. Phys.*, *5*, 799–825, 2005.

Reisin, T., Z. Levin, and S. Tzivion, Rain production in convective clouds as simulated in an axisymmetric model with detailed microphysics. Part1: Description of the model, *J. Atmos. Sci.*, *53*(3), 497–519, 1996.

Robock, A., Volcanic eruptions and climate, *Rev. Geophys.*, *38*, 191–219, 2000.

Robock, A., L. Oman, G. L. Stenchikov, O. B. Toon, C. Bardeen, and R. P. Turco, Climatic consequences of regional nuclear conflicts, *Atmos. Chem. Phys.*, *7*, 2003–2012, 2007.

Rogers, R. R., and M. K. Yau, *A Short Course in Cloud Physics*, Butterworth-Heinemann, 1989.

Rosenfeld, D., Suppression of rain and snow by urban and industrial air pollution, *Science*, *287*, 1793–1796, 2000.

Rosenfeld, D., and W. L. Woodley, Deep convective clouds with sustained supercooled liquid water down to −37.5°C, *Nature*, *405*, 440–442, 2000.

Rosenfeld, D., M. Fromm, J. Trentmann, G. Luderer, M. O. Andreae, and R. Servranckx, The Chisholm firestorm: observed microstructure, precipitation and lightning activity of a pyro-cumulonimbus, *Atmos. Chem. Phys.*, *6*, 645–659, 2007.

Schlesinger, R. E., Mature Thunderstorm Cloud-Top Structure and Dynamics: A Three-Dimensional Numerical Simulation Study., *J. Atmos. Sci.*, *41*, 1551–1570, 1984.

Seifert, A., and K. D. Beheng, A two-moment cloud microphysics parameterization for mixed-phase clouds. Part1: Model description, *Meteorol. Atmos. Phys.*, *92*, 45–66, doi:10.1007/s00703-005-0112-4, 2006.

Setvák, M., R. M. Rabin, and P. K. Wang, Contribution of the MODIS instrument to observations of deep convective storms and stratospheric moisture detection in GOES and MSG imagery, *Atmospheric Research*, *83*, 505–518, 2007.

Siebert, J., C. Timmis, G. Vaughan, and K. H. Fricke, A strange cloud in the Artic summer stratosphere 1998 above Esrange (68°N), Sweden, *Annales Geophysicae*, *18*, 505–509, 2000.

Simard, A. J., D. A. Haines, R. W. Blank, and J. S. Frost, The Mack Lake Fire, *Tech. Rep. NC-83*, USDA Forest Service, General Technical Report NC-83., 1983.

Simmel, M., and S. Wurzler, Condensation and activation in sectional cloud microphysical models, *Atmos. Res.*, *80*, 218–236, 2006.

Small, R. D., and K. E. Heikes, Early cloud formation by large area fires, *J. Appl. Meteorol.*, *27*, 654–663, 1988.

Stocks, B. J., M. E. Alexander, and R. A. Lanoville, Overview of the International Crown Fire Modelling Experiment (ICFME), *Can. J. For. Res.*, *34*, 1543–1547, 2004.

Stocks, B. J., et al., Climate change and forest fire potential in russian and canadian boreal forests, *Climatic Change*, *38*(1), 1–13, 1998.

Stohl, A., et al., Stratosphere-troposphere exchange: A review, and what we have learned from STACCATO, *J. Geophys. Res.*, *108*(D12), 8516, doi:10.1029/2002JD002490, 2003.

Stull, R. B., *An introduction to boundary layer meteorology*, Kluwer Academic Publishers, Dordrecht, 1988.

Textor, C., H.-F. Graf, M. Herzog, and J. M. Oberhuber, Injection of gases into the stratosphere by explosive volcanic eruptions, *J. Geophys. Res.*, *108*(D19), 4606, doi:10.1029/2002JD002987, 2003.

Textor, C., H. F. Graf, M. Herzog, J. M. Oberhuber, W. I. Rose, and G. G. J. Ernst, Volcanic particle aggregation in explosive eruption columns. Part I: Parameterization of the microphysics of hydrometeors and ash, *J. Volcanol. Geotherm. Res*, *150*, 359–377, 2006a.

Textor, C., H. F. Graf, M. Herzog, J. M. Oberhuber, W. I. Rose, and G. G. J. Ernst, Volcanic particle aggregation in explosive eruption columns. Part II: Numerical experiments, *J. Volcanol. Geotherm. Res*, *150*, 378–394, 2006b.

Thomas, G. E., and K. Stamnes, *Radiative transfer in the atmosphere and ocean*, Cambridge University Press, Cambridge, 1999.

Trentmann, J., Atmospheric processes in a young biomass burning plume − radiation and chemistry, Ph.D. thesis, University of Hamburg, 2001.

Trentmann, J., M. O. Andreae, H.-F. Graf, P. V. Hobbs, R. D. Ottmar, and T. Trautmann, Simulation of a biomass-burning plume: Comparison of model results with observations, *J. Geophys. Res.*, *107*(D2), 4013, doi:10.1029/2001JD000410, 2002.

Trentmann, J., M. O. Andreae, and H.-F. Graf, Chemical processes in a young biomass-burning plume, *J. Geophys. Res.*, *108*(D22), 4705, doi:10.1029/2003JD003732, 2003a.

Trentmann, J., B. Früh, O. Boucher, T. Trautmann, and M. O. Andreae, Three-dimensional solar radiation effects on the actinic flux field in a biomass-burning plume, *J. Geophys. Res.*, *108*(D17), 4558, doi:10.1029/2003JD003422, 2003b.

Trentmann, J., R. J. Yokelson, P. V. Hobbs, T. Winterrath, T. J. Christian, M. O. Andreae, and S. A. Mason, An analysis of the chemical processes in the smoke plume from a savanna fire, *J. Geophys. Res.*, *110*, D12301, doi: 10.1029/2004JD005628, 2005.

Trentmann, J., G. Luderer, T. Winterrath, M. Fromm, R. Servranckx, C. Textor, M. Herzog, H.-F. Graf, and M. O. Andreae, Modeling of biomass smoke injection into the lower stratosphere by a large forest fire (Part I): Reference study, *Atmos. Chem. Phys.*, *6*, 5247–5260, 2006.

Turco, R. P., O. B. Toon, T. P. Ackerman, J. B. Pollack, and C. Sagan, Nuclear winter: Global consequences of multiple nuclear explosions, *Science*, *222*, 1283–1292, 1983.

Van Wagner, C. E., The development and structure of the canadian forest fire weather index system. forestry technical report ftr-35, *Tech. rep.*, Candian Forest Service, Petawawa National Forestry Institute, Chalk River, Ontario, 1987.

Waibel, A. E., H. Fischer, F. G. Wienhold, P. C. Siegmund, B. Lee, J. Stroem, J. Lelieveld, and P. J. Crutzen, Highly elevated carbon monoxide concentrations in the upper troposphere and lowermost stratosphere at northern midlatitudes during the STREAM II summer campaign in 1994, *Chemosphere - Global Change Science*, *1*, 233–248, 1999.

Wang, C., A modeling study of the response of tropical deep convection to the increase of cloud condensation nuclei concentration: 1. dynamics and microphysics, *J. Geophys. Res.*, *110*(D21211), doi:10.1029/2004JD005720, 2005.

Wang, P. K., Moisture plumes above thunderstorm anvils and their contributions cross-tropopause transport of water vapor in midlatitudes, *J. Geophys. Res.*, *108*(D6), 4194, doi:10.1029/2002JD002581, 2003.

Wang, P. K., The thermodynamic structure atop a penetrating convective thunderstorm, *Atmos. Res.*, *83*, 254–262, 2007.

Ward, D., Combustion chemistry and smoke, in *Forest Fires: Behavior and Ecological Effects*, edited by E. A. Johnson and K. Miyanishi, pp. 55–77, Academic Press, San Diego, 2001.

Ward, R. D., Clouds over a fire, *Science*, *5*, 60–61, 1897.

Ward, R. D., Cumulus clouds over a fire, *Mon. Wea. Rev.*, *26*, 104–105, 1898.

Westerling, A. L., H. G. Hidalgo, D. R. Cayan, and T. W. Swetnam, Warming and Earlier Spring Increase Western U.S. Forest Wildfire Activity, *Science*, *313*, 940–943, doi:10.1126/science.1128834, 2006.

Wooster, M. J., Small-scale experimental testing of fire radiative energy for quantifying mass combusted in natural vegetation fires, *Geophys. Res. Lett.*, *29*(21), doi:10.1029/2002GL015487, 2002.

Wooster, M. J., G. Roberts, G. L. W. Perry, and Y. J. Kaufman, Retrieval of biomass combustion rates and totals from fire radiative power observations: FRP derivation and calibration relationships between biomass consumption and fire radiative energy release, *J. Geophys. Res.*, *110*, D24311, doi: 10.1029/2005JD006318, 2005.

Zimet, T., J. E. Martin, and B. E. Potter, The influence of an upper-level frontal zone on the Mack Lake wildfire environent, *Meteorol. Appl.*, *14*, 131–147, 2007.